NANOMETER SCALE FRICTION AND WEAR ON SELF-ASSEMBLED MONOLAYERS INVESTIGATED BY ATOMIC FORCE MICROSCOPY

INAUGURALDISSERTATION

zur
Erlangung der Würde eines Doktors der Philosophie
vorgelegt der
Philosophisch-Naturwissenschaftlichen Fakultät
der Universität Basel

von

Susanne Kopta
aus Rheinfelden / Deutschland

Basel, 2001

Genehmigt von der Philosophisch-Naturwissenschaftlichen Fakultät auf Antrag der Herren

Professor Dr. E. Meyer

Dr. M. Salmeron

Basel, den 03. Juli 2001

Prof. Dr. A. Zuberbühler, Dekan

Abstract

Nanometer scale tribology investigates the phenomena of adhesion, friction and wear at the molecular level. It is driven by a basic research interest to unveil the fundamental nature of the processes responsible for energy dissipation in friction and the modification of the interface by wear. Furthermore, for modern technologies, such as hard disk drives and micro-electro-mechanical systems (MEMS), it is crucial to understand the role of monolayer thick lubricants, i.e. to correlate the mechanical properties with the molecular structure of these layers. Atomic force microscopy (AFM) is used to investigate wear on muscovite mica and friction on self-assembled monolayers on the nanometer scale. Two basic mechanisms for energy dissipation are revealed. First, on muscovite mica, the production of surface defects, i.e. the rupture of Si-O bonds at the surface, although not yet visible in contact AFM images, has a noticeable contribution to friction. This contribution can be explained with a model based on the stress-induced enhancement of the rate of thermal defect production. Besides, the accumulation of these defects leads to the creation of 2 Å deep holes, which have not been observed with AFM before. Second, on monolayer islands of alkylsilane molecules, self-assembled in an *all-trans*, upright configuration on mica, a correlation between discrete structural changes and stepwise changes of the frictional properties, occurring at specific threshold loads, is determined. A model of discrete molecular tilts explains the stepwise decrease in height accompanied by an increase in friction observed for increasing applied load and allows to quantify the increase in frictional force: Meta-stable states are dictated by the zigzag skeletal structure of the carbon atoms and the requirement of optimal packing density. Pressure-induced transitions between meta-stable states of interlocked molecules are also observed for alkyl thiol monolayer islands on gold. Measurements on specific thiol monolayers, containing a photo-polymerizable diacetylene group within the alkyl chain, show that frictional properties can be manipulated by internal molecular scaffolding. Upon polymerization a linear polymer backbone forms, which covalently links neighboring molecules, preventing the relative motion of the molecules necessary for tilting. Thus the typical stepwise increase in friction with increasing load observed for unpolymerized monolayers vanishes upon polymerization.

Reibung und Verschleiss auf sich selbst-anordnenden Monolagen untersucht auf der Nanometer-Skala mit Raster-Kraft-Mikroskopie

Tribologie auf der Nanometer-Skala untersucht die Phänomene Adhesion, Reibung und Verschleiss in molekularen Grössenordnungen. Die Forschung auf diesem Gebiet wird von dem Interesse vorangetrieben, die Grundlagen der Prozesse zu entschleiern, die für die Dissipation von Energie bei Reibung und die Modifikation von Grenzflächen bei Verschleiss verantwortlich sind. Darüber hinaus ist es für moderne Technologien wie z. B. für Computerfestplatten und mikro-elektromechanische Systeme (MEMS) entscheidend, die Funktion von Schmiermitteln zu verstehen, die nur eine Monolage dick sind, d. h. einen Zusammenhang herzustellen zwischen den mechanischen Eigenschaften und der molekularen Struktur solcher Lagen. Mit Hilfe der Raster-Kraft-Mikroskopie (engl. "atomic force microscopy", kurz AFM) werden Verschleiss auf Glimmer und Reibung auf sich selbst-anordnenden Monolagen in der Grössenordnung von Nanometern untersucht. Dabei werden zwei grundlegende Mechanismen für Energiedissipation aufgedeckt: (1) Auf Glimmer, leistet die Produktion von Fehlstellen an der Oberfläche, die durch den Bruch von Si-O Bindungen an der Oberfläche entstehen, einen merklichen Beitrag zur Reibung, obwohl die Fehlstellen in Kontakt-AFM Aufnahmen noch nicht sichtbar sind. Dieser Beitrag kann durch ein Modell erklärt werden, das darauf basiert, dass die Rate der thermisch angeregten Produktion von Fehlstellen durch die Belastung, ausgeübt von der AFM Spitze, erhöht wird. Darüberhinaus führt die Anhäufung solcher Fehlstellen zur Entstehung von 2 Å tiefen Löchern, welche zuvor noch nicht mit einem AFM detektiert worden waren. (2) Auf Monolagen hohen Inseln von Alkylsilan-Molekülen, die sich auf Glimmer in einer aufrechten, *all-trans* Konfiguration anordnen, wird ein Zusammenhang zwischen diskreten Änderungen der Struktur und sprunghaften Änderungen der Reibungseigenschaften, die bei bestimmten Grenzwerten des ausgeübten Druckes auftreten, hergestellt. Ein Modell, bei dem die Moleküle in diskreten Schritten kippen, beschreibt die sprunghafte Abnahme der Höhe der Inseln, die von einer Zunahme der Reibung begleitet wird, und die mit zunehmendem Druck auftreten. Darüberhinaus erlaubt das Modell quantitative Aussagen über die Zunahme der Reibungskraft. Metastabile Zustände werden durch das Zickzack-Skelett der Kohlenstoffatome innerhalb der Moleküle und durch die Bedingung der optimalen Packungsdichte festgelegt. Solche druckinduzierten Übergänge zwischen metastabilen Zuständen ineinander verzahnter Moleküle sind auch für Monolageninseln aus Alkylthiolen auf Gold beobachtet worden. Messungen auf speziellen Thiol-Monolagen, die eine durch Licht polymerisierbare Diazetylen-Gruppe enthalten, zeigen, dass die Reibungseigenschaften durch ein internes Molekülgerüst manipuliert werden können. Als Folge der Polymerisation entsteht ein linearer Polymerstützstrang, der benachbarte Moleküle kovalent aneinander bindet, was die relative Versetzung der Moleküle verhindert, die für das Verkippen nötig wäre. Folglich verschwindet die sprunghafte Zunahme der Reibungskraft, die als Funktion des zunehmenden Druckes für unpolymerisierte Monolagen beobachtet werden kann, sobald der Film polymerisiert ist.

Contents

List of Figures

List of Tables

Chapter 1

Introduction

1.1 Motivation

The desire to manipulate matter at the atomic level goes back to the alchemists' dream to turn lead into gold. Nowadays, this dream has slightly changed shape towards machines with micrometer dimensions, to manipulate matter at a nanometer scale. It is reflected in various science fiction movies, one of the most famous "Fantastic Voyage (1966)" where a submarine with a surgical team aboard is miniaturized so it can travel along blood vessels to save the life of a nearly assassinated diplomat. Less virtuous, but closer to reality than shrinking submarines, are the virus-like "Borg nano-probes" (not to be confused with the commercially available "nanoprobe" AFM tips) from the latest Star Trek episodes: Nanometer sized machines with a spider-like appearance that can be programmed to perform different tasks when injected into organic matter. Unfortunately the half-robot half-human species of the Borg uses it to acquire new members and subject them to the will of the hive mind. The reader may be tempted to chuckle or even laugh out loud at this point, but how close we are already to this in the not so distant future shows in one of the latest projects from the IBM research laboratory at Rüschlikon [1]: The cantilever arms of a silicon chip are functionalized to achieve selective binding of proteins or DNA to the levers, the arising surface stress bending the lever. The demonstrated ability to detect variations in the stress arising from a single base mismatch between two DNA sequences, combined with the bending forces acting on the levers, which would be strong enough to operate micromechanical valves, could be used for *in-situ* drug delivery devices: The functionalized arms would identify an infected cell and trigger at the same time the release of medication. Although a yellow press paper already claimed to know the price of one such "nanorob", there is still some time until such devices will become available.

There are more key projects from which it becomes apparent that today we are standing on the threshold into an age where micro-machines will become reality. All of the technologies that will lead there are more or less directly related to the semiconductor industry, which already has provided us with a computer in basically every household of the industrialized nations. One of the most important is the technique to etch three-dimensional structures from silicon: It is essential to the mass production of tip-lever assemblies needed for atomic force microscopes (see section 2.1.1), culminating in the so called "millipede", i.e. an array of 1024 individually addressable, heatable tips, which can burn holes (bits) into a polymer film, to be used as storage device [2]. Furthermore, it has also led to the first microelectromechanical systems (MEMS) [3], which at the current state are micrometer sized gears, etched out of silicon, aimed towards a "true" silicon micromachine. The biggest enemies of micrometer sized structures are friction and adhesion, which are dramatically reducing the lifetime of such devices due to stiction and wear. New types of lubricants are in high demand, since oil and even water will act like glue for such delicate structures, the latter imposing limits on the operation in ambient conditions. But also

the magnetic storage media branch of the computer industry has a need for new lubricants to keep up with the continuous miniaturization of computer hard discs and increasing bit density. Some aspects of such new lubricants will be discussed in section 1.3.

Besides direct applications, there is also a basic research interest, to understand the fundamental nature of the processes responsible for energy dissipation in friction and the modification of the rubbing interfaces by wear at the nanometer scale. Several basic processes have been proposed as elementary energy loss mechanisms [4, 5], including electron-hole pair excitation and electronic drag [6, 7, 8], phonon production [6, 9, 10, 11, 12], viscoelastic deformations of organic films [13, 14, 15, 16] (see Section 1.3 and chapter 4) and point defect production [17, 18, 19, 20]. To design an experiment and sometimes even a new experimental setup, in which just one of these mechanisms can be separately identified and investigated, is not a trivial task. New instrumental developments were necessary to gain insights about friction, adhesion and wear at the nanometer scale, e.g. the surfaces forces apparatus (SFA) [21], the quartz crystal microbalance (QCM) [22], the interfacial force microscope (IFM) [23] and the atomic force microscope (AFM), which is probably the most versatile of these new surface science tools (see Section 1.2 and chapter 2).

This work can only scratch the surface of the vast field of nanotribology, but two important new insights will be presented, both obtained by AFM: In chapter 3 the role of the production of surface defects and its contribution to energy dissipation is investigated. A connection between specific molecular scale events, i.e. discrete tilts, induced in organic monolayers by applying pressure with an AFM tip, and energy dissipation in friction is demonstrated in chapter 4.

1.2 Atomic Force Microscopy

For centuries the knowledge about the friction forces between two sliding bodies was described by two simple statements, together known as Amonton's law of friction: Frictional forces are independent of the area of contact and only proportional to the normal force acting between the sliding bodies. The constant of proportionality, i.e. the friction coefficient, is typical for the specific combination of sliding materials.

Although it was postulated that the independence of contact area must be due to the "true" contact area - formed by microscopic single asperity contacts - being much smaller than the macroscopic one, there was no theory from which information about friction forces of single asperity contacts could be obtained. Furthermore there is no theory to predict the friction coefficient of two materials. Thus tribology was the field for engineers, because only meticulous testing of various material combination could yield new information.

This changed dramatically with the invention of the atomic force microscope (AFM) [24], and its subsequent development into a standard surface science tool, which made the field of nanotribology accessible to researchers: A sharp tip (radius 5 - 100 nm), i.e. a single asperity contact, mounted at the end of a leaf spring lever (triangular or bar shaped), is raster scanned across the sample and topographic information is obtained by measuring the deflection of the lever perpendicular to the sample. This is now most commonly achieved with an optical detection scheme [25]: A laser beam is focused onto the back of of the lever and reflected onto a four-quadrant photo-detector (see Figure 1.1). The difference signal between the top and bottom segments contains the topographic information, while the "left" and "right" segments allow the simultaneous recording of lateral forces twisting the tip sideways during scanning.

AFMs can be operated anywhere from ultra high vacuum (UHV) to ambient pressures and above, in various atmospheres, even in liquids. Through AFM measurements under perfectly clean conditions in UHV frictional properties of single asperity contacts are accessible and have already led to genuine new insights of friction at the atomic scale: At the atomic scale friction does indeed depend on the contact area [26], and on the sliding velocity [27].

Two key elements vital to the success of the AFM technique are micro-fabricated tip-lever as-

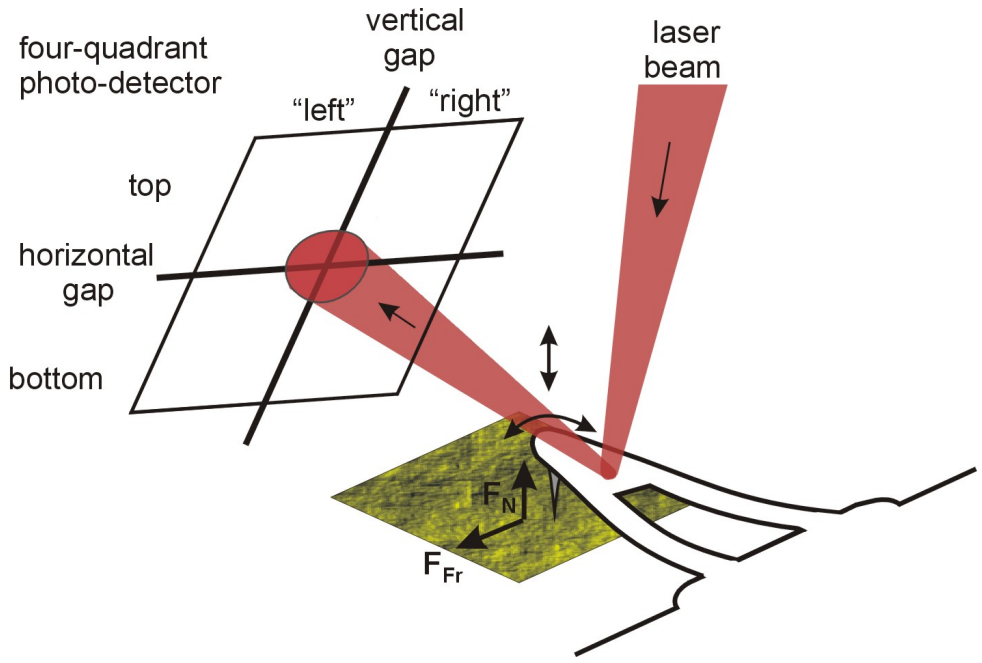

Figure 1.1: The operating principle of a beam deflection AFM. The incident laser beam is focused onto the reflective back of the lever. From there the laser is reflected into a four-quadrant position sensitive photo-detector. When the tip is brought into contact with the sample the lever will be bent upwards (or downwards for attractive forces), for small deflections following Hook's law. Thus the laser spot on the photo-detector moves towards the top segments (i.e. bottom segments, respectively) and a voltage difference proportional to the deflection of the lever can be measured. During scanning there are lateral forces acting on the tip, which cause the lever to twist and create a voltage difference between the "left" and "right" segments. Here a triangular lever is shown, which is commonly used for contact measurements. The first levers were bar-shaped, and this is still the preferred type for tapping applications.

semblies and piezo-electric ceramic materials. The former will be discussed in more detail in section 2.1.1, for now it is sufficient to note that the knowledge of etching three-dimensional structures out of silicon and silicon-nitride, obtained from the semiconductor industry, enabled the mass-production of tip-lever assemblies (for simplicity referred to as "cantilevers"). Furthermore they are sold with a variety of coatings, e.g. platinum to obtain a conductive probe or tungsten-carbide for increased hardness, opening the door for a nearly unlimited number of possible applications and promoting AFM within a decade to a routine surface analysis tool, sold by several companies[1]. Piezo-electric materials allow the positioning and relative motion of tip and sample with subatomic resolution. These materials have a polar axis, i.e. dipole moments oriented along this axis, will respond with a mechanical deformation to an applied electric field and vice versa. Because the dipoles which are lined up along the axis are attracted to each other, adjacent layers will be deformed until elastic forces counteract the electrostatic ones. Such a material, which most people have used without knowing, is quartz: It is used for tuning forks in quartz watches. A small AC voltage, oscillating with the resonance frequency of

[1]to name a few: Digital Instruments (DI), Santa Barbara, CA, USA, www.di.com
ThermoMicro (former Park Scientific), Sunnyvale, CA, USA. www.thermomicro.com
Omicron, Taunusstein, Germany, www.omicron.de
Asylum Research, Santa Barbara, CA, USA, www.asylumresearch.com
Molecular Imaging (MI) Corporation, Phoenix, AZ, USA, www.molec.com

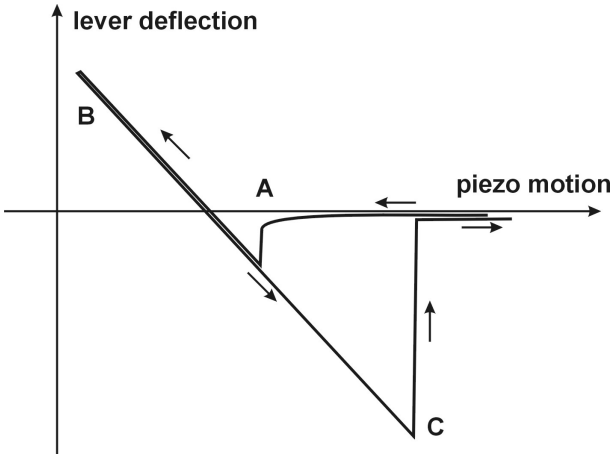

Figure 1.2: A typical force vs. displacement curve during an approach-retract cycle. The lever deflection is recorded while tip and sample are brought into contact and separated again. As long as tip and sample are separated, the free lever is not deflected. When tip and sample are brought into close proximity (A) the lever "feels" an increasingly attractive force, caused by long range electrostatic or van der Waals forces, and is bent down towards the sample. When the force gradient exceeds the spring constant of the lever, an instability, the so called "jump-to-contact", occurs, and the tip abruptly contacts the surface. Upon further approach, the lever experiences a repulsive force and is bent upwards (B), for small deflections following Hook's law. Upon reversal of the piezo motion the deflection signal follows the previous path. But adhesive forces, e.g. caused by a water meniscus condensed around the contact between tip and sample, will keep the tip in contact with the sample until the elastic force of the lever exceeds the adhesion and the lever snaps out of contact (C).

the tuning fork, is applied to electrodes on the faces of the quartz and it excites the tuning fork to resonate at its Eigenfrequency. Thus the tuning fork stabilizes the frequency of the whole circuit. Besides certain minerals there are also piezo-electric ceramics which can be formed into a variety of shapes. An everyday application for these materials is the positioning of the ink spouting nozzles of inkjet printers. For a resolution of 600 x 600 dpi the area per pixel is about $40 \times 40\ \mu\text{m}^2$ where a misalignment of $\pm\ 1\,\mu$m still would not be noticeable by eye. In an AFM, much lower tolerances are required to achieve subatomic accuracy in positioning and moving tip and sample relative to each other. Lead-zirconate-titanate ceramics have a typical expansion coefficient (perpendicular to the applied electric field) of the order of 1 Å/V. To obtain a reasonable scan area size (up to a few microns) and sub-Ångstrom resolution, the most suitable shape for scanning probe applications is a tube. Four outer quadrants and one inner electrode allow motion in x, y and z-direction using the leverage of the tube length to increase the motion per applied volt by a factor of 100 to typically[2] 10 - 20 nm/V.

Besides topography imaging and friction measurements, various other properties can be probed by an AFM. One, which is important for the work presented here is the measurement of adhesive forces between tip and sample. Under ambient conditions a water meniscus condenses around the contact area, providing an additional adhesion, which has to be taken into account to obtain the total force the tip applies to the sample. Figure 1.2 shows a typical force vs. displacement curve, from which the adhesive force can be obtained. The lever deflection is recorded while tip

[2] values obtained for a length of 1 inch, wall thickness of 0.02 inch, diameter of 0.125 to 0.5 inch for materials EBL #2 and #3, Staveley Sensors, E. Hartford, CT, USA. www.staveleyndt.com

and sample are brought into contact, and separated again. As long as tip and sample are far apart, the free lever is not deflected. When tip and sample are brought into close proximity, the lever experiences an increasingly attractive force, caused by long-range electrostatic or van der Waals forces, and is bent down towards the sample. When the force gradient exceeds the spring constant of the lever, an instability, the so called "jump-to-contact", occurs, and the tip abruptly contacts the surface (A). Assuming the tip does not penetrate the sample surface, upon further approach the lever experiences a repulsive force and is bent upwards (B), for small deflections, following Hook's law. Upon reversal of the piezo motion the deflection signal follows the previous path, but adhesive forces, e.g. caused by a water meniscus condensed around the contact between tip and sample, will keep the tip in contact with the sample until the elastic force of the lever exceeds the adhesion, and the lever snaps out of contact (C). The slope of either the repulsive (B) or the attractive linear region (before C) corresponds to the deflection sensitivity, i.e. the voltage difference at the photo-detector per z-motion of the piezo. Together with the lever force constant the deflection sensitivity yields the conversion factor to convert the voltage difference at the detector into applied force. With this knowledge, the maximum adhesive force can be calculated from the maximum negative deflection in point (C). This adhesive force has to be added to the force setpoint to obtain the effective total load applied to the sample. Such force vs. displacement curves can be taken e.g. at different locations on samples with inhomogeneities, or as a function of humidity, temperature, etc.

To minimize adhesive forces due to a water meniscus around the contact area, some AFMs allow to immerse tip and sample into a liquid (generally water) making it possible to image fragile structures without destroying them. Also most biological specimen, which can only be investigated *in vivo* in liquids, call for such a setup.

Furthermore, with force vs. displacement curves, bond breaking forces can be measured: Biomolecules such as DNA [28] can be forced to form a connection between the tip and sample, which is subsequently stretched and released to measure forces, relaxation time scales, velocity dependence and other properties of interest.

Normal elasticity and lateral stiffness can be probed by bringing the tip into contact with the sample, modulating either the normal or lateral position of the tip and measuring the response.

Beyond these contact mode techniques, there is an even bigger number of intermittent or non-contact measurements with a reputation of being less or not at all destructive for soft samples. For these techniques the distance between tip and sample is modulated, and only for a fraction of the modulation cycle the tip actually contacts the surface. Lock-in techniques have to be applied to compare the excitation signal with the response to obtain information about topography and other properties. True non-contact modes usually exploit long range electrostatic forces. One of these techniques, which has been applied in this work, will be discussed in detail in section 2.3.

1.3 Layers of Organic Molecules as Lubricants

The field of organic multi- and monolayers has exploded over the last few years, due to potential applications for non-linear optics [29], as photoresists [30] and biosensors [31], for membrane modelling [32] and also as lubricants, on which the focus of this work is placed.

Long hydrocarbon chains as lubricants are already known for centuries, if not millennia. Everyone knows that not changing the oil in your car will have devastating consequences for the engine. Much less known is the amount of research big oil and car companies put into the research of oil additives to improve their lubrication properties [33].

But the development of new technologies has created new demands for lubricants, going far beyond what "common oil" and its relatives can provide.

Once again, the driving force is the computer industry. The manufacturers of magnetic storage media are constantly trying to increase the amount of data, which can be stored on ever smaller

devices. To accomplish a higher bit density, the read/write-heads are getting smaller and also closer to the magnetic discs. The lubricant layer on the disc, which has the main purpose of keeping the head from crashing onto and sticking to the disc, subsequently has to get thinner. So far the lubricants are complex tailor-made molecules, the exact composition usually a patented secret, with a consistency somewhere between liquid and solid, bound rigidly enough to the surface so they do not spin off during the operation of these fast turning devices, but fluid enough so they will recover by "flowing" back in the case the head has touched the surface. Exactly these liquid like properties become increasingly troublesome for extremely thin layers, where the interaction is governed by intermolecular forces. Now de-wetting instead of re-wetting becomes a more likely alternative after a "touch down" [34]. There will obviously be a limit to how thin these layers can be made and the need for a new lubricant will arise.
There are already devices with dimensions far smaller than today's magnetic storage media: micro-electro-mechanical systems (MEMS). Micrometer sized gears etched from silicon are prototypes of a whole new industry of micro-machines[3]. And they also demand a whole new type of lubricant, one that is only one molecular layer thick, two layers at the most.
Hydrophobic monolayers of alkyltrichlorosilanes have already been successfully applied to reduce (i) the capillary forces of water during the final rinse of the etching process of three-dimensional silicon structures, and (ii) stiction and friction during operation of micrometer sized gears [3].
Another application, which may appear trivial at first glance, is the application of toner to paper in photocopying-machines. But to cause the toner particles to form an image of the object placed in the copier on the cylinder and subsequently to transfer these particles with a minimal loss onto paper, where they should remain even under the influence of liquids from marker pens, is a non-trivial problem, tackled in company owned research laboratories [35].
Although monolayers of organic molecules have been used as lubricants, the mechanisms by which energy is dissipated have been elusive.
Thanks to the AFM, there have been many advances in understanding the tribological behavior of monolayer thick lubricants. For example the frictional properties of self-assembled alkylsilanes and alkylthiols have been correlated with their chain length [13] and terminal group [36]. In this work, a connection between structural molecular changes and energy dissipation mechanisms will be established.

1.4 Preparation of Organic Monolayers

There are two techniques to obtain mono- or multilayers of organic molecules on a solid substrate: Langmuir-Blodgett (LB) films and self-assembled (SA) monolayers.
For a Langmuir-Blodgett film of the simplest kind, amphiphilic molecules, i.e. molecules with a hydrophilic head and a hydrophobic tail, e.g. fatty acids, in a dilute solution with a volatile solvent are spread usually onto a water surface (so called subphase) in a trough. One or two movable barriers limit the area of the air-water interface. The solvent is allowed to evaporate, before the barriers are set into motion, compressing the molecules on the water into a highly ordered monolayer of densely packed molecules, with their heads towards the water and the tails straight up. To measure the surface pressure changes during the compression, the force exerted on a hydrophilic plate (so called Wilhelmy plate), or a piece of filter-paper, is measured by an electrobalance or a sensitive spring. An example of a typical surface pressure vs. area isotherm is given in Figure 1.3(a). The molecules can go through several phase transition, of which only the most common ones shall be mentioned briefly here. The loosely packed disordered phase corresponding to the first increase in surface pressure is referred to as the liquid expanded (LE) phase. Before reaching the liquid condensed (LC) phase of highly ordered, maybe tilted, and densely packed molecules, there is a coexistence region in between [plateau in Figure 1.3(a)],

[3]CSEM, Switzerland, is advertising optical MEMS, on a "if you need it, we can build it" basis.

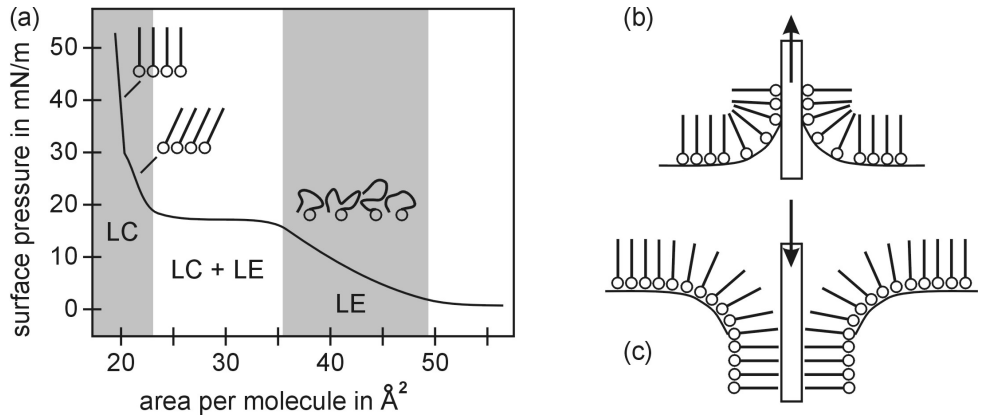

Figure 1.3: (a) A schematic drawing of a typical surface pressure vs. area isotherm for a Langmuir-Blodgett film. During a compression cycle on the water subphase the molecules can go through several phase transition: The loosely packed disordered phase, corresponding to the first increase in surface pressure, is referred to as the liquid expanded (LE) phase. Before reaching the liquid condensed (LC) phase of highly ordered, maybe tilted, and densely packed molecules, there is a coexistence region in between [plateau in Figure 1.3(a)], where the surface pressure does not increase significantly while islands of LC-phase molecules grow on the expense of the surrounding sea of LE-phase molecules. (b) Transfer of a compressed monolayer onto a hydrophilic substrate. (c) Transfer of a compressed monolayer onto a hydrophobic substrate.

where the surface pressure does not increase significantly while islands of LC-phase molecules grow on the expense of the surrounding sea of LE-phase molecules. A hydrophilic substrate, e.g. mica, which is immersed in the water before spreading the molecules, is "pulled" up through the film, which will deposit on the substrate [see Figure 1.3(b)], while the barriers will continuously keep the monolayer on the water compressed. Moving the substrate after the deposition of a monolayer again down through the monolayer and so on will result in multi-layers. There are many more variations for deposition on hydrophobic substrates [e.g. see Figure 1.3(c)], deposition of layers with identical orientation of the molecules or of layers of different molecules on the same substrate. An overview of the vast variety of LB-films can be found in the book by Ulman [37] and also in two reviews of LB-film structure in general [38], and of scanning probe techniques applied to investigate LB-films [39].

Note, that surfactant molecules with intermolecular forces beyond van-der-Waals forces, especially ones with the capability of a cross-linking reaction between the heads, are likely to yield different results as the ones described here.

Certain organic molecules in a dilute solution will spontaneously absorb and organize onto a solid substrate to form a so called self-assembled monolayer (SAM). This process is driven by the interaction of the head-group with the substrate, while for LB-films such an affinity is not necessary, although useful to increase the stability of the layer. There is a variety of head-groups and substrates, which will form either silicon-oxide, covalent or ionic bonds, promoting a strong attachment of the film to the substrate. The most widely known are thiols on gold and silanes on silicon, glass or mica. Despite an explosive increase in research on self-assembled layers since the early 1980's, an exact quantitative understanding of self-assembled monolayer formation mechanisms remains elusive. A model for monomer adsorption and subsequent 2D diffusion given by Doudevski *et. al.* [40], which was successfully applied by the authors to octadecylphosphonic acid adsorbed onto mica, does not accommodate the influence of molecules with a reactive headgroup such as trichlorosilanes, i.e. it does not include oligomers already

assembled in solution prior to adsorption. Many approaches have been undertaken recently to isolate the influence of factors such as solution temperature [41, 42], substrate properties [43] (modified by specific treatments [44]), solvent, solution age and water content [45, 46]. The following results for the self-assembly of octadecylsiloxane on silicon and mica give a qualitative insight into some aspects involved and illustrate the complexity of the process. In general self-assembly is accomplished by two competing mechanisms: The adsorption of a disordered liquid-like phase (comparable to the LE-phase of an LB-film) and an island-type growth, where the molecules are highly ordered and densely packed within the islands (comparable to the LC-phase of an LB-film). The solution temperature is one of the parameters to control the balance between these two growth types. Low temperatures favor pure island type assembly, while with increasing temperature the island size decreases and the space in between the islands will be filled by a liquid-like phase, up to a point where only liquid-like adsorption takes place. Another parameter, which has only lately received attention, is the water concentration of the solution and its age. Vallant *et. al.* [45] found that increased water content and age of the solution will favor the island type growth. The authors suggest that this is due to oligomers and similar "pre-assemblies" already formed in the solution.

Since the goal of this work is to investigate frictional properties of self-assembled monolayers and not their formation mechanisms, this shall suffice as introduction to the topic.

Both techniques, Langmuir-Blodgett films and self-assembled monolayers have the same problem: Pinholes and similar defects can never be completely avoided over large areas. However, the LB-technique has been employed successfully for non-tribological applications such as biosensors [31]. A significant impediment towards any massproduction involving LB-films is the necessary size of a trough to coat, e.g., just one four-inch-waver. Furthermore LB-films require a flat sample surface, which is not the case for MEMS. Self-assembly on the other hand can be easily included into the fabrication process for MEMS, since it is just another step in a sequence of various etching and rinsing procedures.

For the measurements presented in this work self-assembly was preferred over the LB-technique for several reasons, which will be explained in detail in chapter 4.

Chapter 2

Instrumentation

The goal of this work is to investigate the frictional properties of model lubricants under typical conditions and relate them to structural changes within the monolayer. As already discussed in the introduction, the atomic force microscope is the perfect tool to measure friction and topography at lateral dimensions of the order of tens of nanometers up to micrometers. To achieve a height resolution better than 1 Å, which is necessary to detect conformational changes of the molecules, the instrument should be compact, with an excellent vibration isolation and have a low-noise control electronics.
Since typical devices to be coated with such lubricants are intended for use in clean and low humidity environments, but not in vacuum, the following measurement can be performed under ambient conditions, i.e. at temperatures between 20°C and 25°C and at a humidity from 30 % to 50 %. Although the high humidity does not correspond to ideal operating conditions, it is often used as a means to simulate the accelerated aging, sometimes together with elevated temperatures.
The following section describes the setup which was used for this work, and has already proven its capabilities in various similar measurements [13, 47, 48, 49]

2.1 The AFM Setup

All results presented in this work were obtained on a home-built atomic force microscope (AFM) [50], operated by a commercial control electronics[1] interfaced to a PC. It is based on the beam deflection scheme (see Figure 1.1), to detect the vertical displacement and horizontal twist of a sharp tip at the end of a cantilever (leaf spring): The light from a laser diode is focused onto the reflective back of a cantilever under which the tip is situated, and reflected into a position sensing four-quadrant photo-detector.
A schematic drawing of the AFM is shown in Figure 2.1[2]. In Figure 2.2 a photo, taken from the left relative to the schematic, shows the AFM "disassembled", as necessary to exchange the sample.
A laser diode (*) and respective optics are enclosed in a housing (1) at the top, held by a clamp ring on top of two crossed translation stages (2). The translation stages are cross-stacked to form a two-axis positioner, thus the laser spot can be moved in x and y direction to be aligned on the AFM tip. Note that the translation stages are mounted at a slight angle (5 - 10 degrees off the horizontal), so the light of the laser does not shine perpendicular onto the sample. This avoids backscattering from reflective samples into the laser diode, which would destabilize the laser. The chip with the AFM tip attached to a lever (3) (see section 2.1.1), is clamped into the tip holder (4) by a spring, permitting an easy exchange of tips. The tip holder itself is

[1] STM100 and AFM100 from RHK Technology, Troy, MI, USA. www.rhk-tech.com
[2] a list of suitable parts can be found in Appendix B

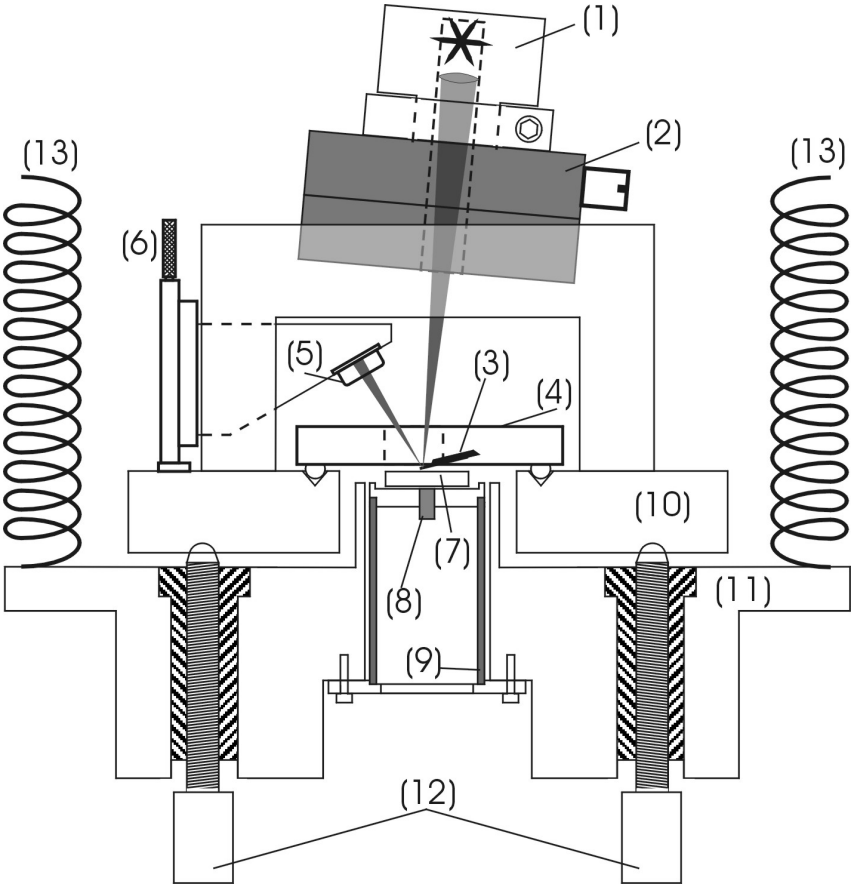

Figure 2.1: A schematic drawing of the AFM setup, not to scale. For a description of the components see text. Electrical connections are not shown.

clamped down into a three-point-bearing on the upper base plate (10). The laser is reflected off the back of the lever and into the four-quadrant photo-detector (5), which is also mounted on two crossed translation stages (6) to position the detector at the center of the laser spot. The sample, mounted on a magnetic puck (7), is held by a magnet (8) on top of the piezo (9), which is glued onto a holder plate and screwed into the bottom base plate (11). Three fine-threaded screws (12) with ball bearings atop, one controlled by a stepper motor, are used to approach the tip towards the sample. The top portion, called the head, which consists of all parts including and above the upper base plate (10), is made of brass wherever possible, so its weight is sufficient to hold it in a stable position atop of the screws. However, springs can be attached between the upper and the bottom base plate, which protect the head from being knocked over accidentally, but they do *not* improve the performance. The whole setup is suspended from rubber bands, represented by springs (13), for vibration isolation.

The alignment of the laser onto the cantilever takes some practice, since this compact arrangement of the components does not leave much room for an optical microscope. Instead a little piece of paper is placed approximately at the position where the photo-detector will be positioned later on. Although it is possible to leave the detector in its position during the alignment, it greatly hinders the view of tip and sample. From the shape of the reflected spot on the paper piece the position of the laser spot on the lever can be easily determined and adjusted with the two translation stages (2). A well focused laser beam has a spot size of 10 - 30 micrometer at the lever position, thus there should be no light spilling over the corners of the lever and a mostly

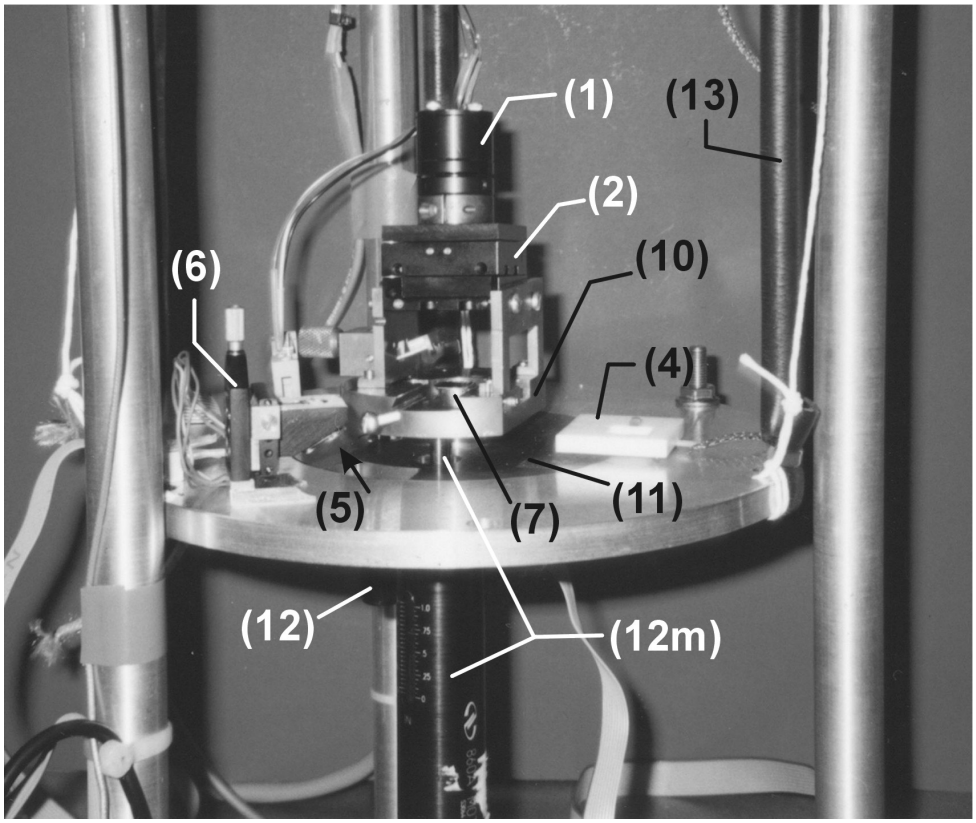

Figure 2.2: A photo of the AFM setup. The numbers correspond to those given in the schematic drawing of Figure 2.1 to the extend the components are visible here.

circular spot[3] should appear on the paper. When moving in x- or y-direction first some light is scattered at the corner of the lever and adds a "streak" to the spot on the paper, before the spot quickly disappears. For narrow levers it is possible that these "streaks" caused by scattered light do not disappear completely, but the remaining pattern should be symmetric.

Once the laser is aligned on the lever, the coarse approach using the (motorized) screws is performed. Afterwards the photo-detector is moved back into its position inside the upper base plate and locked there with a set screw. With the second set of translation stages (6) the photo-detector is positioned so the laser spot hits the center of the detector. The control electronics allows an offset to be added to the difference signals from the detector, which corresponds to a fine adjustment. Thus the positioning by means of the translation stages does not have to be perfect, but more important this offset allows for corrections due to drift.

The sample is held on a magnetic puck with double sided carbon tape, which is commonly used for vacuum applications, such as XPS, SEM and similar. It does not outgas significantly in vacuum, a treat not necessary for this work, but furthermore it is fairly conductive to prevent the sample from accumulating charge (note: the magnet holding the sample is grounded), and the tape's relaxation time is around 10 minutes, compared to conventional (office use) double sided sticky tape, which causes the sample to drift in the z-direction for at least 1 hour.

In this setup the sample is scanned with a single tube scanner, with an effective maximum range of 6.5 μm x 6.5 μm. While the nominal values for tube material (EBL # 2) and its dimensions yield a maximum range of 4.3 μm x 4.3 μm, the leverage of the sample puck with a

[3]The shape of a beam from a diode laser will always be somewhat stretched due to the rectangular dimensions of the active area inside the diode, typically 3μm x 10 μm

height of approximately 6 mm increases the effective area. The main advantage of scanning the sample is that the alignment of laser, tip and detector is not disturbed by scanning, and that a single piezo tube scanner is sufficient. The only other type where this alignment stays fixed, is the"walker" type AFM: Detector, tip and laser have to fit onto a "base" with a diameter of approximately 1.25 inch which is supported by three piezo tubes, which are altogether referred to as the head. The sample is mounted at the center of a circular holder which has three sectors of 120° containing a ramp each. The head is placed onto the sample holder in a way that each piezo is positioned on one ramp. Thus applying a saw-tooth voltage to the appropriate segments of the piezos, the head performs a circular motion due to its inertia and "walks" down the ramp to approach tip and sample. For details see Dai *et. al.* [51].

The tip holder is made out of macor, a very hard ceramic material, with an inlaid metal plate above the tip, onto which the tip is clamped by a spring loaded tungsten wire. A flexible shielded wire is attached to the metal plate to apply a bias voltage to the tip. Such a bias voltage is necessary for the SPFM technique described in detail in section 2.3, but it can also be used to quickly *and* safely approach the tip towards the sample surface: An AC voltage (with a frequency on the order of kHz and an amplitude of the order of V) applied to the tip, will have no effect on the lever deflection, as long as the tip is far away. But for small separations of tip and sample the lever is deflected due to electrostatic forces caused by mobile and static surface charges on the sample. The lever will respond with an oscillation, which increases its amplitude rapidly with decreasing separation (for a detailed explanation see section 2.3). Thus the tip can be quickly lowered onto the sample with the approach screws until the oscillation appears in the normal deflection signal. Afterwards the tip is brought into contact with the motorized screw using the smallest possible step size of the motor.

The whole AFM, as shown in Figure 2.2, plus the preamplifier for the signal from the photo-detector and power-supply for the laser diode, are enclosed in a plexiglass box, which allows to control the humidity during measurements. By introducing desiccant into the box and constantly flushing with dry nitrogen, the humidity can be lowered to less than 10 % within one hour. The opposite can be achieved with a beaker of hot water and nitrogen bubbled through water to reach a humidity of up to 90 %.

The electrical connections, not shown in Figure 2.1, consist of flexible ribbon cables: one for the voltages to the segments of the piezo, one for the the laser diode and one for the signals from the four-quadrant photo-detector. These ribbon cables do not interfere significantly with the vibration isolation.

The processing of the signals from the photo-detector is performed by a special analog AFM electronics module, which receives the voltages from the four segments of the detector as inputs and calculates the difference signals: The normal deflection corresponds to the difference of the two top segments minus the two bottom segments, and the lateral deflection corresponds to the difference of the two "left" minus the two "right" segments (see Figure 1.1). In addition, the AFM module allows to add offsets to the normal and lateral deflection signals to adjust for a not perfectly centered laser spot on the detector, but also to adjust the force setpoint at which the feedback is maintained. The feedback adjusts the position of the sample so the tip is applying a constant force, i.e. the lever deflection is kept constant. Almost any point on the force distance curve, see Figure 1.2, between the "jump-to-contact" (A) and "pull-off" point (C) can be chosen as setpoint. Close to the "pull-off" one risks to loose feedback during a scan. To scan at a constant oscillation amplitude of the lever as for SPFM (see section 2.3), the deflection signal is processed by a lock-in amplifier, giving a DC output proportional to the amplitude, which will be kept constant by the feedback.

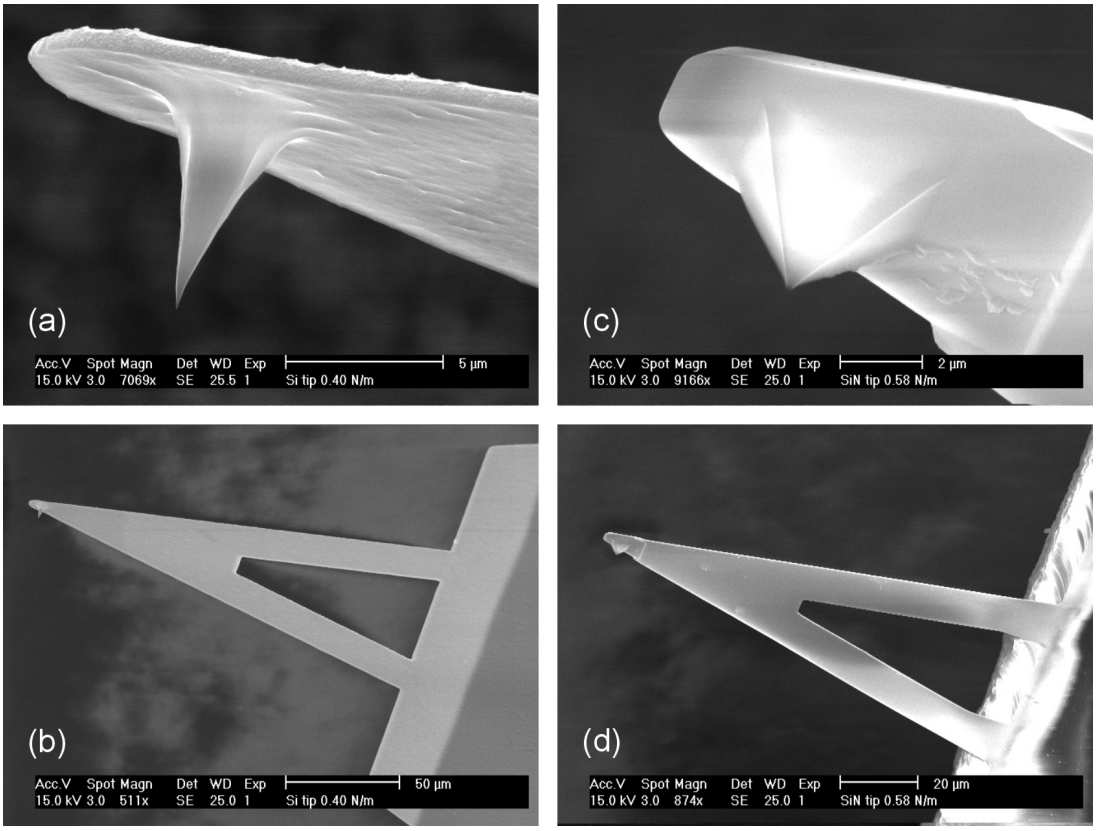

Figure 2.3: SEM images of typical AFM tips used in this study: (a) and (b) show a conical silicon tip with a nominal lever force constant of 0.4 N/m, (c) and (d) a pyramidal silicon-nitride tip with a nominal lever force constant of 0.58 N/m.

2.1.1 Cantilever

While in the early days of AFM cantilevers had to be made by the researchers themselves [52, 53], today a whole variety of different types of levers, tips and coatings is commercially available. From the basic materials silicon and silicon-nitride[4] simple bar-shaped or triangular levers are produced with conical or pyramidal tips, which can be especially "sharpened" or coated for conductivity, increased hardness or inertness.

For the measurements presented in chapter 3 and 5, triangular silicon cantilevers with a conical tip[5] were used, for those in chapter 4, triangular silicon-nitride levers with a pyramidal tip[6], see Figure 2.3.

As already mentioned in the introduction (section 1.2), to estimate the applied force, the normal force constant of the lever has to be known, at least approximately. For the following measurements the normal force constant was assumed to have the value given by the manufacturer, although there can be easily deviations of a factor of two.

There are various methods to determine the normal force constant experimentally, but most of them are difficult to perform:

[4] commonly referred to as Si_3N_4, although the relation between silicon and nitrogen can vary due to the CVD (chemical vapor deposition) production method.

[5] Ultralever, from former Park Scientific Instruments, now ThermoMicroscopes, Sunnyvale, CA, USA. www.thermomicro.com

[6] Nanoprobe lever, Digital Instruments (DI), Santa Barbara, CA, USA. www.di.com

- Considered to be most accurate but also destructive, is the added mass method, where spherical tungsten particles of a known mass, are attached to the end of the lever and from the shift in resonance frequency the force constant can be determined [54].

- Another way is to deflect the lever with a larger lever of known spring constant (typically of the order of a few mN), but this requires a special experimental setup and such a larger, calibrated lever [55].

- Furthermore the thermal vibration of the free lever can be used to obtain an estimate of the normal force constant [56]. Note, compared to the added mass method, there can be an error of up to 20 % [57] with this method.

- Finally, one can use the dimensions of the lever to calculate the normal force constant, but these calculations require elaborate numerical calculations and a detailed knowledge of the dimensions of the lever [58]. Note, that the lever thickness is a crucial parameter, because slight variations will have a significant effect, and so will any kind of coating, even if its thickness is known [59].

Of these methods only the last one can be also applied to calculate the *lateral* force constant of the lever. But even if the lateral force constant is known, the calibration of lateral forces, i.e. the conversion of the lateral deflection signal, is highly sensitive to the alignment of the lever on the tip, especially since the lateral sensitivity is usually 10 to 100 times lower than the normal sensitivity. Ogletree *et. al.* presented an *in situ* method to calibrate the lateral deflection signal also including the laser-detector alignment [60]. It involves scanning over a wedge sample with two differently sloped areas, e.g. a $SrTiO_3$ (305) crystal (see Figure 2.4). Such an elaborate and time consuming measurement is necessary for exact quantitative friction measurements [26]. For the measurements in this work an estimation using the lever dimensions (measured with an SEM, lever thickness by imaging a broken off lever with an AFM) of typical levers was sufficient, as shall be seen.
For many measurements it is important to know not only the applied force, but rather the pressure inside the contact area. To calculate the contact area one needs to know the tip radius. Although tip manufacturers give estimates on the tip radius, some deviations are possible and there is also a chance to find a defective tip. Since typical tip radii are on the order of 5 -100 nm, a high resolution SEM can be used to measure the radius, but not everyone has easy access (if at all) to such a machine. A much less costly alternative way to measure the tip radius is to invert the principle of AFM: Instead of imaging the sample with the tip, the tip can be imaged by a sample with an array of features sharper than the tip itself. Such features can be e.g. spikes, which will give a three-dimensional image of a tip. Figure 2.4(a) shows an image of a silicon-nitride tip obtained in this manner.
Also samples with sharp ridges, e.g. a $SrTiO_3$ crystal cut to expose the (305) surface or etched silicon can be used to obtain a two-dimensional estimate, i.e. a cross-section of the tip. With such samples a possible source for errors is that the tip might be a lot more blunt in the third dimension along the ridge. To exclude such a case the sample and scan direction have to be turned by 90° for another image. Figure 2.4(b) shows an image obtained on an etched silicon ridge sample[7] with an apex radius of $\sim$ 10 nm, Figure 2.4(c) shows another image obtained on $SrTiO_3$. Although the silicon samples will be initially more blunt than $SrTiO_3$ (freshly annealed in oxygen), the latter will degrade unless kept under perfectly dry conditions.
To assign a "radius" to a tip, the very end of the tip is regarded as a sphere. Since the most accurate way to measure is *along* an actual scan line [8], the problem can be reduced to two

[7] SiliconMDT, Moscow, Russia. www.siliconMDT.com

[8] Cross-sections over several scan lines can contain errors caused by misalignment of the scan lines relative to each other, depending on the way the data has already been processed.

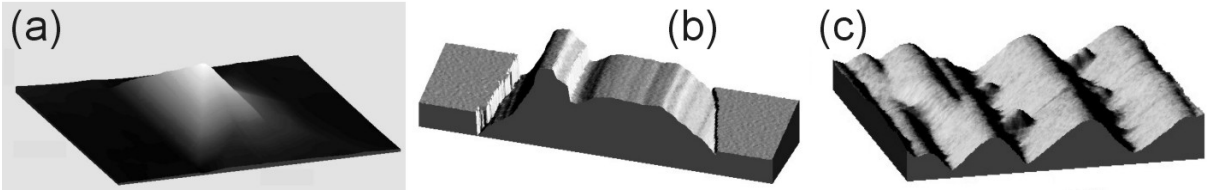

Figure 2.4: Example images of analysis gratings to measure the radius of an AFM tip: (a) Pyramidal silicon-nitride tip imaged with a sample which consists of an array of spikes sharper than the tip itself. Image size 2.0 × 2.0 μm^2, total height 0.76 μm (b) Cross-sections of a silicon tip obtained with an etched silicon sample, which consists of sharp parallel ridges (apex radius $\sim$ 10 nm), clearly exposing a double tip. Section length 0.5 μm, total height 50 nm. (c) Cross-sections of a silicon-nitride tip obtained on a $SrTiO_3$ (305) crystal. Image size 400 × 400 nm^2, total height 11.0 nm

dimensions, reducing the sphere to a circle. The equation of a circle with radius R around the origin (0/0)

$$f(x) = \sqrt{R^2 - x^2} \tag{2.1}$$

can be expanded into a Taylor-series around (0,R):

$$f(x) = R + 0 \cdot x - \frac{1}{2R} \cdot x^2 + 0 \cdot \frac{1}{6}x^3 - \frac{1}{8R^3} \cdot x^4 + O(x^6). \tag{2.2}$$

Neglecting the terms of forth order and higher leaves us with the equation of a parabola:

$$f(x) = -\frac{1}{2R} \cdot x^2 + R \tag{2.3}$$

Thus fitting a parabola through a cross-section of the image will yield the tip radius from the coefficient of the second order term.
Besides these methods, there is also the possibility of a "blind reconstruction" [61], which is a numerical method to obtain an upper limit for the tip radius from any AFM image with topographic features.

2.1.2 Calibration

For any AFM a careful calibration of the piezo motion is absolutely necessary. As already mentioned, the motion in x- and y-direction calculated from data sheets can change significantly due to an additional spacer between piezo and sample, e.g. the sample puck, which increases the leverage of the tube scanner. Unfortunately piezos are subject to creep, hysteresis and memory effects. The actual motion depends on the applied voltages, the scan speed and to a lesser degree the previously performed motion. These factors are extremely difficult to correct for all possible combinations of scan area size and scan speeds, which make it almost impossible to obtain a perfect calibration. An elaborate solution implemented in some of the commercial AFMs are "closed-loop scanners": Capacitance sensors measure the actual motion of the piezo(s) and a feedback loop corrects for any non-linear behavior. Such an additional feedback loop limits the bandwidth of the scanner and ultimately, the scan speed.
A simple way to solve this dilemma is to have several parameter files with different calibrations for the most common cases. It is important that the calibration samples have dimensions similar to those to be measured on the samples. For lateral dimensions on the order of micrometers and for heights on the order of some tens of nanometers, etched silicon samples are commercially

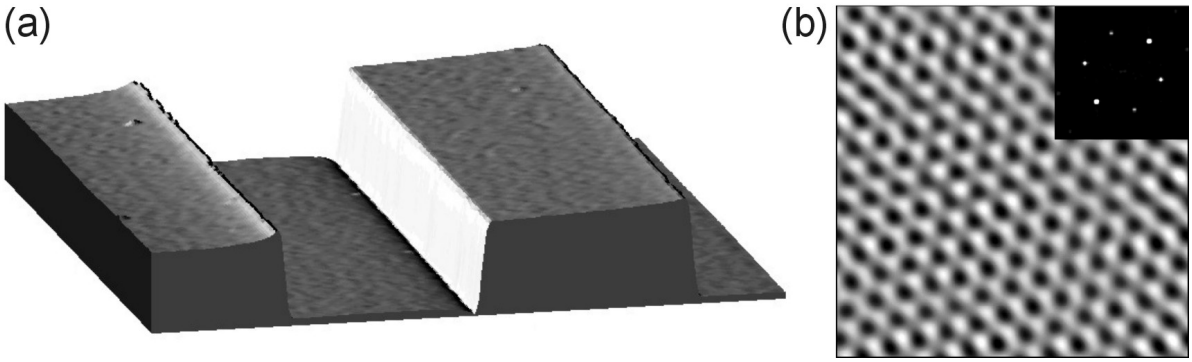

Figure 2.5: AFM images of (a) a commercial calibration grating with a periodicity of 3 μm and a height of 25.5 nm used for large scale calibration (image size 5.50 $\times$ 5.50 μm^2) and (b) the mica lattice with a lateral periodicity of 5.2 Å. Shown is the fast-Fourier filtered lateral force image and in the inset the two-dimensional fast-Fourier transformation.

available. For heights on the order of a few Ångstroms, layered materials, which have cleavage steps, e.g. graphite, or which can be removed with the AFM tip layer by layer, e.g. mica, are the ideal calibration samples. Furthermore, on mica atomic lattice resolution is easily obtained, with a well known hexagonal periodicity of 5.2 Å, suitable for a calibration for lateral dimensions of the order of 5 - 20 nm.
The samples investigated in this work required two sets of calibration parameters: One for monolayer islands with lateral dimensions of the order of micrometers and heights between 5 and 30 Å, and one for atomic lattice resolution for lateral dimensions of the order of 10 nm. An etched silicon grating[9] with a periodicity of 3 μm and a height of 25.5 nm provided the large scale lateral calibration and a first estimate for the height calibration [see Figure 2.5(a)]. For an accurate height calibration, mica was removed with a sharp tip layer by layer, leaving holes with depth of multiples of 10 Å. These holes were immediately imaged with the same tip (see also chapter 3). The lateral atomic scale calibration was obtained with mica [see Figure 2.5(b)]. Note, that the calibration should be checked once in a while, since piezoelectric materials depolarize due to aging or high electric fields.

2.2 Friction Measurements

Maybe "energy dissipation" would be the more appropriate term than "friction" for the following measurements, but on the other hand, "friction" is the term everyone is familiar with. Since the main goal of this work is to uncloak structural changes within a monolayer as channels for energy dissipation, a calibration of frictional forces is desirable, to make sure the involved energies are of the same order of magnitude. But it is not imperative to go through an elaborate procedure to obtain accurate quantitative friction forces.
To understand how friction data is acquired by AFM, one simply has to imagine the motion of the laser spot across the detector while the tip is scanned across the sample, i.e. here the sample is scanned underneath the tip[10]. Lateral forces will twist the lever, which will deflect the laser spot towards one side on the detector. Retracing the same scan line will twist the lever the opposite way and also move the center of the laser spot towards the other side of the detector. Figure 2.6(a) shows a schematic of a typical deflection signal during such a cycle. The steep

[9] SiliconMDT, Moscow, Russia. www.siliconMDT.com
[10] The fast scan direction has to be perpendicular to the long lever axis to obtain reasonable friction data.

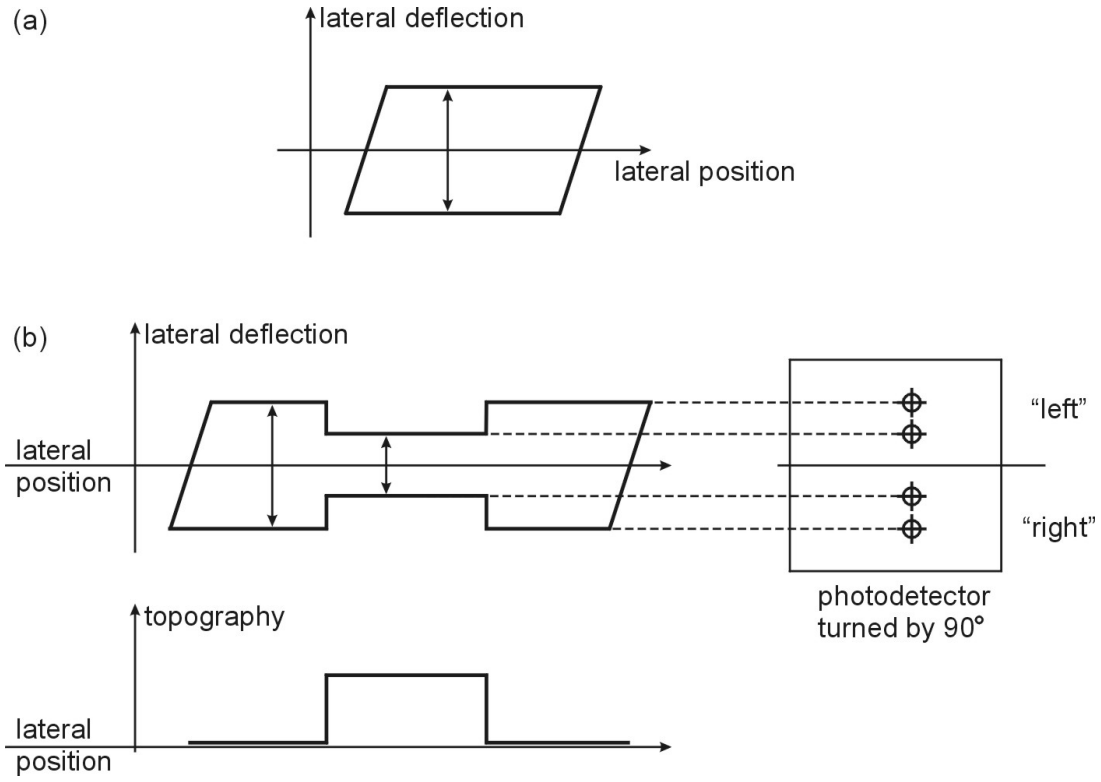

Figure 2.6: (a) Schematic of a typical lateral deflection signal during the course of a complete scan line, i.e. "forward" and "backward" scan across a homogenous sample. The steep regions are those of static friction when the lever motion reverses direction. When the force due to the torsion of the lever exceeds the static friction the tip begins to slide across the sample with a constant lateral deflection. (b) Lateral and normal deflection signal for an inhomogenous sample, i.e. one with an island of lower friction. Starting off the island, the laser spot is deflected by a certain amount, which will decrease, when the "lubricating" island is reached. Obviously, the width of the friction loop decreases. Looking at the lateral deflection images separately will create the impression of a "contrast reversal" between the two scan directions, see Figure 2.7.

regions are those of static friction when the lever motion reverses direction. The tip stays on the same spot on the sample, until the force due to the torsion of the lever exceeds the static friction and the tip begins to slide across the sample with a constant lateral deflection. Such curves are commonly referred to as friction loops. Attention has to be paid to the fact that the width of the friction loop corresponds to twice the frictional force. Using only one direction to extract the lateral deflection as difference to zero can easily lead to significant deviations: The lateral force constant of the lever is much higher than the normal, thus the lateral deflection signal is 20 to 80 times smaller compared to the normal deflection signal. A small drift of the lateral deflection signal can cause a significant shift of the friction loop, which would contribute to the "friction", if only one scan direction would be taken into account.

Samples of self-assembled monolayer islands of alkylsilane molecules on mica, which will be discussed in detail in chapter 4, show a contrast reversal between the two lateral force images with different directions, which is startling at the first glance, but can be readily explained as shown in Figure 2.6 (b). The islands are areas of lower friction, thus the lever is twisted less on those regions. Starting on a bare region the laser spot will be deflected by a certain amount to e.g. the left side of the photo-detector. Reaching the island, this amount will decrease, i.e.

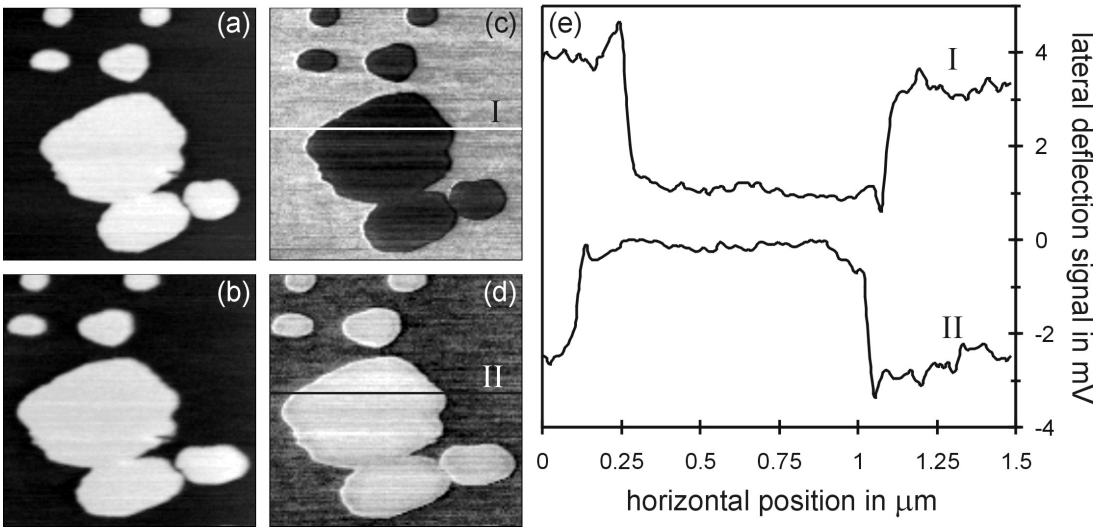

Figure 2.7: Typical topography and corresponding lateral force AFM images acquired on octadecylsilanol islands on mica. (a) and (b) show the "forward" and "backward" channel of the topography signal, lighter colors correspond to higher regions. There is a clear contrast reversal between the lateral force images (c) and (d), as explained in the text and Figure 2.6. The corresponding cross-sections marked I and II are shown in (e). Also there is a noticeable hysteresis effect between the "forward" and "backward" direction, which causes the islands to appear wider and displaced to the left in the images (b) and (d). Image size is $1.5 \times 1.5\ \mu m^2$.

the spot moves closer to the gap separating the "left" and "right" segments. When moving in the opposite direction, the laser spot will be mirrored at the gap between the segments. The result is the friction loop shown in Figure 2.6 (b). The width of the loop is clearly smaller in the island region, but regarding the top and bottom part separately gives rise to this apparent contrast reversal. As already mentioned, the width of the loop is a measure for the lateral force between sample and tip. For representative purposes the lateral force image acquired in the direction where the island appears "lower" is sometimes used, instead of the difference image of the two directions. In any case, it should be clearly stated which of the two is displayed. Figure 2.7 shows an example for the contrast reversal of lateral deflection images of octadecylsilanol islands on mica.

A misalignment of lever and detector in such a way that the laser spot will not move perfectly vertical on the detector, when only normal forces are acting, as e.g. during a force displacement curve, will cause a lateral contribution proportional to the normal deflection, see Figure 2.8. This can be corrected by adding a certain percentage of the normal deflection signal to the lateral deflection signal. The signals are perfectly decoupled, when the lateral deflection signal stays constant during a force displacement curve.

Two different methods were employed to obtain information about the frictional properties of the samples. The first will be referred to as "image by image", the second as "line by line".

For the island samples of chapter 4 it was advantageous to measure island height and friction at the same time and to be able to compare different islands at the same applied load. Thus the data was acquired "image by image", i.e. starting at a very low load close to the pull-off point, topography and lateral force images are acquired simultaneously, then the load is increased and again whole images are acquired. Before increasing the load even further, the sample is imaged again at the low initial load to see if any changes, which appear with increasing load, are reversible or not on the time scale of the experiment. The friction data can be extracted by

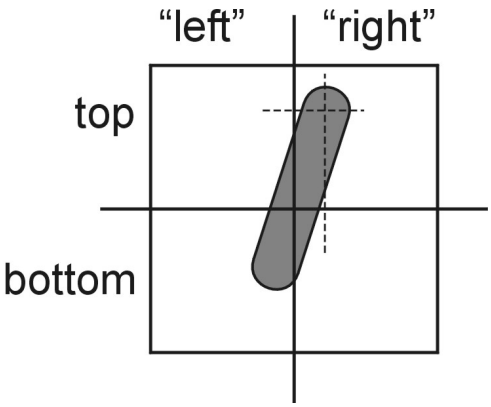

Figure 2.8: Schematic drawing to illustrate the coupling of Normal and Lateral Deflection Signal in AFM. Depicted is the area covered by the laser spot during a force vs. displacement curve with the lever misaligned relative to the detector. The laser spot does not move perfectly vertical on the detector, even though only normal forces are acting, causing a lateral contribution proportional to the normal deflection.

subtracting the lateral force images from each other and averaging over a homogeneous area on the island.

For samples covered by a homogeneous monolayer the simpler “line by line” method can be applied. Here the load is increased software controlled within one image from scan line to scan line up to half the total number of scan lines (typically 256) and decreased from line to line over the remaining half of the scan lines of this image. The data analysis is performed in a very similar way: The lateral force images are subtracted from each other, so each line of the resulting image corresponds to the width of the friction loop for a specific load. Neglecting the areas of static friction where the width of the friction loop is not yet constant, the values along one line are averaged and can be plotted vs the applied load to yield friction vs. load curves as presented in chapter 5. Here the reversibility can not be checked after each load, however, the branch where the load is decreased line by line can indicate permanent damage.

Compared to the “image by image” method where each data point on such a friction vs. load curve corresponds to one set of images processed to obtain the width of the friction loop at one load, the “line by line” method is definitely quicker. Unless there are good arguments as mentioned above for the “image by image” method, the “line by line” method is to be preferred.

Note on atomic lattice resolution: Is is a well known fact that layered materials, such as mica [53] and graphite, but also alkali halides [63] exhibit “atomic lattice resolution” in AFM. Atomic scale stick-slip processes take place between tip and sample, leading to a deflection of the lever, which is usually more pronounced in the lateral than in the normal direction [64], reflecting the atomic scale periodicity. This is stunning, since even for sharp tips and low loads in contact AFM measurements (in air and UHV), the contact area between tip and sample will always contain several unit cells. Although many approaches have been undertaken to explain this phenomenon ([5] and references therein), none so far has led to a satisfying theory. However, is is widely accepted that there is a periodic potential between (even incommensurate) tip an and sample, following the sample periodicity and giving rise to the stick-slip behavior. Such images, as shown e.g. in Figure 2.5(b), are referred to as “atomic lattice resolution” images, in contrast to “true atomic resolution”, defined by the capability to detect single atomic/molecular defects, which is usually accomplished only by intermittent contact modes in UHV [65] or contact mode imaging with soft levers in liquids [99].

2.3 Scanning Polarization Force Microscopy

Scanning Polarization Force Microscopy (SPFM) is a true non-contact technique to measure dielectric polarization forces on surfaces induced by a charged tip [66, 67, 68, 69, 70, 71, 72]. Note that in the literature, the same technique is sometimes also referred to as "Kelvin Probe Microscopy". At first glance, such a technique does not fit into the scheme of friction and wear, but on a second thought, as will be shown in chapter 3, it can be an excellent method to determine even minute wear damage caused by an AFM, without the risk of further eroding the surface [73].
Long range electrostatic forces are used to perform non-contact imaging not only of conductive, but also insulating materials. As shown by Hu *et. al.* [67] the attractive force between a point charge representing the tip and a substrate with dielectric constant ϵ, which has a film with dielectric constant $\tilde{\epsilon}$ adsorbed on it, can be given by

$$F = Q^2 \left(\frac{\gamma_1}{(2z)^2} + \sum_{n=0} \frac{(\gamma_1)^n (\gamma_2)^{n+1} [(\gamma_1)^2 - 1]}{(2z + 2H + 2nH)^2} \right) \tag{2.4}$$

where Q is the charge on the tip, z is the tip sample separation, H the height of the film, $\gamma_1 = (\tilde{\epsilon} - 1)/(\tilde{\epsilon} + 1)$ and $\gamma_2 = (\tilde{\epsilon} - \epsilon)/(\tilde{\epsilon} + \epsilon)$. This result was obtained using a simple image charge method. From Equation 2.4 it follows that the height of the film is magnified for $\tilde{\epsilon} > \epsilon$, and demagnified for $\tilde{\epsilon} < \epsilon$. Note that conductive silicon or silicon-nitride levers with a conductive coating are suitable probes for this technique.
Hu *et. al.* also proposed to use an ac-voltage instead of a dc-voltage to investigate the frequency dependance, but it also allows to separately measure static and mobile charge contributions, i.e. surface potential and dielectric polarizability.
Besides the exact explanation, which will be given in the following, there is also a more intuitive way to qualitatively describe the response of the tip with an ac-voltage applied to static and mobile charges on the sample surface (see Figure 2.9):
The force between a static charge on the sample and an ac-voltage applied to the tip will oscillate between repulsive, for equal signs, and attractive, for opposite signs, with the same frequency as the ac-voltage. Mobile charges, i.e. ions and dipoles, on the other hand, will flow towards or away from the tip or orient themselves in a way that the force will always be attractive for any sign of the ac-voltage, which will lead to a response with double the frequency.
For an ac-voltage applied to the tip, the force between tip and sample consists of two components:

- The derivative of the energy $\frac{dE}{dz}$, which is stored in the capacitor formed by the tip and the sample $E = \frac{1}{2}CV^2$, where C is the capacitance of the tip-sample geometry, which will depend on the separation z.

- The force between two point charges, which is according to Coulomb's law: $F = \frac{1}{4\pi\epsilon_0} \frac{Q_s Q_t}{z^2}$, where Q_s is the surface charge on the sample, Q_t the charge on the tip and z the separation between tip and sample. Q_t is given by the sum of the induced image charge of Q_s and the charge stored $(C \cdot V)$ in the tip due to the applied voltage V

$$F = \frac{1}{2} \frac{dC}{dz} V^2 + \frac{1}{4\pi\epsilon_0} \frac{Q_s(-Q_s + CV)}{z^2} \tag{2.5}$$

Furthermore, the bias voltage applied to the tip shall also accommodate a dc-component, for reasons that will be discussed in the following: $V = V_{dc} + V_{ac} \cos wt$. With $2\cos^2 wt = 1 + \cos 2wt$ the force F can be separated into terms which have a $\cos wt$ and a $\cos 2wt$ dependence:

$$\begin{aligned} F = \frac{1}{4} \frac{dC}{dz} V_{ac}^2 \cos 2wt + \left[\frac{dC}{dz} V_{dc} + \frac{Q_s C}{4\pi\epsilon_0 z^2} \right] V_{ac} \cos wt \\ + \frac{1}{2} \frac{dC}{dz} \left(V_{dc}^2 + \frac{1}{2} V_{ac}^2 \right) + \frac{Q_s}{4\pi\epsilon_0 z^2} (CV_{dc} - Q_s) \end{aligned} \tag{2.6}$$

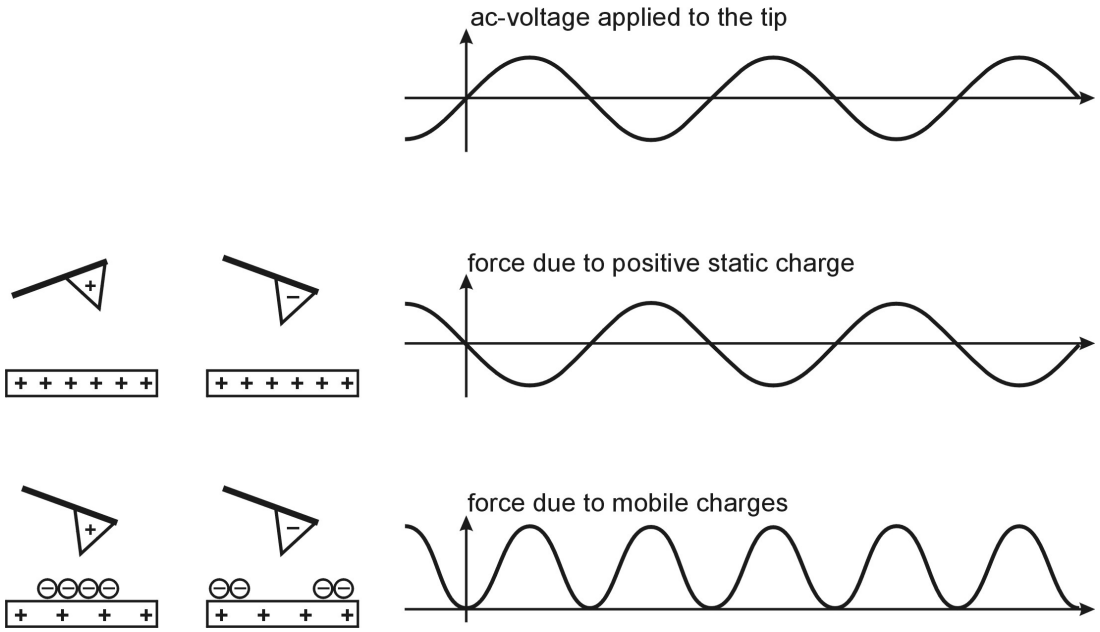

Figure 2.9: Schematic of an intuitive explanation for the ac-scanning polarization force microscopy technique. (top) ac-voltage applied to the AFM tip. (middle) The force between a static charge on the sample and the ac-voltage will oscillate between repulsive (for equal signs) and attractive (for opposite signs) with the same frequency as the ac-voltage. (bottom) Mobile charges will flow towards or away from the tip in a way that the force will always be attractive for any sign of the ac-voltage, which will lead to a response with the double frequency.

Technically the amplitude of the 2ω- and 1ω-term can be measured separately with two lock-in amplifiers and recorded by the electronics. The amplitude of the 2ω-term depends only on the derivative of the capacity, i.e. it will be constant for a fixed separation z unless the dielectric properties change. Reversing this thought, the amplitude of the 2ω-term can be used as feedback parameter, since it will keep the separation z constant as long as the dielectric properties on the sample are the same all over the scan area, simply following the topography of the sample. Note, that since the feedback will keep $\frac{dC}{dz}$ constant, changes of the dielectric properties of the sample will cause topography artefacts! The amplitude of the 1ω-term appears to be more complicated, but since V_{dc} is constant and $\frac{dC}{dz}$ is kept constant by the feedback, changes of the 1ω amplitude are due to changes in the surface potential ϕ $(= Q_s C)$. Note, that there is no specific model for the capacitance applied for this calculation.

Surface potential changes during an image can be calibrated by acquiring an additional image over an area, where the scan area is limited to a region with constant surface potential. Changes of the dc offset voltage V_{dc} (applied to the tip) by a certain amount correspond to changes of the surface potential by the same amount. Thus changing V_{dc} every few scan lines by a certain amount allows to calibrate the surface potential changes recorded in the 1ω image. It is evident that an image and its corresponding calibration image have to be acquired at the same tip sample separation z.

The frequency of the applied ac-voltage must not coincide with the resonance frequency of the lever (or half its value), so the lever is excited off resonance at an amplitude of typically 1 - 3 nm. The average tip position is considered as separation z, since the oscillation amplitude (typically on the order of 1 nm for our experiments) is small compared to the tip sample distance of usually 20 - 50 nm. The separation of tip and sample should not be decreased below a point,

where a contact between features on the sample and the tip becomes likely during scanning. Since the amplitude increases with decreasing separation, a contact with the sample will lead to a devastating crash, because the amplitude will be immediately zero, which causes the feedback to move tip and sample even closer, ultimately ramming the tip into the sample surface. Beyond the risk of a crash, for smaller distances the air cushion between the tip and sample starts to damp the oscillation and will introduce a phase shift, depending on the ability of the lock-in amplifiers to exclude such phase shifts from the amplitude signal. However, the separation between tip and sample also limits the lateral resolution to approximately the same value of 20 - 50 nm.

Chapter 3

Muscovite Mica

Mica is a sheet-silicate which is widely used as substrate for Langmuir-Blodgett films, self-assembled monolayers and other organic surfactant molecules to be investigated by atomic force microscopy or with the surface forces apparatus (SFA) [21]. It can be easily cleaved to expose atomically flat regions of hundreds of micrometers in size, which are extremely hydrophilic (contact angle of 0°) immediately after cleavage. The negatively charged surface is covered by Potassium ions which are displaced by positively charged surfactants. Although mica is transparent at a typically used thickness of 0.2 mm or less, its birefringence requires, to say the least, careful alignment of the optical axis for any optical measurements, as e.g. in SFA experiments. Beyond the use as a substrate mica is also an excellent calibration sample at the atomic scale (see Figure 2.5).

Furthermore, as will be shown in this chapter, new insights on friction and wear at the nanometer scale can be gained from atomic force microscopy on mica [74]. It can be shown that the production of surface defects at the interface of rubbing solids is an important mechanism of energy dissipation in friction. It will be demonstrated that defects produced by the rupture of silicon-oxide bonds at the surface, which are not visible in contact mode AFM images, have a noticeable contribution to friction. The contribution of defect production to friction will be explained by a simple model, which is based on the stress-induced enhancement of the rate of thermal defect production.

3.1 The Crystallographic Structure of Muscovite Mica

Since the structure of muscovite mica is crucial for understanding the results presented in this chapter, it will be discussed in this section and a sketch of it is given in Figure 3.1. Muscovite mica is a layered alumino-silicate. Complete formula units of $KAl_2(Si_3AlO_{10})(OH)_2$ are stacked in layers of 10 Å thickness. K^+ ions are located at the boundary of these layers, providing a weak electrostatic bonding. Thus they define the preferred cleavage planes. These planes expose oxygen atoms arranged in a hexagonal pattern with 5.2 Å periodicity formed by the bases of corner-sharing SiO_4 tetrahedra. This surface plane, labelled "S1" in the Figure 3.1, is typically imaged by contact mode AFM (see Fig. 2.5 b), while the potassium ions on top have not been imaged, presumably because they are randomly distributed or displaced during scanning. The second plane labelled "S2" is formed by the bottom oxygen atom of the SiO_4 tetrahedra and additional OH-groups. Figures 3.1 b and c present a top view of layer "S1" and "S2" respectively, which clearly shows that the periodicity of the second plane is reduced to 3.0 Å and the unit cell is turned by 30° relative to the one of the surface plane, due to the interspersed OH-groups. The "S2" plane is followed by a layer of aluminum atoms, which is also a mirror plane of the unit cell.

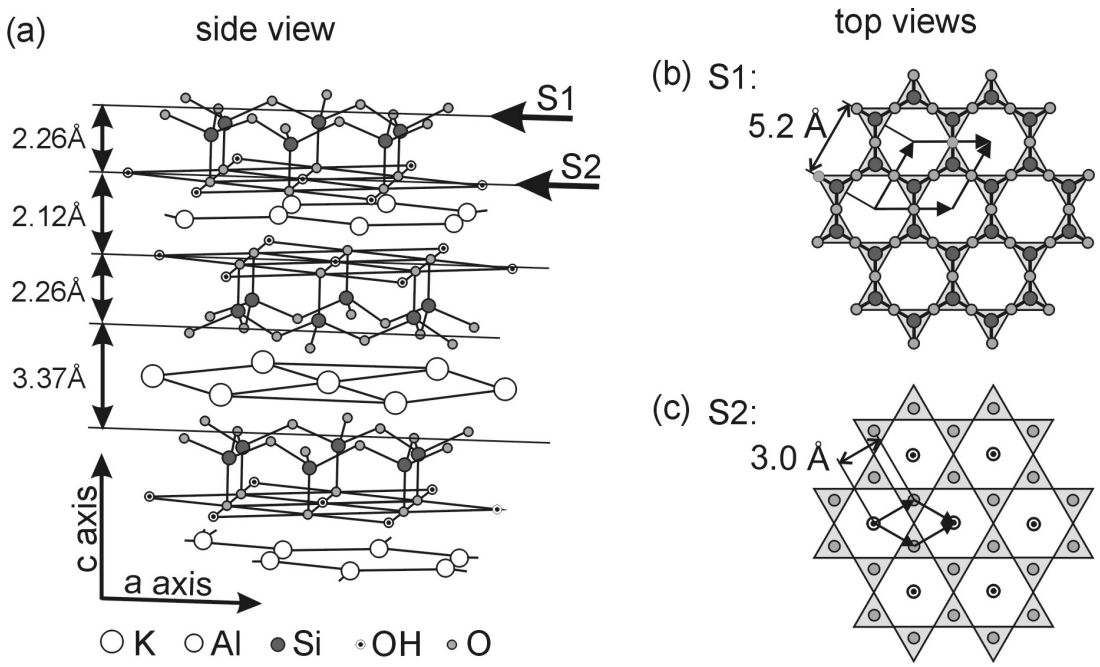

Figure 3.1: (a) Crystallographic structure of muscovite mica from [53]. (b) Top view of the layer labelled "S1", showing the array of hexagonal rings formed by the bases of SiO_4 tetrahedra. This is the periodicity typically imaged by AFM. (c) Top view of the layer labelled "S2" below the SiO_3 bilayer. The sites are occupied by O and OH-groups with a periodicity of 3.0 Å, and form an angle of 30° relative to the former lattice direction. The K^+ ions on top of the S1 layer are not shown.

3.2 A New Cleavage Plane

The following experiments were mainly performed (on the AFM described in detail previously) under ambient conditions, i.e. at room temperature (21°C) and at a relative humidity (RH) of approximately 55 % (unless otherwise noted). To achieve zero humidity a similar setup but with vacuum capability was employed. Four silicon cantilevers[1], two with a nominal force constant of 2.1 N/m and a nominal tip radius of 50 nm and two with a force constant of 0.4 N/m and measured tip radii of 30 - 50 nm were used. Tip radii were measured by imaging the tip with a silicon grating with sharp ridges (see Figure 2.4b).

In previous experiments, scanning at sufficiently high load produced damage in the form of 10 Å deep holes [75], due to the removal of entire mica sheets. While characterizing this wear process in detail, we noticed that 2 Å and 12 Å deep holes could also be produced after a certain number of scans over the same area. This is shown in the example in Figure 3.2a. From Figure 3.1 it is clear that the 2 Å holes correspond to the removal of first layer SiO_3 tetrahedral units, by the rupture of Si-O bonds. This was never before reported for AFM measurements, although Brusdeylins *et. al.* found steps with a height of 2.5 Å by helium scattering experiments on mica cleaved in UHV [76].

To ascertain the structure of the new layer, lattice-resolved lateral force images were acquired at low loads (well below the damage threshold) inside the 2 Å hole. The result, shown in Figure 3.2, indicates that the periodicity of the newly exposed layer is 3.0 Å and that it is rotated approximately 30° relative to the original mica surface. This is what is expected from the "S2" plane (see Figure 3.1), which consists of O and OH species. Furthermore the surface potential

[1]Ultralevers, Park Scientific Instruments, now ThermoMicroscopes, Sunnyvale, CA, USA. www.thermomicro.com

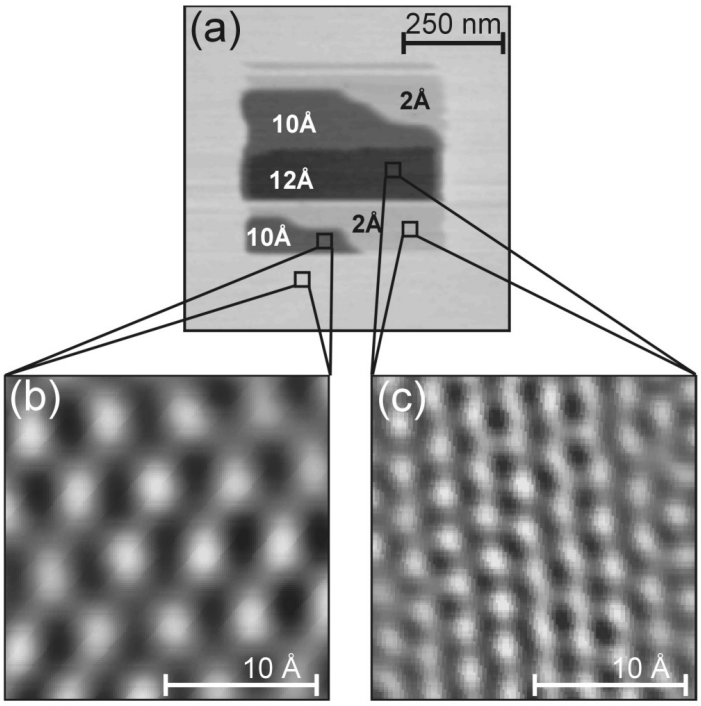

Figure 3.2: AFM images of a hole scratched into muscovite mica with an AFM tip. For these images a silicon cantilever with a nominal force constant of 2.1 N/m and a nominal tip radius of 50 nm was used. The hole was created after 8 consecutive scans with a load of 230 nN, over an area of 500 × 500 nm^2 at a scan speed of 60 ms/line. (a) The hole obtained with these parameters shows 2 Å, 10 Å and 12 Å deep regions (different shades of gray). Marked with a square are regions where the atomic lattice resolution images, shown Fourier filtered in (b) and (c), were obtained. The periodicities in these images are 5.2 Å (b) and 3.0 Å (c). In addition the lattice is rotated by $\sim 30°$. The image size is 0.75 × 0.75 μm^2.

difference between the original surface and the "S2" layer was measured as described in section 2.3. The surface potential of the latter was found to be 20 mV lower than that of the "S1" surface. As can be seen in Figure 3.3c the surface potential of the 10 Å deep hole, exposing again an "S1" type surface, is the same as the undamaged surface. These results indicate that the formation of wear scars is due to Si-O bond breaking processes in the top layer and not due to the emergence of dislocations from deeper inside the mica, as expected from classical plasticity theory.

Although the energy to break a Si-O bond is quite high (approximately 4 - 7 eV, depending on the surrounding atoms), the presence of water provides an energetically lower reaction pathway since the dangling bonds can be capped off with OH and H groups. The activation barrier for breaking a Si-O bond is lowered substantially to about 1 eV, thanks to the energy gain from simultaneously formed SiOH, which is a reasonable value regarding the energy balance for these reactions. The role of water in lowering the barrier for bond breaking is supported by measurements made in vacuum (pressure below 10^{-2} Torr). Under these dry conditions, high loads of 400 nN and 20 to 30 consecutive scans over an area of 400 × 400 nm^2 (at 25.6 seconds per image) failed to produce any visible damage. The humidity had to be increased (by leaking water vapor into the chamber) above 50 % (RH)[2] to allow the generation of visible

[2]The relative humidity (RH) was determined by measuring the partial pressure of water inside the chamber with a capacitance gauge.

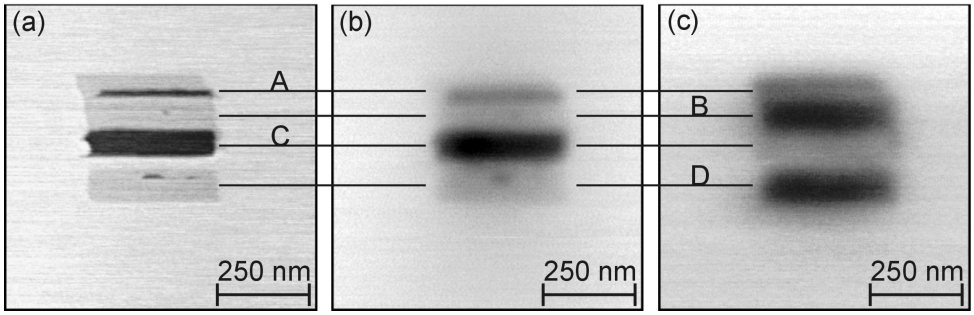

Figure 3.3: (a) contact mode image of a 400 × 400 nm^2 hole with 2 Å and 10 Å deep regions scratched into mica with an AFM tip. (b) and (c) non-contact scanning polarization force images of the same area. While (b) shows the topography channel, similar to (a), only with lower resolution, (c) represents surface potential changes. The lines marked A to D correlate corresponding regions on the different images. Apparently the 2 Å deep regions have a lower surface potential (by 20 mV), while the 10 Å deep ones have the same surface potential as the undamaged region around the hole. Image size is 0.85 × 0.85 μm^2.

damage after 1 to 5 scans, again at 400 nN total load. When decreasing the humidity again, hole creation ceased below 50 %. This behavior could be reproduced by increasing and decreasing the humidity several times across this threshold humidity with the same tip on different areas on the sample. A relative humidity of 50 % corresponds to an equilibrium water adsorption on mica of roughly one monolayer [77], while complete saturation occurs only for 80 % to 90 % RH.

3.3 Measurements of Number of Scans vs. Load

Wear scars can be produced by repeatedly scanning over the same region at a fixed load, as we shall see. It is, however, independent of humidity above 50 %. At moderate loads (80 nN for a tip of $\sim$ 30 nm radius) the 2 Å hole will form first, followed at higher loads (or more scans) by the formation of the deeper 10 Å hole. The number of scans necessary to create visible 2 Å deep wear holes was measured as a function of applied load, while keeping the scanning area and speed constant. This number was found to increase rapidly with decreasing load, as shown in Figures 3.4a and b. The shape of these cumulative curves is very reproducible.
A simple model provides the basic explanation of the physical phenomena that are occurring. Point defects are created as a result of the lowering of the activation energy for bond breaking by the applied stress. A similar model was used by Dickinson *et. al.* to explain tip induced dissolution of calcite in $CaCO_3$ solution [78]. The number of defects created in the absence of stress is extremely small. In the tip sample contact area, it is given by:

$$N_{def}(L) = t_{res} n_0 A(L) \nu e^{-\frac{\epsilon_0 - \delta\epsilon(L)}{kT}}, \tag{3.1}$$

where t_{res} is the residence time of the tip, which is given by the ratio of contact area and image area (400 x 400 nm, in this case) multiplied by the time required for an image (25.6 s, in this case): $t_{res} = \frac{A(L)}{A_{Image}} \cdot t_{image}$, n_0 ($\sim 10^{19}\ m^{-2}$) the surface density of atoms, and *A(L)* the contact area as a function of total load L, which will be estimated using Hertzian contact mechanics. ν is the attempt frequency (on the order of $\sim 10^{13}\ s^{-1}$) to overcome the energy barrier ϵ_0 to break a Si-O bond. $\delta\epsilon(L)$ is the decrease in activation energy due to the applied stress, which can be estimated by multiplying the force acting on an atom by the resulting bond stretch. The average force per atom is given by the pressure *P(L)* in the contact divided by n_0. The relative deformation (bond stretch) $\frac{\Delta l}{l}$ should be on the same order as the Hertzian indentation depth

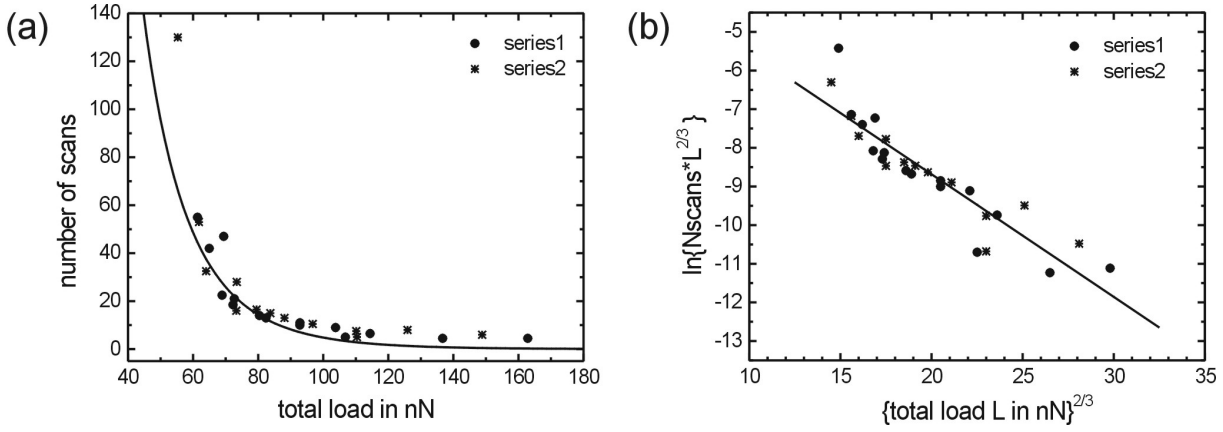

Figure 3.4: (a) Number of consecutive scans necessary to cause visible damage to the mica surface, i.e. 2 Å deep holes. Data from two series of experiments, measured with the same tip (force constant 0.4 N/m) in two consecutive days, are shown. (b) The same data in a semilog plot (see axis labels). The solid lines are fits according to Equation 3.2.

h, divided by the characteristic length of the affected area, which is on the order of the contact radius $r(L)$: $\frac{\Delta l}{l} \approx \frac{h}{r(L)}$, with $h \approx \frac{r^2(L)}{2R}$ for a tip radius $R \gg h$. Thus $\delta\epsilon(L) \propto L^{2/3}$. Note also that the contact area $A(L) \propto L^{2/3}$.

Wear damage will occur when the defect density ($\frac{N_{def}}{n_0 A(L)}$) reaches a critical value η_{crit} and gives rise to nucleation of a hole. Thus the number of scans (N_{scans}) multiplied by the defect density has to equal this critical value. We thus arrive at the following cumulative curve:

$$N_{scans} = A_0 L^{-2/3} e^{-B_0 L^{2/3}}, \tag{3.2}$$

with constants A_0 and B_0. This curve fits the experimental data quite well, as shown in Figure 3.4(a), and in the semi-log plot of Figure 3.4(b). The semi-logarithmic representation $ln(N_{scans} L^{2/3}) = lnA_0 - B_0 L^{2/3}$ clearly shows the validity of Equation 3.2. A linear fit (solid line) yields the slope B_0 and the ordinate lnA_0. A small offset of the data is necessary, however. As can be seen in Figure 3.4(a), even at high loads, it takes a minimum of 4 scans to visibly detect the wear threshold. This is related to the noise level in the friction force measurement. While A_0 contains the critical defect density η_{crit}, B_0 contains only known (at least approximately) material constants:

$$B_0 = \frac{l\ K^{1/3}}{2\pi k T n_0 R^{4/3}}, \tag{3.3}$$

where l is the Si-O bond length (1.5 Å), $K = \frac{4}{3}(\frac{1-\nu_1^2}{E_1} + \frac{1-\nu_2^2}{E_2})^{-1}$ is the combined elastic modulus with values for poisson ratio ν and Young modulus E for a Si-tip ($\nu_1 = 0.3$, $E_1 = 155$ GPa) and for mica ($\nu_2 = 0.1$, $E_2 = 56.5$ GPa), k is the Boltzman factor, T the temperature and R the tip radius (35 nm used for calculation). $n_0 = 8.54 \cdot 10^{18}\ m^{-2}$, based on the 2 Si-O bonds along the c-axis of the 2 SiO_4 tetrahedra per unit area. The value of B_0 obtained from the fit, $\sim (3.0 \pm 0.5) \cdot 10^5\, N^{-2/3}$, is 13 times larger than the estimated value of $2.3 \cdot 10^4\, N^{-2/3}$. A_0 obtained from the fit ($\sim 0.1\, N^{2/3}$), together with a bond breaking energy of ~ 1 eV , gives a critical defect density on the order of a few percentage of the bonds. This corresponds to a number of defects in the contact area on the order of 1, which indicates, that once produced, a hole grows rapidly to cover the entire surface.

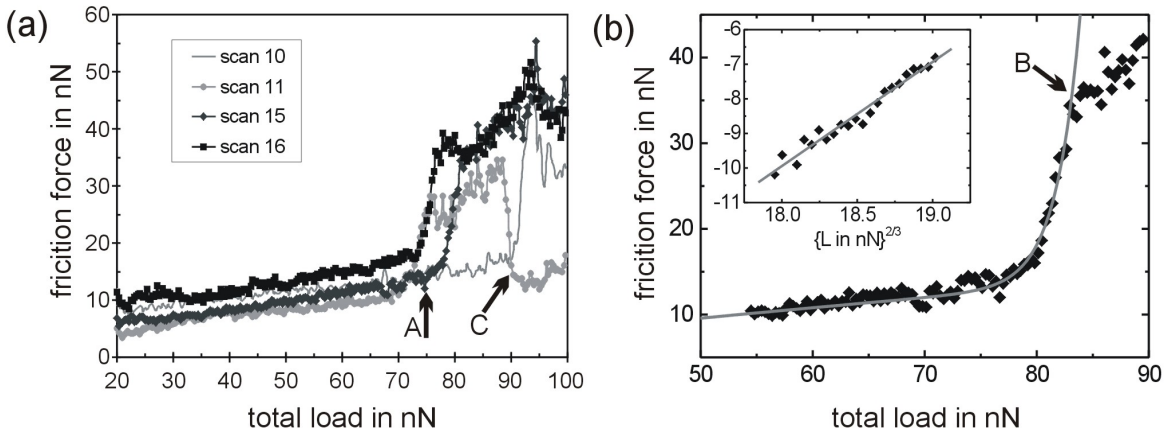

Figure 3.5: (a) Friction vs. load curves obtained during the creation of 2 Å and 10 Å deep holes. Rapid increase in friction is observed above 75 nN load, corresponding to a large increase in the the production of defects. When the density of defects reaches a critical value, the friction levels off and a wear scar detectable by AFM is produced. (b) The fit of Equation 3.4 to one of the curves (scan 15). The inset shows the region, where the friction increases rapidly, in a semilog representation (see Equation 3.5): $ln[F(L) - c(L - L_0)^{2/3}]/L^{2/3}$ is plotted vs. $L^{2/3}$ to allow for a simple linear fit of the coefficient B_0 (slope).

3.4 Friction Measurements During Hole Creation

In addition to measuring the number of scans required to cause damage to the mica at a certain load, friction was measured as a function of load, scanning only in one direction perpendicular to the cantilever over 150 nm. Since the cantilever is mounted at an angle of $\sim 15°$ from the sample surface, the tip moves by ~ 60 nm, as the load is increased (line-by-line) to its maximum value. For a description of the friction vs. load data analysis see section 2.2. After several cycles of ramping the load, wear scars start to form, preceded by a significant increase in friction. This is shown in Figure 3.5(a) above 75 nN (marked "A"). Eventually, after reaching a high value (marked "B" in Figure 3.5(b)), the friction drops back to a low value (marked "C" in Figure 3.5(a)). Lattice resolved images (at a total load of 3 to 5 nN) were obtained after the point where the friction started to increase rapidly (about 75 nN under our conditions, marked "A" in Figure 3.5) and up to and beyond point "B". Using the Hertzian model of contact between elastic spheres, we estimate the contact diameter to be ≤ 3 nm for our tip radius under these conditions. The periodicity of these images was 5.2 Å, i.e., unchanged relative to the original images. No defects could be observed in the images either, which indicates that the size of the defects produced is smaller than the contact diameter. This suggests point defects, such as atom vacancies or clusters of vacancies of a few atoms and interstitials. Only after the friction returns to its initial low value (marked "C"), is the new 3 Å periodicity revealed. This drop in friction indicates that, once the defects are produced, wear and removal of the top Si-O layer occurs much more easily.

The same model applied in the previous section to describe the dependence of the number of scans necessary to cause damage on the applied load can be extended to explain the rapid increase in the friction force curves. Figure 3.5(a) shows several curves where 2 Å (scans 10 and 11) and 10 Å (scans 15 and 16) deep holes were created. According to the model, the friction

curves should follow:

$$F(L) = c(L - L_0)^{2/3} + \gamma L^{2/3} e^{B_0 L^{2/3}}, \tag{3.4}$$

where the first term includes the wearless friction part, which is proportional to the contact area (e.g., phonons), using a simple shifted Hertz model for the contact area. The second term is the contribution of the defect production model. The additional friction force is assumed to be proportional to the number of defects $[N_{def}(L)]$ produced in the contact area. For these experiments, $N_{def}(L)$ is calculated using t_{res}, which is given by $t_{res} = \frac{\pi r(L)}{v_{line}}$, where v_{line} is the scan speed (0.04 s/150 nm) and $\delta A(L) = 2r(L)\delta x$ is the area swept by the tip. The validity of Equation 3.4 can be tested using a semilogarithmic representation of the experimental data of the form

$$ln\left\{\frac{F(L) - c(L - L_0)^{2/3}}{L^{2/3}}\right\} = ln\gamma + B_0 L^{2/3}. \tag{3.5}$$

As can be seen from the fit to one of the scans [Figure 3.5(b) and inset], the agreement is excellent. In this case, we get a value of $3.0 \cdot 10^6\, N^{-2/3}$ for B_0, which is higher by a factor of 130 than the calculated value, and within a factor of 10 of the value measured before. This is still quite reasonable, considering the simplicity of the assumptions.

3.5 Summary

In conclusion, we have shown that wear results from the production of surface defects, most likely point-type defects, at high load and that this constitutes an important mechanism of energy dissipation in friction, even when the defects are not yet visible in AFM contact images. In our model, the activation energy for bond breaking is lowered by the applied stress, which greatly enhances the rate of defect production.

Chapter 4

Alkyl-Silane Islands on Mica

This section presents a series of AFM experiments on alkylsilane monolayer islands, which exhibit a striking step-wise change in their structure and friction properties at specific loads. These observations can be interpreted as pressure-induced changes in the structural arrangement of molecules in the film. This demonstrates a connection between energy dissipation in friction and specific molecular scale events occurring at organic interfaces [79, 80, 81].

4.1 Sample Preparation

To measure the height and friction properties of a lubricant layer simultaneously the samples consist of (monolayer) islands instead of a complete monolayer. Islands can be easily produced with the self-assembly method (see section 1.4) by reducing solution concentration and immersion time, relative to those for monolayers, until the desired island size and density is obtained. With the Langmuir-Blodgett technique (see section 1.4) preparation of island samples is possible, but the effort per sample is much bigger, since island size and distribution depend on the transfer pressure and the pH of the subphase [82]. Furthermore it is more difficult to obtain reasonably large, clean areas of mica between the islands.
For an accurate height measurement it is vital to have an atomically flat substrate. One of the easiest to prepare is muscovite mica (see chapter 3). It can be easily cleaved either with adhesive tape or a razor blade, to expose a fresh, over hundreds of micrometers atomically flat surface.
From the variety of organic molecules, which were found to self-assemble on mica, alkylsilanes are one of the most common types. They adhere strongly to mica, i.e. they are not easily removed by the scanning AFM tip, are rather easy to prepare and commercially available.
With respect to the complex reaction of long-chain alkylsilanes, an already successfully used recipe [83] was followed to obtain the samples for this study:
The basic compounds were simple triethoxysilanes[1] of various chain lengths: $CH_3-(CH_2)_{\text{n-1}}-Si(-O-C_2H_5)_3$, with n = 18, 16 and 12. This species was chosen over the more common trichlorosilane, because of the lower reactivity with the ambient humidity. To achieve adsorption on mica the molecules had to be modified to alkylsilanols by a hydrolysis reaction:

$$\begin{aligned} &CH_3-(CH_2)_{\text{n-1}}-Si(-O-C_2H_5)_3 \;+\; HCl \;+\; 3\,H_2O \\ &\longrightarrow CH_3-(CH_2)_{\text{n-1}}-Si(-O-H)_3 \;+\; HCl \;+\; 3\,CH_3-CH_2-OH \end{aligned} \tag{4.1}$$

where the HCl functions only as a catalyst. It protonates the water, the H^+ replaces $CH_3-CH_2^+$, which is saturated by OH^-. This is achieved by adding 0.2 g of the triethoxysilane and 0.2 g of 1M HCl solution in water to 25 ml of tetrahydrofurane[2] (THF), which has to be stirred for

[1] United Chemical Technologies, Inc., Bristol, PA, USA, used as received.
[2] 99+% (BHT stabilized 250ppm), Sigma-Aldrich, Milwaukee, WI, USA, www.sigma-aldrich.com

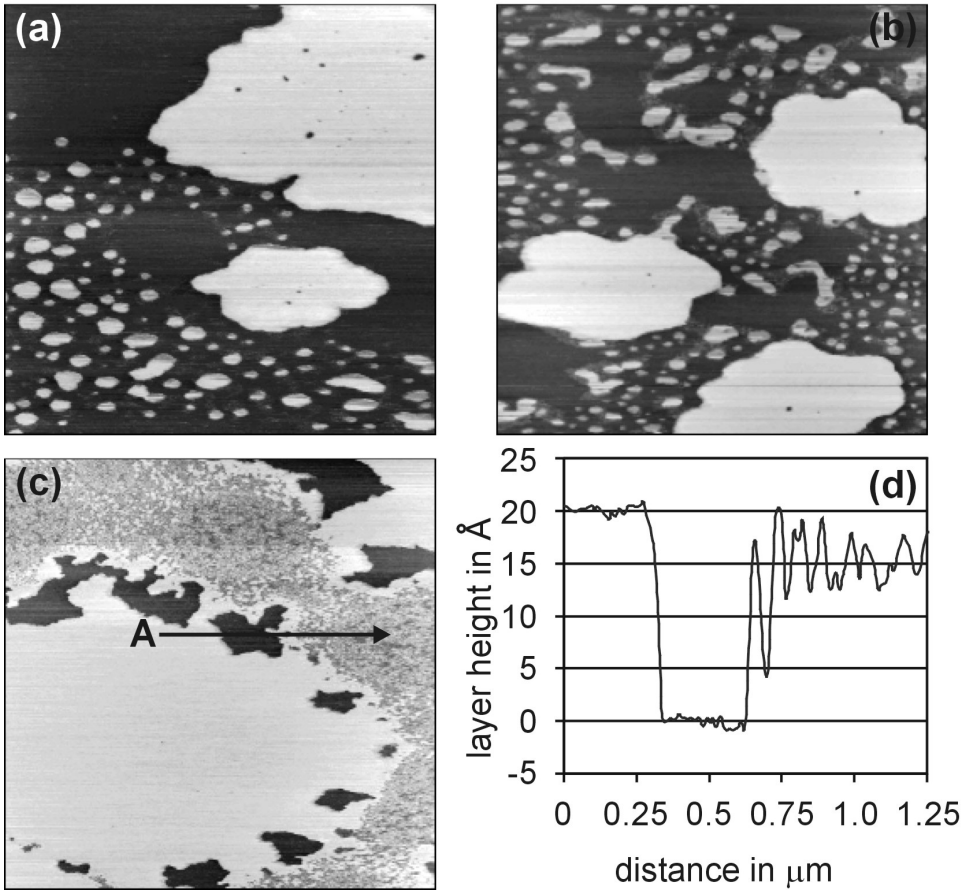

Figure 4.1: Typical topography AFM images obtained on (a) C18, (b) C16 and (c) C12 silane islands. Lighter colors correspond to higher regions. In (d) a cross-section along a scan-line is shown, as marked in (c). Image sizes are (a) 2.50 × 2.50 μm^2, (b) 3.30 × 3.30 μm^2 and (c) 2.55 × 2.55 μm^2.

at least 72 h before use. Samples should be prepared within 1-3 days thereafter. However, island preparation was still possible 2 weeks after the initial stirring phase was over. Preparation of *monolayers* could only be achieved within the first few days after the hydrolysis was complete. Afterwards inhomogeneities appeared, e.g. monolayers had islands of approximately 0.5 micrometers diameter protruding about 0.5 Å.

The silanol solution was further diluted in cyclohexane[3], approx. $100 - 250\mu l$ solution into 25 ml solvent, yielding a final concentration of $80 - 200\mu$M. A piece of freshly cleaved mica was immediately immersed for a few seconds, rinsed for 10 - 20 seconds in pure cyclohexane and afterwards dried under a stream of dry nitrogen. The exact concentration and immersion times were varied to change the size, number and distribution of islands on the surface. Higher concentrations yield bigger islands, longer immersion times result in a higher island density. At least three samples can be prepared successively from these 20 ml of solution, without any degradation in sample quality.

AFM images acquired at negative external load, in other words, slightly pulling the lever away from the surface in the adhesive regime, revealed the presence of numerous islands of the self-assembled silanols. Under these conditions, the height of the islands was found to be 27 Å for the C18, 25 Å for the C16 and 20 Å for the C12, with an absolute uncertainty of ± 1 Å. The

[3] 99.9+% (HPLC grade), Sigma-Aldrich

uncertainty for changes in height, however, is about ± 0.5 Å. These heights are slightly larger than expected from the length of the corresponding molecules standing upright [84]. Lateral island dimensions of a few hundred nanometers up to a few micrometers were typical. Figure 4.1 shows typical examples of AFM images of silane islands obtained with this method. Apparently there is a significant difference in the morphology of the islands of C16 and C18 compared to the island of C12 silane. The latter has a fractal, dendritic structure and is surrounded by a dense sea of tiny islands with a well defined height, which is smaller than the actual island height (see Figure 4.1(d)). Thus it seems that the adsorption mechanism also depends on the chain length, which is supported by the observation that it was not possible to obtain islands for C8 silane or shorter chains. Based on the results of Carraro *et. al.* [41] about the influence of temperature on the adsorption process, one can speculate, that by lowering the temperature it is possible to obtain islands also for short chains by self-assembly. But the imaging would have to be performed at low temperatures too, to avoid the risk of "melting" the islands. Islands could be observed on these samples even after months of storage under ambient conditions. However, we have strong reasons to believe that at least for the first few days the molecules are *not* covalently bonded to the substrate, but rather loosely attached via hydrogen bonds [44, 85, 86]. Maybe there is even a monolayer of water enclosed between the silane molecules and the mica substrate, causing the increased island height, similar to what was observed by Parikh *et. al.* [46]: The authors found "microcrystallites" of periodic layers, each consisting of a monomolecular layer of intercalated water enclosed on each side by a crystalline monolayer of alkyl chains. Furthermore it can be observed, that the big islands (diameter of 1 - 2 μm) act like "black holes" (to borrow the term from astrophysics), i.e. small islands migrate or diffuse towards the big ones within the first few days after preparation, leaving a stretch of clean mica (width $\sim$ 0.5 μm) around large islands, where initially small islands could be found. A similar enlargement of islands over the course of days was observed for hexadecylthiol on gold [87]. The most convincing argument to show that the silane molecules can not be rigidly bound to the substrate, is the observation of tilts, as described in section 4.2 and 4.3, which would be impossible if the bases of the molecules were fixed.

4.2 Measurements of Height and Friction vs. Load

All measurements were performed with a home-built AFM, which is described in detail in section 2.1, under ambient conditions, i.e. at room temperature of 21° C and at a relative humidity of 35 % to 45 %. The height and friction behavior of the islands as a function of the load applied by silicon-nitride tips were measured by simultaneously acquiring topographic and friction images of an island and the surrounding substrate. Friction values were obtained according to the "image by image" procedure, described in section 2.2. The height of an island was extracted from several cross-sections of a topographic image. Height and friction are given as a function of total applied load, i.e. including the pull-off or adhesive force, which was about 30 nN for the C12 and C16 islands measured with the same tip. On the C18 islands this force was approximately 45 nN, using a different tip with similar radius.

The results of measurements of two C12 islands are shown in Figure 4.2. Note, the data of Figure 4.2(b) is obtained from the island of Figure As can be seen, there is a remarkable stepwise decrease in the height of the islands. Plateaus extending over a certain load range can be clearly distinguished from transition regions separating them. For the first island (Figure 4.2), the height decreases to 17.5 Å in a first step at about 15 nN. There is a second decrease down to a height of 14.5 Å at about 65 nN and a third one around 115 nN. For the second island (Figure 4.2(b)), with approximately the same size, the first step down to 17.0 Å occurs also at a load of about 15 nN, the second at 60 nN with a decrease down to a height of 12.0 Å, and the final decrease around 105 nN. For C16 and C18 islands similar behavior was observed but

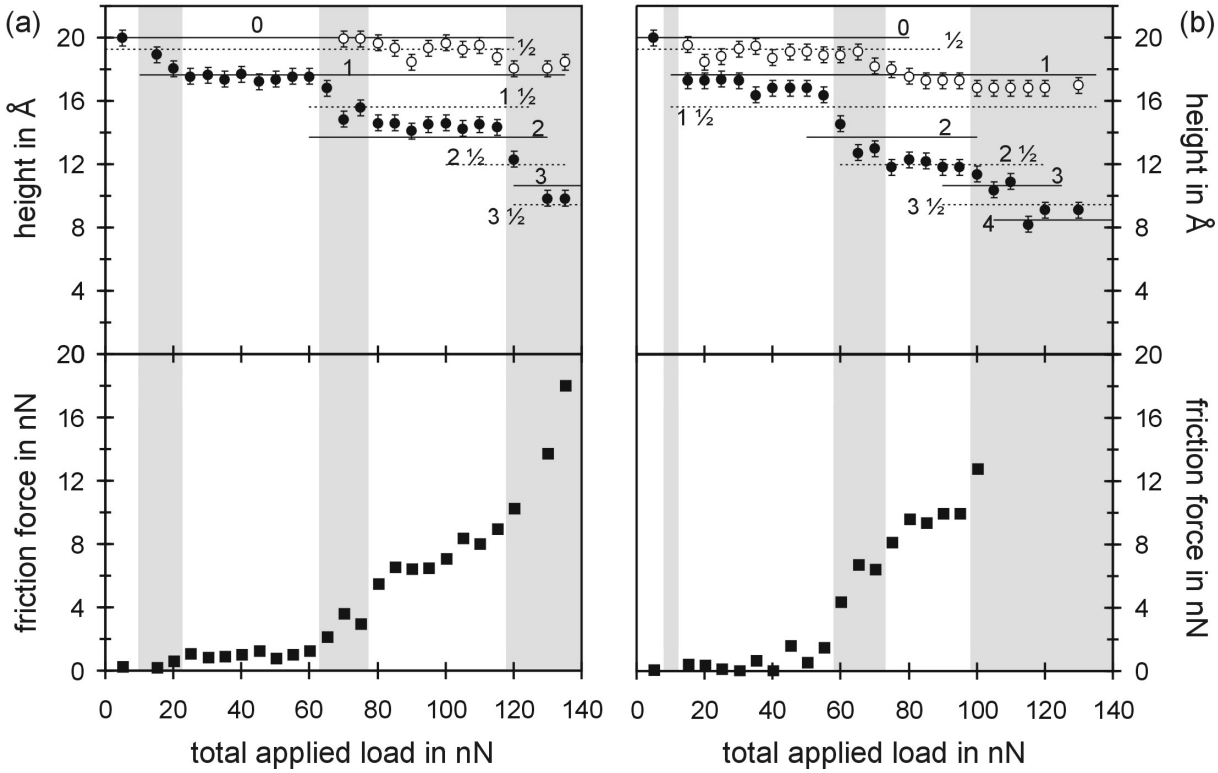

Figure 4.2: (top) Height of C12 alkylsilane islands (measured at the island's center) vs. load (filled circles). The height decreases in discrete amounts at critical loads. Adhesive forces, with a maximum (pull-off) value of about 30 nN, are already added to the external, applied load. Open circles correspond to the height of the film after decreasing the load to the lowest practical value for imaging (5 nN). For (a) the height of the island recovers completely up to about 80 nN (points below 65 nN are not shown for simplicity). For (b) the recovery is not complete already at the loads of the first plateau. Above 75 nN the height of the island recovers only to the height of the first plateau of 17.0 Å. Solid and dashed lines correspond to heights expected from the tilting model presented in section 4.3. (bottom) Simultaneously measured friction force. A steplike behavior correlated with the height decreases is observed. The island of (b) had already disintegrated to such a degree above 105 nN that friction data was unreliable. Transition regions are shaded.

with plateaus at different heights. Although there is some variability in the threshold load from island to island and from tip to tip, the heights observed for such steps were always reproducible. In some cases, a plateau is skipped (compare the plateaus of Figure 4.2 (a) and (b)) and the height decreases to the next one. At very high loads, the height decreases continuously to a final residual height of about 5 Å. The measured heights for the different islands are summarized in Table 4.1 and 4.2 in section 4.3.

On islands with diameters smaller than 0.5 μm, the steps occurred at significantly lower loads, while islands larger than 2 μm could not be compressed (except near the rim). Figure 4.3 compares the height vs. load data obtained on a small (diameter $\sim$ 250 nm) and a big (diameter $\sim$ 1.5 μm). We attribute this variability to differences in the compactness of the islands which is probably the result of local differences in the assembly process. Note, this stepwise decrease of island height could only be observed with AFM tips with a radius equal or smaller than 50 nm, thus the load range of 5 - 150 nN corresponds to a pressure in the contact are between 0.23

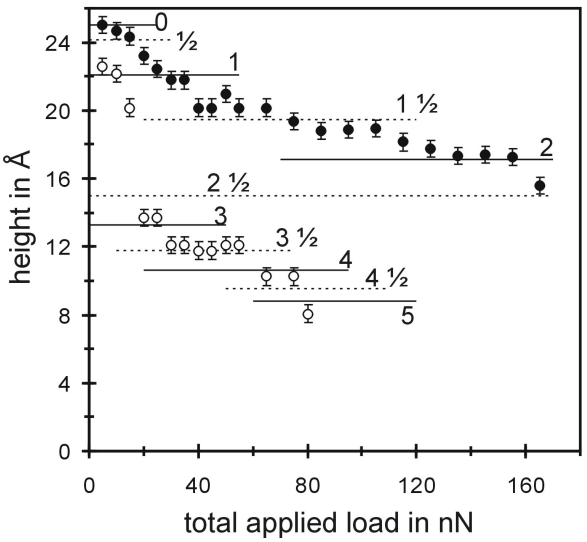

Figure 4.3: Two examples of half-integer steps in height vs. load curves for a small island ($\sim$ 250 nm diameter) and a big island ($\sim$ 1.5 μm diameter) of C16 alkylsilane, represented by open and filled circles respectively. Solid and dashed lines represent calculated integer and half-integer steps (see section 4.3), respectively.

GPa and 0.72 GPa.[4]

The friction behavior is equally striking. A clear increase in friction is observed with each change in height. This indicates that new energy dissipation channels become available at specific loads. Looking back at friction vs. load data obtained by Xiao *et. al.* [14] on a C8 silane monolayer, such a stepwise increase in friction was already present, but without the correlation to decreasing height, the appropriate interpretation was not possible.

Immediately after each measurement of height and friction at a given load, the sample was imaged again at the lowest possible load to determine whether the changes were permanent or if the molecular film recovered its initial height. Interestingly, although the changes in friction were always reversible, there was a threshold load after which the original height was not recovered. For the C12 example shown in Figure 4.2(a), the height recovery was complete up to the third step, for the one in Figure 4.2(b) up to the second step. Irreversible height changes also occurred in a discrete series of plateaus directly correlated with the reversible changes (see Figure 4.2(b)) up to high loads, at which the also the irreversible height loss increased continuously with load. When the load reached values at which the island height was not recovered, we observed damage in the form of island fragments, debris displaced away from the borders, and holes inside the island.

The loss of height and the corresponding increase in friction observed in the experiments described above were not uniform over an entire island but occurred first at the periphery, giving rise to a "sombrero" shaped island when the load was above the first or second step. The "brim" of the sombrero became wider as the load increased until the island became flat again, as shown in Figure 4.4 for a C12 island. Since an AFM image represents only the situation directly underneath the tip, one should be careful not to think that the entire island is compressed. Only the molecules underneath the tip, i.e. in the contact area of about 5nm radius or less in these

[4]The pressure $P = \frac{L}{A}$ is calculated using Hertzian contact mechanics to obtain the contact area $A = \pi \left(\frac{RL}{K}\right)^{2/3}$, with total applied load L, tip radius R and combined elastic modulus $K = \frac{3}{4}\left[\frac{1-\nu_1^2}{E_1} + \frac{1-\nu_2^2}{E_2}\right]$ for alkyl chains (Young modulus E_1=9.3 GPa [88], poisson ratio ν_1=0.4) and silicon-nitride (E_2=140 GPa, ν_2=0.3).

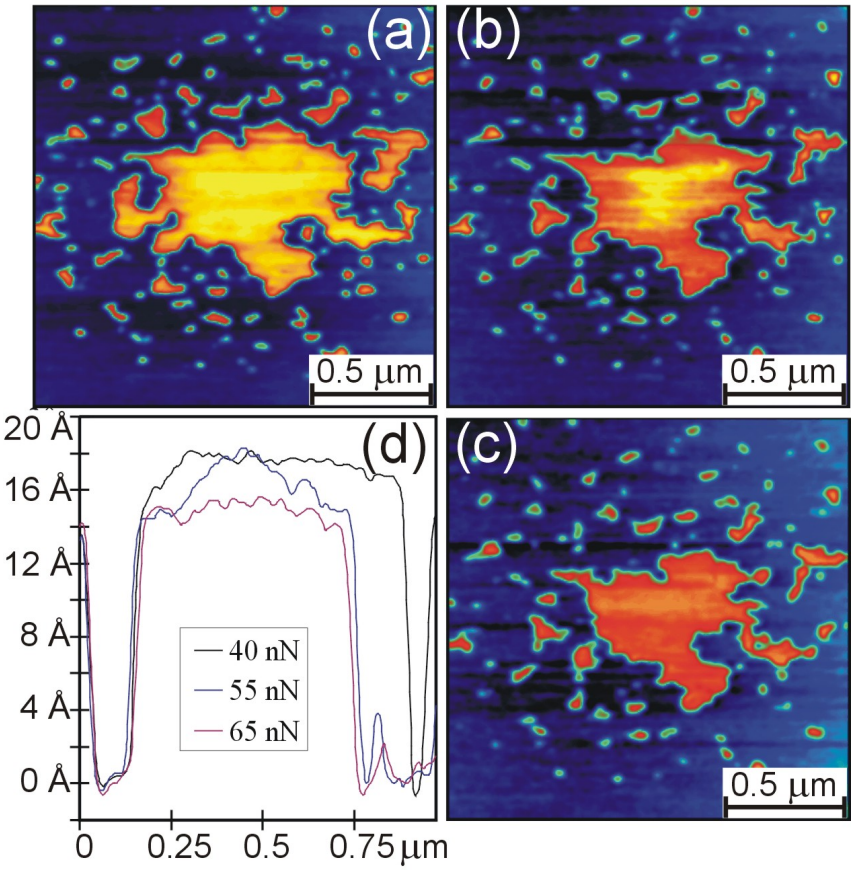

Figure 4.4: Series of topographic images of a C12 alkylsilane island at (a) 40 nN, (b) 55 nN and (c) 65 nN total applied load. Lighter areas correspond to higher regions. In this load range, the height of the island decreases from 17 Å to 14.5 Å, corresponding to plateaus 1 and 2 in Figure 4.2(a). The image in (b) shows clearly that the compression is not uniform: The rim of the island is already lower while the center can still sustain the pressure. (d) Height profiles taken horizontally through the middle of the island. In addition to the height decrease starting at the edges, material is also displaced away from the island as the load increases. Note: In this island (the one of Figure 4.2(b)), 65 nN corresponds to the beginning of a transition region.

experiments, collapse to a given discrete height. After tilting, the molecules assume an upright configuration when the tip has passed (for moderate loads).

4.3 Tilting Model

4.3.1 First Approximation: Integer Steps

The phenomena described before can be explained with a simple molecular structure model. At low loads the long alkyl chains form islands of closely packed, upright molecules. This configuration optimizes the van der Waals attractive energy, which is the driving force for the self-assembly process. Longer chains gain the most from dense packing and therefore form the sturdiest films. Other arrangements of alkyl chains having the same density are possible [38, 89], e.g. by tilting the molecules while keeping their separation constant (about 4.7 Å, the diameter of the $-(CH_2)_n-$ chains). The tilted configuration has a lower total cohesive energy; i.e., it is

less stable because of the smaller film thickness. Optimal packing is achieved for specific angles, dictated by the zigzag skeletal structure of the carbon atoms, when alternate methylene groups of one chain nest into the corresponding depressions in the neighboring chains, as shown in the schematic drawing of Figure 4.5 [90]. This interlocking of molecules is supposed to be the reason for the existence of the first few reversible steps in height observed in these experiments.

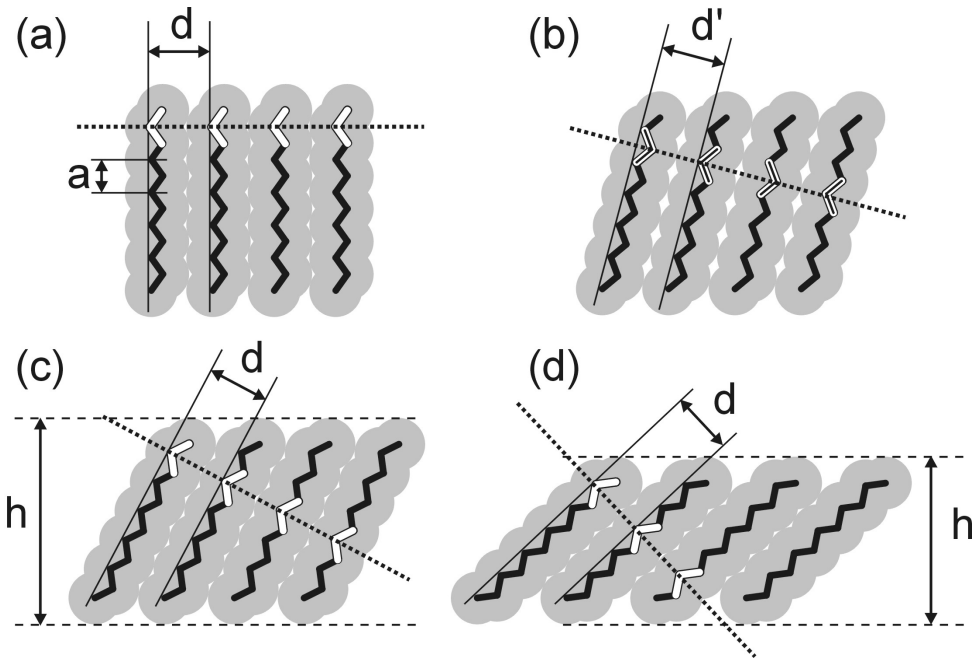

Figure 4.5: Schematic model of all-trans alkyl chains that illustrates tilt configurations which fulfill the condition of maximum packing density (constant separation d between chains). Only certain angles are allowed due to the zigzag arrangement of the carbon atoms. (a) Uncompressed, upright configuration. (b) Opposed zigzag, causing an increased separation (*d'*) of the molecules. This unfavorable energy state has to be overcome to reach the first (c) and second (d) tilted configuration. The height of the islands with tilted molecules can be calculated with simple geometry. The result is $h = L[1 + (\frac{na}{d})^2]^{-\frac{1}{2}}$, where L is the total length of the molecule in all-trans configuration, a (2.5 Å) is the distance between alternate C in the molecule, d (4.7 Å) is the separation of the molecules and n is the step number. The van der Waals diameter of a CH_2-group was taken to be 4 Å and the angle between adjacent C-C bonds to be 109.5°.

The expected height changes from such a model can be calculated from the known 1.25 Å C-C distance (projected along the chain axis), and the 4.7 Å separation d between the molecules: The heights of islands with tilted molecules should only adopt values of

$$h = L \frac{1}{\sqrt{1 + (\frac{na}{d})^2}} \tag{4.2}$$

where L is the total length of the molecule in all-trans configuration, a (2.5 Å) is the distance between alternate C in the molecule, d (4.7 Å) is the separation of the molecules and n is an integer number, which corresponds to the step number.
In Table 4.1 the measured $(\frac{h}{L})$ and calculated $[1 + (\frac{na}{d})^2]^{-\frac{1}{2}}$ relative heights of the monolayer islands are summarized. The solid lines in Figure 4.2 and Figure 4.3 correspond to calculated heights, labelled with the step number n. The agreement is quite good regarding the simplicity of this two-dimensional model. Note, that in section 4.3.2 the *measured* values will be split into more levels when this simple model is refined to accommodate so called half-integer steps. Such

Table 4.1: Measured ($\frac{h}{L}$) and calculated ($[1+(\frac{na}{d})^2]^{-\frac{1}{2}}$) relative heights of the monolayer islands. Measured values are connected with a statistical error of 2 to 3 %. Calculations are based on the assumption that the molecules tilt in discrete steps (n), upon compression with an AFM tip, as described in Figure 4.5. Typical values measured for the uncompressed islands were 20 Å, 25 Å and 27 Å for C12, C16 and C18, respectively.

n	Calculated relative height $\frac{h}{L} = [1 + (\frac{na}{d})^2]^{-\frac{1}{2}}$	Measured relative height of the layer above mica substrate in Å		
		C12	C16	C18
0	1	0.985	1	1
1	0.883	0.860	0.880	0.888
2	0.685	0.725	0.688	0.693
3	0.531	0.590	0.568	0.537
4	0.425	0.450	0.468	—

discrete heights have been observed before for LB-films, i.e. the existence of tilted phases in the compression cycle of long chain molecules at the air-water interface has been known [90] and also measured by AFM [91]. But the measurements presented in this chapter represent the first observation of a (reversible) transition between such tilted configurations induced by applying pressure with an AFM tip.
The need for lateral expansion as the compression and tilting occurs explains why it proceeds from the edges of the island toward the inside and why there is some variability in the experiments, since the presence of defects facilitates molecular tilting.

4.3.2 Refinement to Half-Integer Steps

Although the agreement of the simple 2D-tilting model with the measured heights is quite excellent, there is still room for improvement. As suggested by Würger [80], there are other stable configurations of interlocking zigzag chains, which can be easily adopted by the molecules. Hydrocarbon chains may perform so called screw slips [92], i.e. instead of assuming the energetically unfavorable configuration depicted in Figure 4.5(b) and 4.6(a), every other molecule rotates by

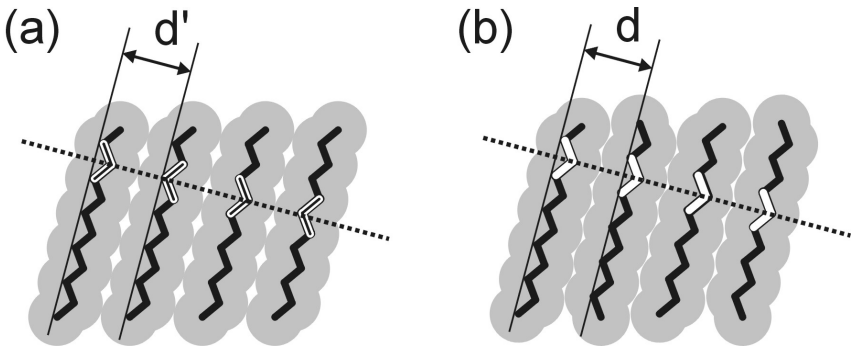

Figure 4.6: Extension of the simple 2D tilt model: Allowing every other molecule in the opposing zigzag configuration (a) to turn around their long axis by π leads to another configuration (b), which fulfills the condition of maximum packing density.

Table 4.2: Measured (h and $\frac{h}{L}$) and calculated ($[1+(\frac{na}{d})^2]^{-\frac{1}{2}}$) (relative) heights of the monolayer islands. Calculations are based on the assumption that the molecules tilt in discrete integer and half-integer steps (n), upon compression with an AFM tip, as described in Figure 4.6. Typical values measured for the uncompressed islands were 20 Å, 25 Å and 27 Å for C12, C16 and C18, respectively.

n	Calculated relative height $\frac{h}{L}=[1+(\frac{na}{d})^2]^{-\frac{1}{2}}$	Calculated, measured and measured relative height of the layer above mica substrate in Å								
		C12			C16			C18		
0	1	20.0	20.0	1	25.0	25.0	1	27.0	27.0	1
$\frac{1}{2}$	0.966	19.32	19.5	0.975	24.15	—	—	26.08	25.0	0.926
1	0.883	17.66	17.4	0.869	22.08	22.0	0.880	23.84	24.0	0.890
$1\frac{1}{2}$	0.782	15.64	—	—	19.55	19.3	0.772	21.11	20.7	0.766
2	0.685	13.70	14.5	0.725	17.13	17.1	0.684	18.50	17.8	0.659
$2\frac{1}{2}$	0.601	12.01	11.8	0.590	15.03	14.3	0.572	16.23	—	—
3	0.531	10.62	—	—	13.28	—	—	14.34	14.5	0.537
$3\frac{1}{2}$	0.475	9.46	9.8	0.490	11.88	11.8	0.472	12.83	—	—
4	0.425	8.50	9.0	0.450	10.63	—	—	11.48	—	—

π around its molecular axis to achieve again a close packed configuration optimizing the cohesive energy, see Figure 4.6(b).
The only modification to Equation 4.2 necessary to accommodate these conformations with a rotation of every other molecule by π is to allow also half-integer values for n:

$$n = 0,\ \frac{1}{2},\ 1,\ 1\frac{1}{2},\ 2,\ 2\frac{1}{2}, \ldots \tag{4.3}$$

These half-integer heights are marked by dashed lines in Figure 4.2 and 4.3. The latter clearly shows that some levels fit much better to half-integer than to integer steps. For small and large tilt angles it is nearly impossible to discern between integer and half-integer steps with AFM, since the differences are smaller than 1 Å. Only for intermediate angles, i.e. for step numbers n between 1 and 3, there is a significant difference between the levels as can be seen in Figure 4.2 and 4.3. In Table 4.2 the calculated (relative) heights are summarized. The previously measured (relative) heights are redistributed with regards to the new possible values. While some measured heights find their perfect match in the calculated ones there are also some ambiguous heights, which can not easily be assigned to an integer or half-integer height.

4.3.3 Three-Dimensional Tilting Model

Although the half-integer steps represent an improvement to the simple two-dimensional model suggested initially, there is still room for further adaption. Barrena *et. al.* [94] present a three-dimensional model (based on integer and half-integer steps), including also next nearest neighbor (NNN) tilts. Using cartesian coordinates, the resulting tilt angle θ is a combination of nearest neighbor (NN) tilts θ_x (for convenience along the x-axis), and NNN tilts θ_y (see Figure 4.7)[5].

[5]Figure 4.7(a) courtesy of Barrena and coworkers

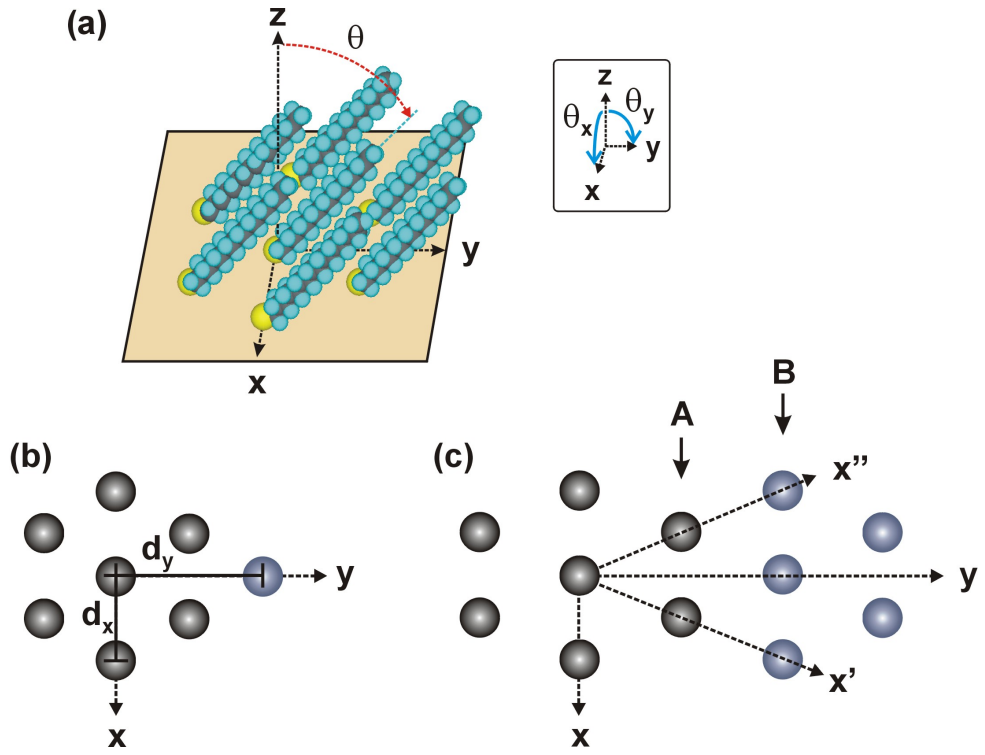

Figure 4.7: Schematic drawing to illustrate the next-nearest neighbor (NNN) tilt in monolayer islands of alkylthiols. The extension of the simple 2D tilt model to three dimensions can be accomplished by an additional angle in the NNN direction. (a) Using cartesian coordinates, the total tilt angle θ can be separated into two components θ_x and θ_y. (b) Topview of untilted upright molecules. The nearest neighbor (NN) distance is d_x, the NNN distance d_y, twice the separation between molecular planes in this direction. (c) Topview of molecules tilted in the direction of the y-axis. The x' and x" direction are equivalent to x due to the symmetry of the system, i.e. seen along x' and x" directions the molecules labelled A are in the NN position, those labelled B in the NNN position. Thus next nearest neighbor tilts can only assume integer tilts (see text), since half-integer tilts would not allow an interlocking of molecules in position A with their neighbors.

The NN tilts along the x-axis will occur for the known condition of

$$\tan\theta_x = \frac{na}{d_x} \quad \text{with} \quad n = 0,\ \frac{1}{2},\ 1,\ 1\frac{1}{2},\ 2,\ 2\frac{1}{2}, ..., \tag{4.4}$$

which is equivalent to Equation 4.2 including half-integer steps.
To calculate the NNN tilt, one has to consider that the condition for the NN tilt still has to be fulfilled for the x' and x" direction (equivalent to x due to the symmetry of the system), i.e. for the molecules in position A [Figure 4.7(c)]. Thus the molecules in the NNN position (marked B) will only assume angles θ_y for which

$$\tan\theta_y = \frac{ma}{d_y} \quad \text{with} \quad m = 0,\ \ 1,\ 2,\ 3, ..., \tag{4.5}$$

with the NNN distance d_y twice the separation between molecular planes in this direction. Note that half-integer values of m would not allow an interlocking of the molecules in position A with their neighbors.
The values for the relative height due to pure NNN tilts can be calculated according to equation 4.2, using d_y instead of d (see Table 4.3).

Table 4.3: Calculated relative heights of a monolayer due to pure next nearest neighbor tilting according to Equation 4.5, with $a = 2.5$ Å and $d_y = \sqrt{3}d_x$, where $d_x = 4.7$ Å.

m	$\frac{h}{L} = [1 + (\frac{ma}{d_y})^2]^{-\frac{1}{2}}$
1	0.956
2	0.852
3	0.735
4	0.631

Table 4.4: Calculated relative heights of a monolayer due to combined nearest and next nearest neighbor tilting: $(\frac{h}{L})_n$ x $(\frac{h}{L})_m$. Values smaller than 0.400 are omitted.

n	$\frac{h}{L}$ for $m = 0$	$\frac{h}{L}$ for $m = 1$	$\frac{h}{L}$ for $m = 2$	$\frac{h}{L}$ for $m = 3$
0	1	0.956	0.852	0.735
$\frac{1}{2}$	0.966	0.923	0.823	0.710
1	0.883	0.844	0.752	0.649
1 $\frac{1}{2}$	0.782	0.748	0.666	0.573
2	0.685	0.655	0.584	0.503
2 $\frac{1}{2}$	0.601	0.575	0.512	0.442
3	0.531	0.508	0.452	-
3 $\frac{1}{2}$	0.475	0.454	0.405	-
4	0.425	0.406	-	-

To obtain the final relative height corresponding to the total tilt angle θ, for a given combination of values n and m the values for the relative heights $(h/L)_n$ (see Table 4.2) and $(h/L)_m$ have to be multiplied with each other. The final relative heights for various values of n and m are given in Table 4.4. Considering all possible combinations for n and m given in Table 4.4 an abundant supply of possible steps is obtained, accounting for any measured height. Regarding only the values for $m = 0$ and $m = 1$ is a more realistic approach. Barrena and co-workers found an excellent agreement with the heights they measured on islands of alkylthiols on gold including NNN tilts of the order $m = 1$.

Looking back at the measurements of height vs. load on two C12 alkylsilane islands presented in Figure 4.2, there are two steps, which are not exactly accounted for neither by integer nor by half-integer steps. Including first order ($m = 1$) NNN tilts, an excellent fit can be obtained also for those, as shown in Figure 4.8. Furthermore, for the height vs. load curve of the big C16 alkylsilane island, shown in Figure 4.3, the data points slightly below the line corresponding to the $1\frac{1}{2}$ step are better matched adding a NNN tilt: $n = 1\frac{1}{2}$ and $m = 1$.

While the simple two dimensional integer tilt model can in general explain the behavior of long alkyl chain molecules under pressure, half-integer and next nearest neighbor tilts have to be added to account exactly for the measured heights of the monolayer islands. Note that already including higher orders of NNN tilts than $m = 1$ decreases the difference between the various calculated heights to below 1 Å, making any assignment to the measured steps rather arbitrary. Thus a technique with higher accuracy has to be found for height vs. load measurements on

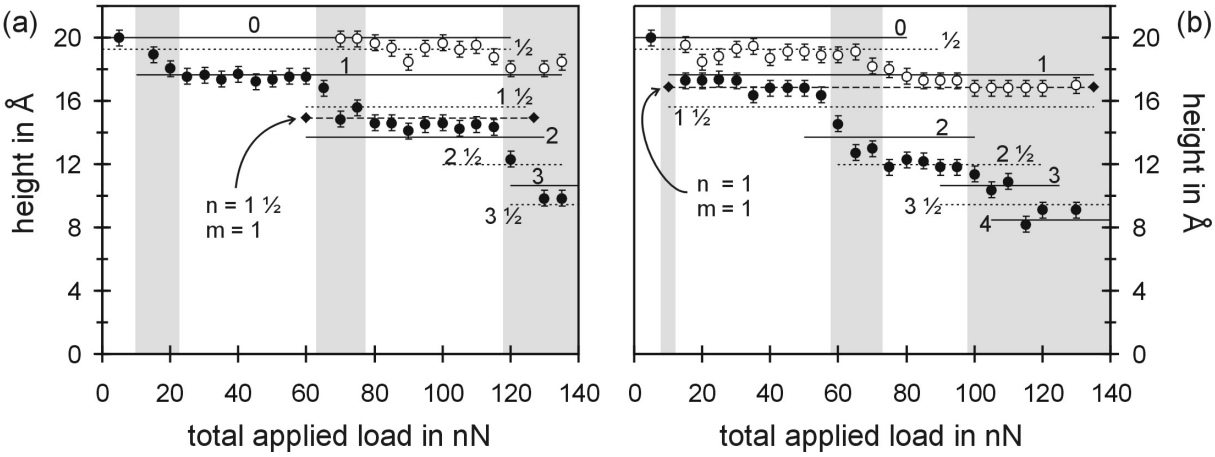

Figure 4.8: Examples of next nearest neighbor tilts in the height vs. load curves for two C12 alkylsilane islands of Figure 4.2. The dashed lines marked with diamonds at the end correspond to heights calculated including first order next nearest neighbor tilts. These heights match the data points better than any of the integer or half-integer values.

self-assembled monolayers, before any further refinement of the tilting model could be more than mere speculation.

4.4 Energy Calculations

The next step is to understand the connection between height changes and friction changes. The fact that tilting occurs at threshold loads implies that there is an activation energy for the tilting process. We performed energy calculations by summing pairwise r^{-6} van der Waals potentials between methylene units as illustrated in Figure 4.9. The zigzag shape of the alkylchain is neglected since these contributions are small and largely cancel out. To calculate the distance between methylene units $r_n(j)$ via Pythagoras' theorem one needs to know (i) the distance between the reference CH_2-unit and the CH_2-unit right above/below it (j=0) in the layer n and (ii) the distance within the layer n from each methylene unit to the one with j=0. While (i) is simply nd, (ii) is obtained from Figure 4.10, assuming hexagonal close packing within the layer. Thus the energy of a CH_2-unit due to the CH_2-units in a layer labelled n is the sum over the van der Waals terms between the reference methylene group and each of the methylene units j in that layer:

$$E(n) = \sum_j \frac{A}{r_n^6(j).} \tag{4.6}$$

Finally the total energy of a CH_2-unit within a monolayer is obtained by summing over all these layers:

$$E_{tot} = \sum_n E(n). \tag{4.7}$$

These calculations show that, after a rapid increase with chain length, the energy per methylene unit stabilizes after about ten carbon atoms in the alkyl chain [14]. The constant A is chosen in a way that the cohesive energy of one molecule (i.e. the sum over the total energies of all its CH_2-units) equals its sublimation energy, which corresponds to an energy per methylene unit of 7kJ/mol [95]. All energy calculations are based on a simple model, assuming a perfect hexagonal packing of the rigid molecules and ignoring defects. Even if every sixth molecule was missing, the result would change by only 10 %. If the molecules were indeed perfectly packed, it would be

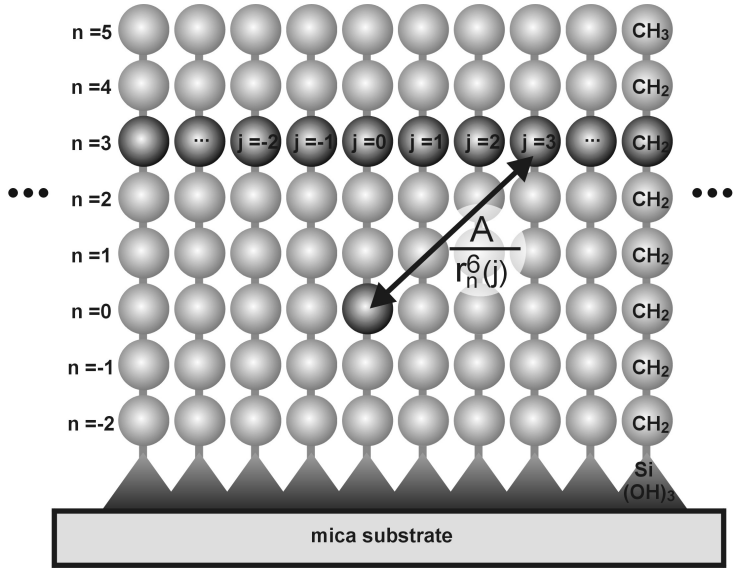

Figure 4.9: Schematic drawing of alkylsilanol chains adsorbed on a mica substrate to illustrate the summation of pairwise r^{-6} van der Waals potentials between methylene units to obtain the cohesive energy of the film. The energy of a CH_2-unit due to the CH_2-units in a layer n layers apart is the sum over the terms between the reference methylene group and each of the methylene units, labelled j, in that layer.

nearly impossible to tilt the molecules with an AFM tip. Thus defects are necessary to initiate the tilt.

Note, that as the molecules incline, the situation for a methylene unit well inside the film does not change, when again an interlocked position is assumed. Only the CH_2-units at the top and bottom will have lost some of their neighbors. Thus the situation is equivalent to a simple shortening of the chains and the results of the summation can still be applied, but have to be corrected for the shorter film height h (see Figure 4.5).

For the following considerations we will stick with the simpler integer-tilt model, as described in section 4.3.1. To slide the contacting molecules between two stable angles, their separation must be increased by approximately 0.2 Å ($d' - d$ in Figure 4.5), according to simple geometric considerations using the 2 Å van der Waals radius of a methylene group. This chain separation energy can be estimated to be the difference in cohesive energy per molecule in the optimal and the expanded configuration. For the first step, the result is 0.23 eV per molecule for C18, 0.20 eV for C16 and 0.15 eV for C12. To this energy one has to add the contribution from the loss in film height (approximately 1.6 Å for C18, 1.4 Å for C16 and 1.1 Å for C12) at the maximum separation, which is formally equivalent to a shortening of the chains and therefore a loss of cohesive energy. This contribution can be easily estimated to be about 0.10 eV for C18, 0.08 eV for C16 and 0.07 for C12. Figure 4.11 illustrates the loss in cohesive energy due to the chain separation energy required for the tilting motion and due to the loss in film height. In the presented model, when the threshold load is reached, the molecules under the tip overcome the barrier and collapse, i.e. tilt to the next stable position.

To reinforce these arguments, the increase in frictional work required to go from one plateau to the next is estimated to be equal to the total activation energy per molecule multiplied by the number of molecules in the contact area swept by the tip as it moves over the surface. Using Hertzian contact mechanics the contact radius is

$$r = \left(\frac{RL}{K}\right)^{1/3}. \tag{4.8}$$

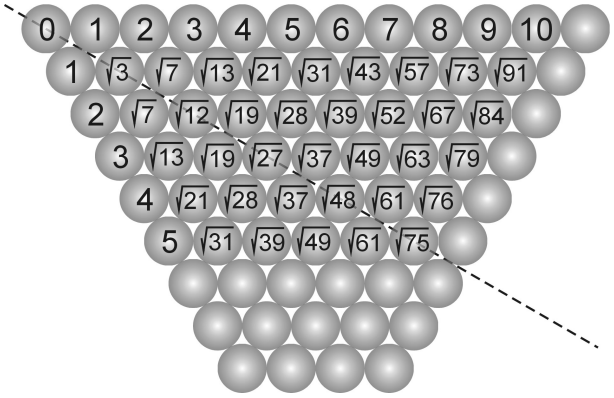

Figure 4.10: Schematic arrangement of CH_2-units in a layer n of the film. Numbers represent the distance to the CH_2-unit labelled j=0 in Figure 4.9 in units of the chain diameter d. Because of the six-fold symmetry of the hexagonally packed chains, only a 60° sector has to be considered. For calculating the energy of the whole layer the value of one sector has to be multiplied by a factor of 6.

From the measured tip radius (R) of 50 nm, a total applied load of 25 nN and the combined elastic modulus

$$K = \frac{3}{4}\left[\frac{1-\nu_1^2}{E_1} + \frac{1-\nu_2^2}{E_2}\right] \tag{4.9}$$

for alkyl chains (Young modulus E_1=9.3 GPa, poisson ratio ν_1=0.4) and silicon-nitride (E_2=140 GPa, ν_2=0.3), a contact radius of 4.5 nm is estimated, which sweeps over approximately five molecules per Å scanned. The increase in friction force for the first step then should be about 1.6 nN for C12, 2.2 nN for C16 and 2.5 nN for C18. For the C12 island of Figure 4.2(a) this is within a factor of two of the measured value of 1.1 nN (averaged over points # 4 - 11). For the C12 island of Figure 4.2(b) the measured value is smaller, about 0.6 nN (averaged over points # 2 - 10). These two islands were measured simultaneously in the same image, but the latter one collapsed earlier to lower levels and disintegrated at lower loads and more significantly, indicating a less tight packing of the molecules for the second island. For the big C16 island in Figure 4.3 the measured value of 2.0 nN frictional force (averaged over points # 5 - 7) for the first step differs only by 10 % from the calculated one. For a big C18 island (height and friction vs. load curve are not shown) the measured value is 8.6 nN frictional force (averaged over 8 data points),which is more than three times the calculated value. A possible explanation is that this sample was several days older than the C12 and C16 samples, thus the molecules might have packed more densely and even started to form silicon-oxide bonds at the bases. However, considering that the conversion of the photodetector signal into nN, estimated from typical lever dimensions, is connected with a possible error of a factor of 2, the agreement is excellent.
Including the half-integer tilts into these considerations is not trivial, since it is difficult to estimate the energy needed for a combined rotation and tilt of the molecules. Seeing how well the calculation for integer-tilts fits the measured values for the increase in friction, it is reasonable to say that the height of the energy barrier that has to be overcome for the tilting motion, will have the same order of magnitude, even when half-integer tilts are included. To adapt the schematic of Figure 4.11, each peak has to be replaced with an additionally valley, doubling the amount of stable configurations.
The complete recovery of the film height when decreasing the load after the first two steps indicates that the molecules resume their upright position within the time scale of the experiment. For activation barriers of approximately 0.2 eV, the “recovery time” for one molecule is extremely short, on the order of tens of picoseconds at room temperature. If, however, many

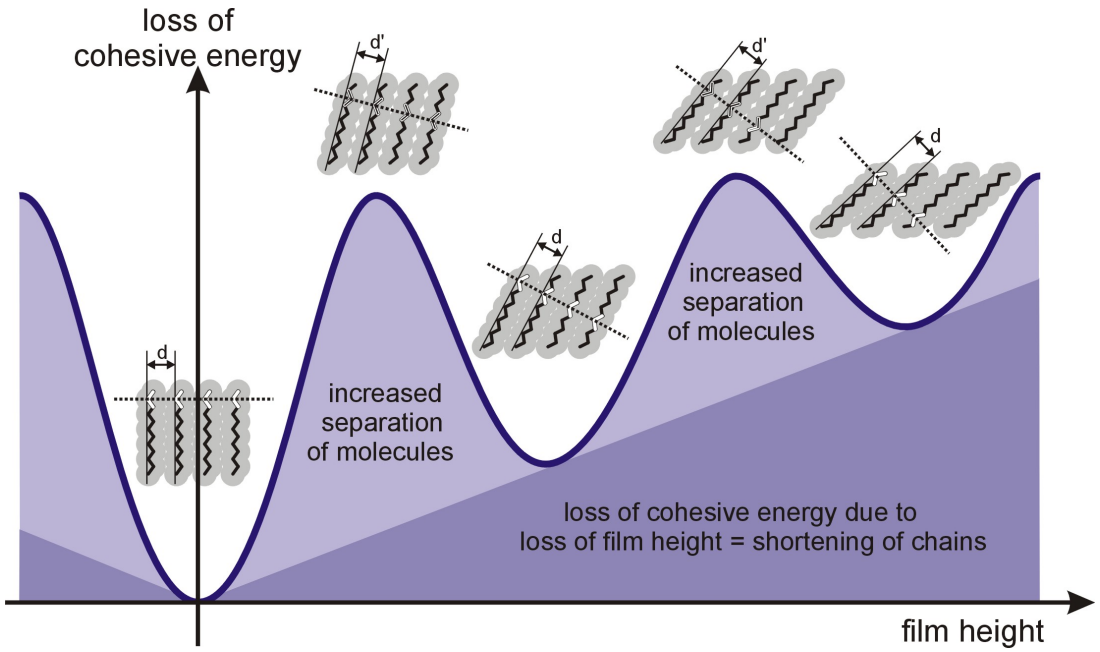

Figure 4.11: Schematic drawing to illustrate the loss of cohesive energy during the tilting process. The loss of cohesive energy consists of two components. One is the loss of cohesive energy due to missing neighboring methylene units caused by the tilting motion, which is equivalent to a shortening of the film height, i.e. a shortening of the chains. The second component is caused by the increased separation of the molecules, which is necessary to slide neighboring molecules past each other during the tilting motion.

molecules must tilt simultaneously (because of their interlocking), the recovery time could be very long. This would explain why metastable areas of lower heights (i.e. of tilted configurations) can exist without applying pressure, as has been observed in films made from fatty acids with the Langmuir-Blodgett technique [91].
The origin of the permanent deformations observed after the application of high large loads is not clear at present. It is likely that they are due to the production of more energetic deformations, such as gauche distortions. Once produced, these might be stabilized for longer time periods by entanglement with neighboring molecules.

4.5 Summary

A step-wise decrease in height is observed in self-assembled islands of alkylsilanes on mica as a function of imaging pressure. These steps in height are accompanied by simultaneous step-wise increases in friction. The height decreases match the values expected from the tilting of chains locked at angles of maximum packing density and the increase in friction force is consistent with the estimated activation energy required for the tilting motion. These experiments constitute the first example establishing a connection between molecular scale events and energy loss processes resulting in discrete frictional behavior.

Chapter 5

Thiol Monolayers on Gold

This chapter is dedicated to measurements of friction vs. load on special alkylthiol monolayers. Photo-polymerizable diacetylene groups are incorporated within the alkylchains of the monolayer, resulting in non-covalent electronic interactions between diacetylene groups. Under these conditions, a stepwise increase in friction is observed for increasing load, indicating a partial collapse of the monolayer at specific loads, in agreement with the tilting model presented in chapter 4. Subsequent photo-polymerization by UV irradiation results in covalent cross-linking between molecules and the creation of a linear conjugated backbone, which acts as an internal molecular scaffolding. This backbone significantly alters the frictional properties of the monolayer by inhibiting lateral displacement within the monolayer [96].

5.1 Introduction

Among the self-assembling monolayers the most extensively studied system are alkylthiols ($CH_3 - (CH_2)_{n\text{-}1} - SH$, referred to as Cn) on gold(111). They are easily prepared in a similar manner as the silanes, i.e. by immersing the gold substrate into a dilute solution of the molecules. Furthermore they can also be prepared by vapor deposition in ultrahigh vacuum. A big advantage for structural investigations on thiols compared to silanes is the fact that thiols form dense and highly ordered monolayers, on which routinely atomic lattice resolution AFM images can be obtained [48, 97, 98]. Atomic resolution has been achieved on silane monolayers prepared by the LB-technique [99], but only with great effort, i.e. by imaging in liquid.
To match the gold lattice the thiols usually assume a configuration with the molecules inclined by approximately 30° off the surface normal. The typical structure in atomic lattice resolution images is a $(\sqrt{3}x\sqrt{3})R30°$, but also a C(4x2) superstructure has been observed [87].
In analogy to the preparation of silane islands (see chapter 4), also thiol islands can be prepared by quick dipping (on the order of a few seconds) of the gold substrate into a dilute solution (on the order of 1 μM) of the molecules.
The structure and mechanical stability of such C16 and C18 thiol islands was investigated by Barrena *et. al.* [93, 94, 87]. They found that the thiol islands (i) can exist already in metastable tilted states, i.e. tilted further than the usual 30° angle, and can be "brushed", by applying pressure with the AFM tip, into their typical 30° tilt configuration, and (ii) also follow the tilting behavior as described in section 4.3. The tilting model presented by Barrena *et. al.* extends the 2D model to a 3D model by including next nearest neighbor tilts, as described in detail in section 4.3.3, to obtain an excellent agreement with their data. Furthermore the authors also found a stepwise increase in friction which coincides with the abrupt decrease of island height.
In the following we want to show, how the frictional properties of thiol monolayers can be manipulated by internal molecular scaffolding. Functional groups, which associate laterally,

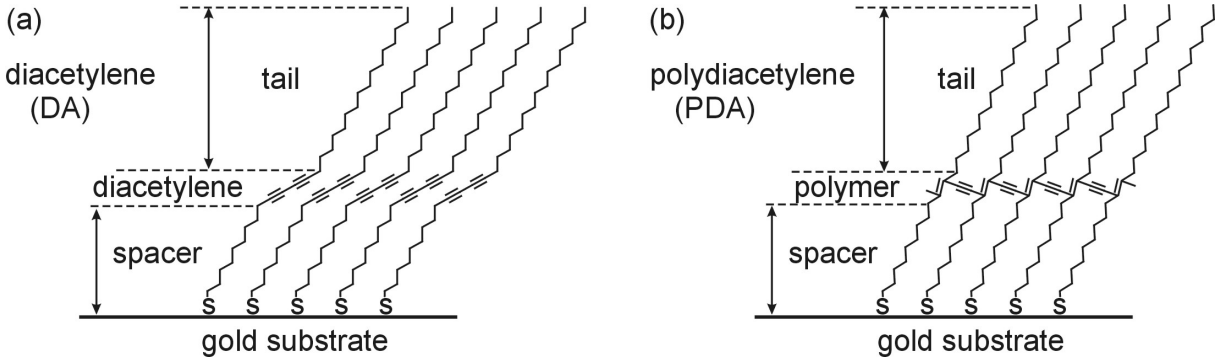

Figure 5.1: Schematic diagram of the molecular structure of (a) unpolymerized diacetylene and (b) polymerized polydiacetylene monolayers. The transition from (a) to (b) is accomplished via UV-irradiation.

can be incorporated within the alkylchains. These internal interactions may take the form of hydrogen bonding [100], dipole interaction [101], π-stacking [102], or covalent attachment [103, 104, 105]. Through these interactions, internal molecular scaffolding is created within the assembly which may impact the overall structure and properties of the monolayer. The incorporation of photopolymerizable conjugated diacetylene moieties within the hydrocarbon chains of these assemblies leads to monolayers with non-covalent internal molecular scaffolding. Upon polymerization, the structure contains a covalently linked, highly conjugated polymer backbone within a single molecular layer, as shown in Figure 5.1. Polymerization in diacetylene compounds is highly dependent on spatial organization, with tolerances for the distance between neighboring diacetylene groups of 0.5 Å [106]. Once formed, the conjugated polymer backbone possesses unique optical and electronic properties and a significantly increased durability to electrical, temperature and solvent extremes compared to conventional alkylthiol monolayers [104]. This combination of properties and high durability extends the range of applications for self-assembled monolayers on gold.

While the incorporation of diacetylene groups and their subsequent polymerization is known to significantly impact the structural properties of the assembly relative to n-alkylthiol monolayers [105], little is known about their effect on the mechanical properties. The diacetylene groups divide the monolayer into three regions (see Figure 5.1) which might contribute differently to the structural order of the film. In the polymerized structure, the presence of the conjugated polymer backbone is likely to significantly impact the mechanical properties of the monolayer. For example, the covalent cross-linking of the monomers is likely to greatly hinder the lateral displacement of the individual adsorbates under applied pressure. In addition the polymer is linear in nature and has been shown to form unidirectional domains in LB-films [107, 108]. These domains cause in a significant dependence of the frictional properties on the relative orientation of the scanning direction and the polymer backbone [109].

In this chapter, atomic force microscopy is utilized to assess the frictional properties of diacetylene and polydiacetylene monolayers under applied load. The effect of chain length and crystallinity is investigated as well as the impact of the presence of the polymer backbone in terms of its rigidity and directionality.

5.2 Sample Preparation

This chapter focuses on monolayers fabricated on gold substrates from diacetylene di-thiol precursors of the form

$$[\mathrm{CH_3} - (\mathrm{CH_2})_\mathrm{n} - \mathrm{C} \equiv \mathrm{C} - \mathrm{C} \equiv \mathrm{C} - (\mathrm{CH_2})_\mathrm{m} - \mathrm{S}]_2\,, \tag{5.1}$$

where *n,m*-diacetylene (*n,m*-DA) or *n,m*-polydiacetylene (*n,m*-PDA) indicate the unpolymerized and polymerized assemblies, respectively. The structure of the hydrocarbon chains is manipulated by synthetically varying the lengths of the tail (n) and spacer (m) region of the monomers. Molecules available for this study had the following values for tail and spacer:

n,m =	7,9	11,9	15,9
n,m =	15,4	15,6	15,9

In the former combinations the length of the tail is varied, while the number of methylene units in the spacer region is kept constant, and in the latter combination the length of the tail is kept constant and and that of the spacer varied.

The diacetylene group divides the monolayer into three distinct regions [Figure 5.1(a)]. In the alkyl tail region, the interactions between molecules are dominated by van der Waals forces which depend on the chain length, while in the spacer region the alkyl chains are additionally constrained by surface attachment. The region containing the diacetylene group provides additional electronic interactions between adjacent monomers. Upon polymerization, monomers are covalently linked, further constraining the spacer region. As a result, each of these distinct regions is expected to contribute to the overall monolayer structure. Octadecanethiol was used as a reference sample to allow direct comparison with a simple alkyl-based monolayer without internal molecular scaffolding.

The symmetrical diacetylene disulfides were synthesized and purified according to a method reported previously [110]. Octadecanethiol (98%) and chloroform (99.9+%)[1] were used as received. Ultrahigh-purity deionized water[2] was used for rinsing the monolayers. The substrates were fabricated from mica (ASTM V-2)[3] and gold (99.99%)[4].

The gold substrate were prepared using a custom-built UHV thin film deposition system. Mica was cleaved on both sides immediately prior to insertion into the vacuum chamber, where it was degassed at 400°C for 12 to 18 hours at pressures below $1 \cdot 10^{-8}$ Torr. Gold was subsequently evaporated at a rate of approximately 0.1 Å/s onto the mica substrates, which are maintained at 400°C by two halogen lamps. Following deposition of about 2000 Å of gold, the films were annealed at the deposition temperature for 4 h. After annealing the chamber was filled with dry nitrogen, and the gold substrates were immediately removed and placed into 1 mM chloroform solutions of the diacetylene disulfide or octadecanethiol of interest. Strict light control was maintained for all solutions to eliminate the possibility of spurious polymerization. After $40-48$ h the films were removed from the solution and rinsed extensively with chloroform and deionized water and then dried under a stream of dry nitrogen. Polymerization of the monolayers was accomplished under nitrogen using a low-intensity UV lamp[5] ($\lambda = 250-260$ nm) at a distance of 2 cm for 7 minutes. No evidence of photo-oxidation was observed using these irradiation conditions [111].

[1] both purchased from Aldrich Chemical Co., Milwaukee, WI, USA, www.sigma-aldrich.com

[2] resistivity > 18 MΩ, Model UV Plus Milli-Q, Millipore, Bedford, MA, USA. www.millipore.com

[3] obtained from Asheville-Schoonmaker Mica Co., Newport News, VA, USA. www.ashevillemica.com

[4] purchased from Kurt Lesker Co., Clairton, PA, USA. www.lesker.com

[5] Model UVG-11; Ultra-Violet Products Inc., Cambridge, UK. www.uvp.com

Table 5.1: Grazing incidence infrared spectroscopic peak positions for the asymmetric (CH_2-ν_a) and symmetric (CH_2-ν_s) methylene stretches. Values are reported with an error of $\pm$ 1 cm^{-1} as determined by replicate measurements.

sample	CH_2-ν_a [cm^{-1}]	CH_2-ν_s [cm^{-1}]
15,4-DA	2919	2851
15,6-DA	2919	2851
15,9-DA	2919	2851
11,9-DA	2924	2855
7,9-DA	2925	2855
octadecylthiol	2920	2851
crystalline alkanes	2918	2851
liquid alkanes	2924	2855

5.3 Friction vs. Load Measurements on Diacetylene Monolayers

All AFM measurements were performed with the home-built AFM, described in chapter 2, under ambient conditions. Measurements on unpolymerized monolayers were performed in the absence of UV light sources, i.e. fluorescent room lights were turned off. A single V-shaped lever (force constant of 0.4 N/m) with a conical silicon tip and a tip radius of approximately 30 nm was used for all measurements to allow direct comparison of the friction signal of different monolayers. Also care was taken to align the laser onto the same spot on the lever for each sample. The tip was evaluated before and after the measurements by imaging a silicon sample with a regular array of high aspect ratio conical features (as described in section 2.1.1) to check for damage and significant changes in tip radius. SEM images, also taken after the measurements, confirmed the tip radius and displayed no abnormal tip or cantilever shape.

5.3.1 Grazing Incidence FT-IR Measurements

Grazing incidence Fourier transform infrared spectroscopy (FT-IR) was performed using a nitrogen-purged spectrometer with a liquid nitrogen cooled MCT detector[6]. The grazing incidence accessory[7] was set at an angle of 85° with respect to normal, and p-polarized light was used for all measurements. The spectra were averaged over 1024 scans with a resolution of 2 cm^{-1}. All spectra were referenced to an unmodified gold film. Background spectra were recorded immediately upon removal of the gold substrates from the evaporator in order to minimize bias from surface contamination.

Table 5.1 summarizes the values measured for the peak positions for the symmetric and asymmetric methylene stretch frequencies for unpolymerized diacetylene samples and octadecylthiol. It also contains values for crystalline and liquid alkanes from the literature [37] for comparison. Note that the peak positions are not affected by polymerization [105]. Comparison of the peak positions for the 7,9-DA and 11,9-DA monolayers with those of solid and liquid hydrocarbons indicates that these diacetylene monolayers are more liquid like, i.e. are less crystalline [105]. In contrast to the 7,9-DA and 11,9-DA monolayers, the infrared peak positions for the 15,4-DA, 15,6-DA and 15,9-DA monolayers, i.e. for diacetylene monolayers with long hydrocarbon tails, are similar to those of the octadecylthiol and are representative of highly crystalline alkyl chains,

[6]Nicolet 550 Magna IR, Thermo Nicolet, Madison, WI, USA. www.nicolet.com

[7]Thermo Spectra-Tech, Shelton, CT, USA. www.spectra-tech.com

Table 5.2: Adhesion measured via the tips pull-off force [nN] for the various unpolymerized and polymerized diacetylene thiol monolayers and bare gold

sample	unpolymerized	polymerized
15,4-DA	32.0 ± 0.3	30.1 ± 0.3
15,6-DA	29.9 ± 0.1	34.4 ± 0.6
15,9-DA	29.5 ± 0.2	26.7 ± 0.2
11,9-DA	40.9 ± 0.2	32.6 ± 0.3
7,9-DA	32.7 ± 0.4	27.0 ± 0.9
octadecylthiol	24.3 ± 0.8	NA
gold	44.0 ± 2	NA

regardless of the spacer length. Recent spectroscopic studies have indicated that the alkyl tail and spacer regions do exist in different structural environments [105]. In particular, although 15,4-DA, 15,6-DA and 15,9-DA appear very similar by infrared peak positions, the combination of changes in spacer length and the odd/even character of the number of methylene units in the spacer causes significant changes in the structure of the spacer regions. Although small changes in tilt and/or twist have been detected spectroscopically, polymerization in diacetylene monolayers is known to have a negligible effect on the overall methylene chain crystallinity. However, covalent attachment of adjacent molecules within the monolayer assembly considerably alters the mechanical properties of the monolayer, as will be shown in the following.

5.3.2 Adhesion Measurements

In addition, adhesive properties of the film were examined by acquiring force vs. displacement curves. Table 5.2 shows the pull-off forces for the different monolayers before and after polymerization, as obtained from force vs. displacement curves. The pull-off force for octadecylthiol is the lowest and represents the least adhesive sample in this study. The higher pull-off forces in all polymerized and unpolymerized diacetylene monolayers may be due to a higher compressibility, leading to larger contact areas at pull-off. This result is in agreement with previous wettability studies, demonstrating a slightly increased disorder at the air-monolayer interface in the diacetylene monolayers compared to octadecylthiol [105]. Indeed higher pull-off forces are required for those monolayers with the lowest chain crystallinity. Upon polymerization, the pull-off forces of the diacetylene monolayers decrease slightly, with the exception of the 15,6-polydiacetylene monolayer. Since no change in methylene crystallinity is observed upon polymerization, simple alteration in the methylene packing is not implicated in this decrease of adhesion. However, the decrease could be due to the changes in alkyl chain twist/tilt upon polymerization and an increased rigidity of the overall film caused by the covalently cross-linked polymer backbone.

5.3.3 Friction vs. Load Measurements on Unpolymerized (DA) Monolayers

Friction vs. applied load curves were obtained with the "line by line" method, scanning along a 75 Å long line, as described in section 2.2. Note, that since the cantilever is mounted at an angle of approximately 15° from the sample surface, the tip moves by about 50 nm (in the direction parallel to the lever), as the load is increased to its maximum, covering a load range of 70 nN in these experiments. The load was cycled in one image from a minimum to a maximum value and back over 256 scan lines. The first part of increasing load will be referred to as the approach portion and the second as the retract portion or the friction vs. load curve. Friction vs. load

curves were also measured for a octadecylthiol film to allow direct comparison with a simple alkyl-based monolayer without internal molecular scaffolding.

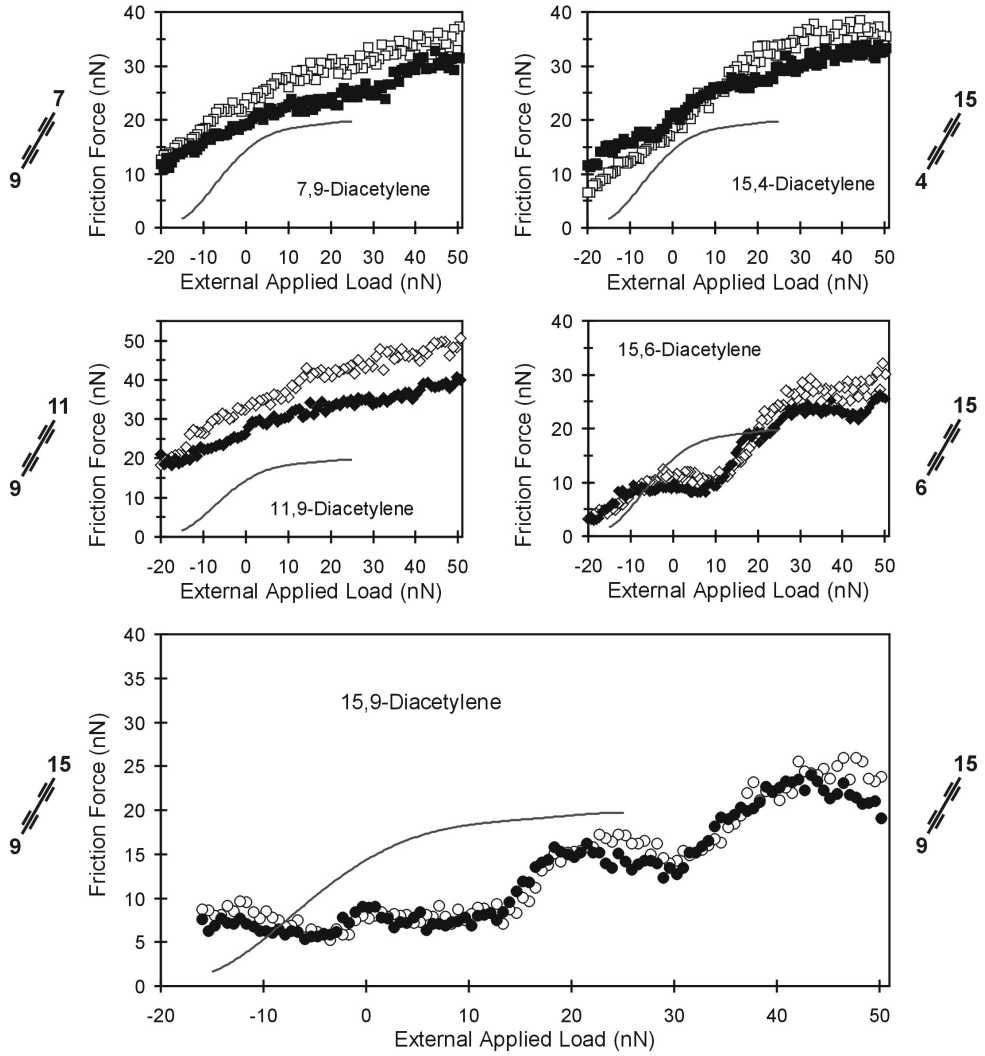

Figure 5.2: Friction vs. external applied load curves for unpolymerized *n,m*-diacetylene monolayers. Curves on the left hand side correspond to molecules where the tail length (n) is varied while the spacer length is fixed at $m = 9$, curves on the right hand side correspond to molecules where the tail length is fixed at $n = 15$ and the spacer length is varied. The curve for the 15,9-DA monolayer applies to both cases. The approach and retract branches of the curve are shown as filled and open symbols, respectively. The solid curve corresponds to a measurement (averaged and smoothed) on an octadecylthiol monolayer, for comparison.

The influence of molecular architecture on the monolayer frictional properties is shown in Figure 5.2 for the unpolymerized layers. Note, that friction is plotted vs. external applied load. To obtain the total applied load, the adhesive force as measured by the pull-off force given in table 5.2 has to be added. The effect of varying the alkyl tail length while maintaining a constant spacer length is illustrated on the left side of Figure 5.2 for 7,9-DA and 11,9-DA. Although these two monolayers have longer overall chains than the octadecylthiol, they exhibit a measurably higher friction at all applied loads. In addition, hysteresis between the approach and retract portion of the curves is observed. This is consistent with the lower alkyl chain crystallinity observed for these monolayers with FT-IR (see Table 5.1). The decreased crystallinity, higher

friction, and hysteresis of these two monolayers are consistent with previous observations of higher friction in the short-chain alkylthiol assemblies, a result that was ascribed to the increased degree of disorder [13]. The somewhat higher friction response in the 11,9 compared to the 7,9 assembly is counterintuitive based on chain length correlations. However, the effect is rather small and might originate from small differences in the overall structural order in the different samples used here.
For the 15,9-DA monolayer little hysteresis and diminished friction at all loads are observed as compared to the 7,9-DA and 11,9-DA systems (see Figure 5.2). This observation is consistent with the expected relationship between highly crystalline chain structures (see Table 5.1) and decreased friction. The magnitude of the friction response at most applied loads is less than that for the octadecylthiol monolayer. Interestingly and unlike the octadecylthiol or the 7,9-DA and 11,9-DA monolayers, abrupt and reversible changes, separated by plateau regions, are observed in the friction vs. load curves for the 15,9-DA and to a lesser extent for the 15,6-DA assembly. Looking back at the observations of a stepwise increase in friction vs. load curves accompanied by a stepwise decrease in height of alkylsilane islands (chapter 4) and alkythiol islands [93], the occurrence of such a stepwise increase in friction with increasing load on the 15,9-DA and 15,6-DA monolayers does not strike as too unusual. Apparently, for these longest two diacetylene molecules, which are significantly longer than the simple alkylthiol counterparts, discrete tilts, as described in section 4.3, represent a possible energy dissipation channel. Unfortunately, a direct comparison with those studies was not possible because simultaneous changes in the film height under load could not be ascertained, due to the continuous nature of these monolayers.
The effect of varying the alkyl spacer length while maintaining a constant tail length is illustrated by measurements on 15,4-DA, 15,6-DA and again 15,9-DA monolayers, presented on the left side of Figure 5.2. Consistent with the high crystallinity observed in the FT-IR measurements (see Table 5.1), the monolayers exhibit minimal hysteresis in the friction vs. load curves. There are, however, significant differences in the magnitude and shape of the friction vs. load curves. As the spacer length is shortened, the friction force increases, particularly at high loads. Even more striking, the number of plateaus in the friction vs. load curve decreases when going from the 15,9-DA to the 15,6-DA, and for the 15,4-DA film, no plateaus can be found. It appears that the high degree of crystallinity observed for monolayers with a 15 carbon atoms long tail chain is necessary, but not sufficient for a stepwise response of the film properties to load. In addition, the spacer length appears to play a large role in determining the existence of this stepwise response, with longer spacer lengths favoring this collapse behavior as a function of applied load.

5.3.4 Friction vs. Load Measurements on Polymerized (PDA) Monolayers

The diacetylene monolayers are photo-polymerized by UV-irradiation, yielding a highly conjugated polydiacetylene backbone within the hydrocarbon chains of the monolayer. Consistent with LB-films, polymerization on gold is also expected to result in the formation of unidirectional polymer domains. The maximum size of the domains is ultimately constrained by the size of atomically flat regions of the evaporated gold substrate (> 100 nm).
Figure 5.3 shows the approach portions of the friction vs. load curves acquired at four macroscopically separated locations (several micrometers) on a 15,9-DA and a 15,9-PDA monolayer. Highly consistent friction vs. load curves are observed for the unpolymerized film. In contrast, the polymerized monolayer exhibits significant variations in frictional properties at different locations on the film. Interestingly, the stepwise change in friction is lost upon polymerization (the same loss in transitions is observed for the 15,6-DA after polymerization, data not shown). The variation of frictional properties for different locations on the polymerized sample is likely due to differences in the orientation of the polymer domains relative to the scan direction. In the limiting case, if the polymer backbone is oriented parallel to the tip scan direction, the tip does

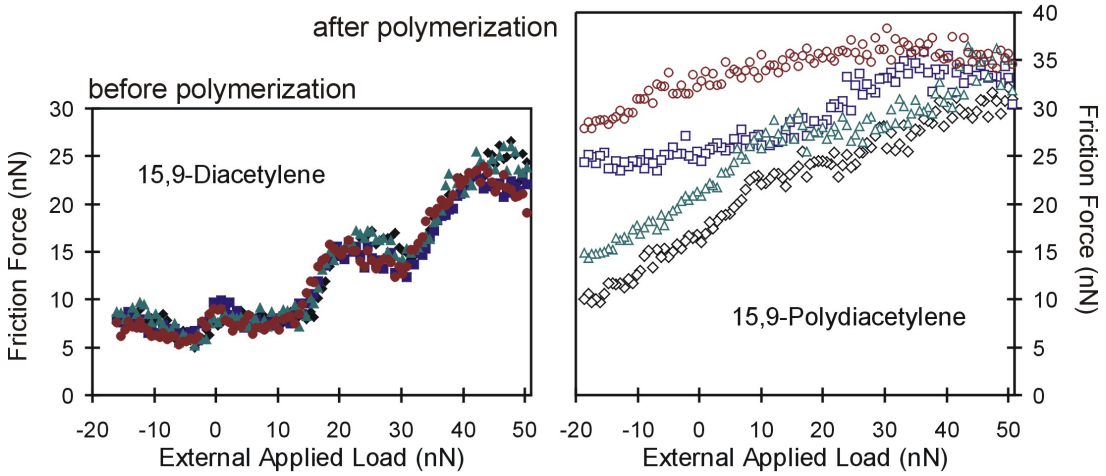

Figure 5.3: Comparison of friction vs. external applied load curves for a 15,9 monolayer before and after polymerization. The four approach curves shown in each graph represent four different locations on the monolayer surface separated by several micrometers. The retract portions of the curves are omitted for clarity.

not cross over the linear polymer chains. However, if the polymer backbone direction within a domain is perpendicular to the tip scan direction, it will cross numerous polymer chains during the friction measurements (approximately 15 polymer chains are expected for a 75 Å long scan line). Given the high degree of polymerization in the 15,9-PDA monolayers [105], it is unlikely that the variations in the friction vs. load response are due to spurious regions of incomplete polymerization. The friction anisotropy due to alignment of scan direction an polymer backbone was studied in detail by Carpick *et. al.* [109] for polydiacetylene monolayers obtained as LB-films, polymerized on the water surface and subsequently transferred onto the substrate.

The disappearance of the plateau structure upon polymerization is consistent with the covalent cross-linkage, preventing the small lateral displacements that are necessary for discrete tilting of the polymethylene chains. Although, in principle, collapse can still occur for an entire polymer chain in the direction perpendicular to the backbone, such collective inclination likely requires much more energy and exact directional application of loads.

5.4 Summary

In this chapter it has been demonstrated, that manipulation of the frictional properties of single-monolayer films can be accomplished by internal molecular scaffolding. In the present case, this control of molecular properties was achieved using adsorbates containing diacetylene groups inside the alkyl chains. These groups provide non-covalent van der Waals and electronic interactions and are subsequently covalently cross-linked by photo-polymerization to form a conjugated linear backbone within the methylene chains. The result from the friction vs. load experiments indicate that variations in the frictional properties of the unpolymerized structure are related to the position of the diacetylene group in the alkyl chain. The length of both the tail and spacer regions is important in determining the friction properties. The overall length of the molecules has to be significantly increased (to 26 and 31 carbon atoms for the 15,6-DA and 15,9-DA, respectively) to achieve a comparable lubrication effect as on a simple 18 carbon long alkylthiol monolayer. Moreover, discrete and reversible transitions are observed for the longest chain diacetylene monolayers. As previously observed for islands of alkylsilanes

on mica and alkylthiols on gold, the origin of the plateau regions in these continuous films is most likely discrete tilting of molecules under applied pressure, dictated by the interlocking of the zigzag geometry of the carbon chains. The stepwise behavior in friction disappears upon polymerization, consistent with prevention of lateral displacement of the molecules upon cross-linkage. Finally, a significant spatial variation in frictional properties is observed for the polymerized layers, consistent with the expected differences in polymer backbone alignment relative to the scan direction for different domains.

Chapter 6

Summary and Outlook

Summary

The goal of this thesis was to investigate friction and wear with an atomic force microscope (AFM) at the nanometer scale, with the focus on wear on muscovite mica, a layered sheet silicate, and friction on self-assembled monolayers of model lubricants. During the course of this study, two energy dissipation mechanisms could be isolated and investigated separately.

On muscovite mica, repetitive scanning with a sharp tip (radius $\sim$ 40 nm) at moderate loads (80 - 100 nN) is found to cause the rupture of Si-O bonds at the surface. The production of these surface defects has a significant contribution to friction, although no damage is visible in contact AFM images, indicating that these defects could be point defects. The contribution of defect production to friction is explained by a simple model, based on the stress-induced enhancement of the rate of thermal defect production.

When the defects accumulate, a 2 Å deep wear scar forms, which has not been observed with AFM before. So far only 10 Å deep holes, corresponding to the removal of a complete unit cell, were reported for scanning at high loads. Furthermore, these 2 Å deep holes only form in the presence of water (i.e. at a humidity above 50 %), which significantly lowers the activation barrier for breaking a Si-O bond, since dangling bonds can be capped off with OH and H groups. The new surface inside the 2 Å deep hole has a lower surface potential and a smaller periodicity than the undamaged regions. The measured periodicity corresponds to the arrangement of atoms in the newly exposed layer.

On monolayer islands of alkylsilane molecules self-assembled in an upright, *all-trans* configuration on mica, a stepwise decrease of island height as a function of pressure applied by the tip is observed. These steps in height are accompanied by simultaneous stepwise increases in friction. This behavior can be explained with a two-dimensional nearest neighbor tilting model. Meta-stable configurations are achieved when alternating methylene units of one chain nest in the corresponding depressions of the neighboring chain, thus optimizing the packing density. The measured island heights fit very well with those calculated from the tilting model.

The activation energy necessary to go from one meta-stable tilted configuration to the next can be estimated by summing attractive van der Waals potential terms between the methylene units in the monolayer. The measured increase in friction force is consistent with this estimate.

These experiments on the alkylsilane islands are the first example establishing a connection between discrete structural changes at the molecular level and energy dissipation processes resulting in discrete frictional behavior.

Pressure-induced transitions between meta-stable states of interlocked molecules can be observed also for alkylthiol monolayer islands on gold. The manipulation of frictional properties by internal molecular scaffolding is demonstrated on monolayers of thiols on gold with a photopolymerizable diacetylene group incorporated into the alkyl chain. Unpolymerized monolayers

with a fairly long alkyl chain above and below the diacetylene group show again a stepwise increase in friction with increasing applied load. Upon polymerization by UV-irradiation a linear polymer backbone forms, which covalently cross-links the molecules, similar to pearls on a string. This backbone prevents the relative motion of the molecules necessary for tilting and therefore the steps in the friction vs. load curves vanish upon polymerization.

Outlook

Besides the collective tilting motion of the molecules, other modes of energy dissipation are possible, e.g. the production of *gauche defects*, i.e. the rotation of part of the alkyl chain around a C-C axis. The challenge of an experiment to measure the contribution of such gauche defects to friction is the sample preparation. An ideal sample would consist of a densely packed monolayer containing a certain percentage of longer, protruding chains. The friction should increase with an increasing percentage of longer chains, i.e. with the increasing amount of gauche defects created under the tip.
The preparation of such "mixed" monolayers has proven to be very difficult, especially avoiding phase separation. One measurement was obtained by Barrena and coworkers, but only a 1:1 mixture of 12 and 16 carbon units long thiols could be prepared. Promising experiments are currently underway in the group of Dr. Salmeron at the Lawrence Berkeley National Laboratory.
To confirm the production of gauche defects on such mixed layers, surface sensitive spectroscopic measurements would be helpful. For example a combination of a surface forces apparatus and sum frequency generation would allow to measure the increase of CH_2 vibrational modes. Besides the problem of sample preparation, which in this case also requires to spectroscopically "label" one of the molecules by e.g. a deuterated chain instead of a hydrogenated, there are some other issues, e.g. the birefringence of mica and the necessary passivation of the backside of the sample to optimize the signal to noise ratio. Therefore such an experiment will be time consuming and challenging, requiring a detailed knowledge of both techniques, the surface forces apparatus and sum frequency generation.
Regarding instrumental improvements, the setup used for the presented measurements could be improved by adding a mirror, a microscope and maybe even a camera to view the tip-sample alignment. An issue, which can only be resolved by major changes to the current design, is the option to macroscopically move the tip relative to the sample in a controlled way. Micrometer distances are achieved by slightly tilting the head on the approach screws, but larger distances are currently accomplished by nudging the sample puck with tweezers.
In Figure 6.1 a "special procedure" to inspect the shape of an AFM tip is suggested, which will not be practical in the near future.
Besides the interesting and surprising discoveries which were achieved in the field of nanotribology during the course of this thesis work, it is astonishing and encouraging that significant insights can be gained with such a fairly simple setup.
Finally, one should never forget that exciting discoveries rarely start with "Heureka, I got it!" but rather with "Hmm, that's funny..."

Figure 6.1: A different approach for AFM tip characterization. For many applications of AFM it is important to know the shape of the the tip. Unfortunately, the method suggested in this picture will not be practical until it is possible to shrink humans down to a few micrometer as in the science-fiction movie “Fantastic Voyage (1966)”.

Appendix A

Lithographically Patterned Thiol Monolayers

This Chapter is dedicated to Scanning Polarization Force Microscopy (SPFM) measurements (see Section 2.3) of water adsorption on lithographically patterned thiol monolayers on gold, i.e. monolayers with micrometer sized hydrophobic and hydrophilic domains [112]. This subject does not seem to be related to the topic of friction measurements on self-assembled monolayers, but considering that adsorbed water layers usually increase adhesion between an AFM tip and the sample, i.e. adhesion between nanometer sized contacts, and that furthermore water is an excellent solvent with the potential to greatly harm monolayer assemblies (by penetrating through pinholes in the film), such measurements are complementary to friction measurements. As briefly mentioned in the introduction about self-assembling monolayers, many aspects influence the quality of the films and just so will certain parameters (e.g. temperature or humidity) determine their performance over time.
Besides fundamental wetting studies patterns of hydrophobic and hydrophilic domains with micrometer dimensions could find applications as "chemical channels" instead of geometric channels, as sensors or micro-vessels to decrease reaction volumes [113, 114].
Although the following measurements started out very promising, the limited supply of samples, technical difficulties and time constraints prevented the final breakthrough, i.e. the observation of droplets nucleating, growing, spreading and evaporating on these patterned samples.

A.1 Sample Preparation

All samples were prepared from ten carbon-units long alkylthiols self-assembled on gold[1]. For the hydrophobic areas of the patterns, two types of molecules were available, one with a per-fluorinated (labelled F) and one with a per-hydrogenated alkyl chain (labelled CH_3). For the "hydrophilic" areas, a per-hydrogenated and CH_2-OH terminated molecule was used (labelled OH). This alcoholic termination achieved still a contact angle of about 50° for pure monolayers, which cannot be considered hydrophilic (contact angle of 0° or at least close to it), just less hydrophobic than the CH_3 terminated or totally per-fluorinated chains. A COOH termination would have been desirable instead to obtain a really hydrophilic surface, but could not be synthesized in time.
For the substrates, gold was evaporated to a thickness of $\sim$ 50 nm onto silicon wavers under vacuum (10^{-6} torr), yielding an rms roughness measured by AFM of $\sim$ 0.7 nm, with domains equal or smaller than 100 nm. The gold substrates were immediately immersed into a 1 mM solution of the first type of thiol molecules in ethanol for at least 24 h to form the initial monolayer.

[1]The samples were provided by Craig Priest, Ian Wark Research Institute, University of South Australia.

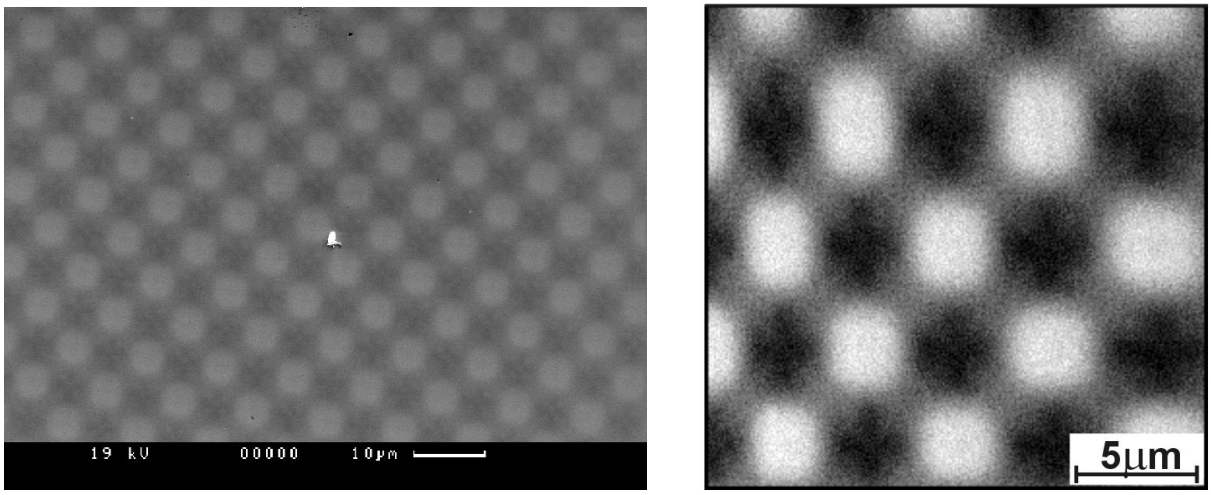

Figure A.1: (left) SIMS image of a 5 μm square pattern of per-fluorinated and per-hydrogenated alkylthiols on gold, the latter with a CH_2-OH termination. Shadowing and edge effects of the lithography method are clearly visible. (right) SPFM image, i.e. surface potential contrast, of the same 5 μm square pattern. Clearly the same structures as in the SIMS image can be resolved. Image size is 20×20 μm^2.

Subsequently the monolayer was irradiated for 4 h through a mask (chromium on glass) with intense (~ 10 mW/cm^2) light source with UV components to oxidize the sulfur-gold bond [115], followed by a rinse with ethanol. Immersion into a solution of the second type of molecules (again a 1mM concentration in ethanol), led to the replacement of those molecules with an oxidized sulfur-gold bond. A crucial parameter is the immersion time in the second bath. Since adsorption of thiols into confined areas can occur about a hundred times faster [116], much shorter immersion times of 30 minutes to 1h are necessary. Once all photo-oxidized molecules are replaced, also those initially not affected by the UV-light will slowly be replace by the second type, especially in case of the more reactive fluorinated molecules.
The patterns consist of either circles or squares with dimensions of 2, 5, 10 or 20 μm and are formed by the two combinations of per-hydrogenated chains with CH_2-OH termination and per-fluorinated chains or per-hydrogenated chains with CH_3 and CH_2-OH termination. They will be abbreviated in the following with F-OH and CH_3-OH.
Patterns of the F-OH type can be imaged by SIMS (secondary ion mass spectroscopy), see e.g. Figure A.1, or SEM, while the CH_3-OH type patterns, which differ by only one oxygen atom in the terminal group, show no contrast for these methods.

A.2 AFM Measurements

A.2.1 Surface Potential Measurements

All AFM and SPFM measurements were obtained on the AFM described in Chapter 2 and a similar setup with larger scan range of up to 20×20 μm^2 and vacuum capability. The samples investigated in detail are a 5 μm square and a 2 μm circular F-OH pattern and a 10 μm square CH_3-OH pattern. Other samples turned out to be dirty, or have less distinct areas, indicating problems in the assembly/patterning process.
For the F-OH samples a clear contrast in expected in the surface potential, dictated by the significantly different electronic structure of the hydrogen and fluoride atoms. As can be seen for the example of a 5 μm square pattern in Figure A.1, the pattern, including the fine structure caused by shadowing and edge effects of the lithography technique, is resolved as well as in the

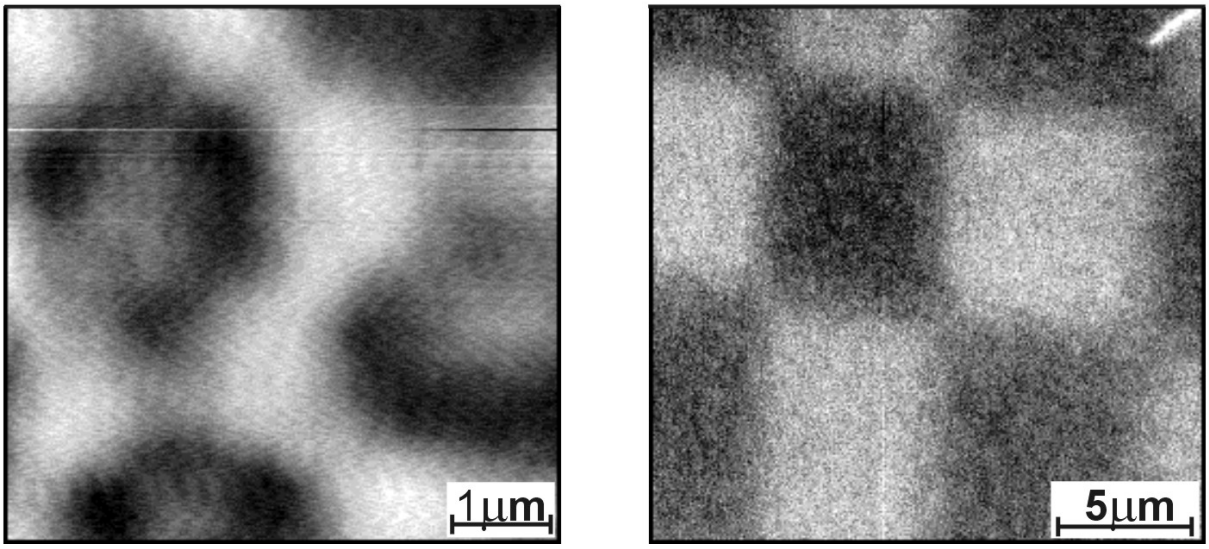

Figure A.2: (left) Surface potential image of F circles with a diameter of 2 μm. The circles have coalesced to form doughnut-like shapes, i.e. the resolution limit of the preparation method is reached. Image size is 5.5 × 5.5 μm^2. (right) Surface potential image of a 10μm CH_3-OH square pattern. Although the difference between the two areas is just one oxygen atom in the terminal group, still a contrast of about 10 mV can be detected. Image size is 20 × 20 μm^2.

SIMS image. As determined on a circular pattern, where a clear distinction is possible, the OH regions appear brighter, i.e. have a higher surface potential relative to the per-fluorinated areas. The surface potential difference was measured as a function of humidity on the 5 μm squares with the vacuum capable AFM. The humidity was determined by the partial pressure inside the chamber, after initial evacuation and subsequent backfilling with water vapor. There is only a slight increase of about 20 % with increasing humidity in the surface potential difference: For 0 % RH a value of 115 ± 5 mV was obtained, for 50 % RH of 132 ± 5 mV, and finally for 100 % RH it remained at 134 ± 5 mV, all for a tip-sample separation of 50 nm.
Furthermore a contrast in friction could be expected for contact mode images. Only on the 5 μm square pattern an increased friction was observed for the OH regions relative to the F regions, while for the 2 μm circles no friction contrast could be detected.
SPFM images of the 2 μm circular pattern have again a clear contrast in the surface potential, but as can be seen in Figure A.2 the resolution limit of the lithographic patterning method is reached: Instead of the expected dark (F) circles with a diameter of 2 μm arranged in a hexagonal array the imaged structures have a doughnut-like shape, formed from coalesced circles.
On the CH_3-OH samples, the difference in surface potential, caused by just one oxygen atom more in the terminal group of the OH region, is much smaller but still detectable, see Figure A.2. For a 10 μm square CH_3-OH sample, measured with the same setup and at the same tip-sample distance of 50 nm as for the 5 μm square F-OH sample, the surface potential difference was determined to be $\sim 8-10$ mV at 0 % RH and $12-14$ mV at 100 % RH, again a slight increase with increasing humidity.

A.2.2 Droplets

To achieve an *in situ* nucleation of water droplets on the sample only and not the complete setup, the sample has to be cooled below room temperature in a high humidity atmosphere. Condensation, visible by eye, could be achieved with a special sample holder puck containing a thermoelectric cooling element (see Appendix B) by lowering the sample temperature about

5° below room temperature in a 70 % RH atmosphere. Unfortunately, due to the more or less hydrophobic nature of the samples, this non-equilibrium process of droplet condensation and growth happens much faster than could be imaged by SPFM. Once the nucleation of a droplet is detected by SPFM it grows rapidly in size, exceeding the z-range ($\sim$ 1 μm) of the setup within a few tens of seconds. Note, that in SPFM the topography contrast of water droplets will be exaggerated due to the dielectric properties of water compared to those of the substrate. Subsequent evaporation of the droplet tends to leave a layer of contaminants sometimes even in a deceptive droplet shape.

A.3 Summary and Outlook

It has been demonstrated that SPFM is capable of imaging patterns of hydrophobic and hydrophilic alkylthiol molecules with micrometer dimensions. Even surface potential differences of 10 mV between CH_3 and CH_2-OH terminated regions could be determined. Furthermore, holes in the film with a diameter down to 500 nm exposing the bare gold, could be easily detected (images not shown).
To be able to image droplet condensation, growth and evaporation, the following improvements will be necessary:

- The hydrophilic regions have to consist of molecules with a truly hydrophilic termination such as -COOH [117] or of a bare hydrophilic substrate such as silicon [118].
- Using a liquid with a lower vapor pressure than water should be considered, e.g. hexaethylene glycol [118].
- The volume of the chamber around the AFM head has to be decreased to achieve a better control of the humidity.
- Furthermore it would be advantageous for AFM measurements to use longer chain thiols (e.g. C18) to obtain a greater stability of the monolayers for contact measurements.

Extensive studies in the area of droplet formation on patterned substrates are currently in progress in the group of Professor Herminghaus at the University of Ulm, Germany.

Appendix B

Construction of the AFM Head

The setup described in chapter 2 and used for the measurements presented in this work, belongs to the veterans among AFMs. It was originally designed and built by Kolbe *et. al.* [50] in 1992. It has been operated since and delivered results for various publications, mainly in the field of friction on model lubricants [47, 13, 49]. Several copies of this setup have sprouted around the world. As any AFM it has its advantages and disadvantages, but in general it is a very versatile design.
The following contains a collection of construction drawings, photos and a part list to built this AFM. Furthermore some suggestions on modifications and improvements will be given.
Note on copyrights: The reader is welcome to built a copy of this AFM, there is no patent on the design, but if you intend to do so, please inform Dr. Miquel Salmeron[1]. Do not follow these instructions blindly, there might be some mistakes or ambiguities in the drawings which slipped by, and there is no no warranty connected with the publication of this information. Furthermore, if you have achieved a significant improvement[2] of your setup, you are welcome to convey the respective drawings to Dr. Salmeron.

B.1 List of Parts

Please note, that the companies listed here may not be the only ones selling these parts. It is possible to find equivalent pieces from other supplies. For simplicity the list contains only a minimum of choices. Prices are as of summer 2000. The numbers in brackets correspond to those in Figure 2.1 and 2.2.

- one piezo tube, 0.5" OD x 0.020" W x 1.00" H, PN# OP EBL2 (9) — $ 165.00
  Staveley Sensors, E. Hartford, CT, USA.
  www.staveleyndt.com
  (1-860-289-5428)

- one photo-detectors, active area 2.5 x 2.5mm, PN# SPOT-4D (5) — $ 31.50
  UDT Sensors, Inc., Hawthorne, CA, USA.
  www.udt.com
  (1-310-978-0516)

- two manual micropositioners, PN# 35-2799 (2) — $ 245.00 each
  Coherent, Auburn, CA, USA.
  www.cohr.com or www.ealing.com
  (1-800-343-4912)

[1] Lawrence Berkeley National Laboratory, Berkeley, CA, USA. MBSalmeron@lbl.gov
[2] i.e. a practical improvement which actually works, not good ideas!

This part was originally from the British company *Ealing*, which was bought by Coherent. It is not mentioned in Coherent's catalogue, but it is available upon request. The advantage of this piece over other translation stages are the square outside dimensions of 35 mm x 35 mm, which allow to mount them easily on top of each other at a 90° angle to position the laser.

- two miniature translation stages, PN# M-MR1.4 (6) — $ 129 each
  Newport Corporation, Irvine, CA, USA.
  www.newport.com
  (1-800-222-6440)

- one open loop motorized stage, PN# CMA35 CC (12m) — $ 500
  Newport Corporation (see above)

- one hand-held controller, PN# 861 — $ 209
  Newport Corporation (see above)

- cable for hand-held controller, PN# 860I-10 — $ 16
  Newport Corporation (see above)

- two fine adjustment screws, PN# AJS-0.5 (12) — $ 24 each
  Newport Corporation (see above)

- one collimation tube and optics, PN# LT230P5-B [inside (1)] — $ 104
  includes lens with f=4.50 mm and 0.55 NA
  ThorLabs
  Newton, NJ, USA.
  www.thorlabs.com
  (1-973-579-7227)

- one laser diode socket for 5.6 mm laser diode casing, PN# S7060 [inside (1)] — $ 3.98
  ThorLabs (see above)

- one laser diodes, I=650 mm, P=5mW, PN# TOLD9442M (*) — $ 88.20 for six
  ThorLabs (see above)

In addition to the parts listed above and the pieces in the following drawings you will also need a frame, from which to suspend the AFM, i.e. the "support ring", for vibration isolation. Furthermore, about 3 meters of soft rubber tubing for the suspension (13), a cylindrical magnet with a diameter of approx. 0.250 inch and a height of about 0.25 inch (depending on the strength), some wires with colorful insulation (to make life easier), some meters of 10 line flat ribbon cables, three 0.125 inch diameter sapphire/stainless steel balls for each tip holder and some other "thingies" usually present in a lab will be required.

Note on housekeeping: The list of parts contains only the minimum number of pieces necessary to built one AFM head. However, it is highly recommended to have some (3 - 5) spare laser diodes, one photo-detector and one piezo tube in stock, preferentially well hidden from scavenging colleagues, labelled with a scull and a "touch it and die" note. (The latter might not be a good idea if you are subject to safety inspections conducted by people without humor.) Laser diodes have an annoying tendency to die quickly and sometimes like lemmings they hop over the cliff right after one another. Photo-detectors and piezos live longer, when properly wired, but tend to have delivery times of several weeks. Furthermore I highly recommend keeping a *complete* set of drawings, list of parts and notes on changes in one specific place. I spent hours hunting down everything for this collection.

B.2 Photos of Selected Parts and Partial Assemblies

To help with the assembly, several photos of the partially assembled/disassembled AFM are shown here.

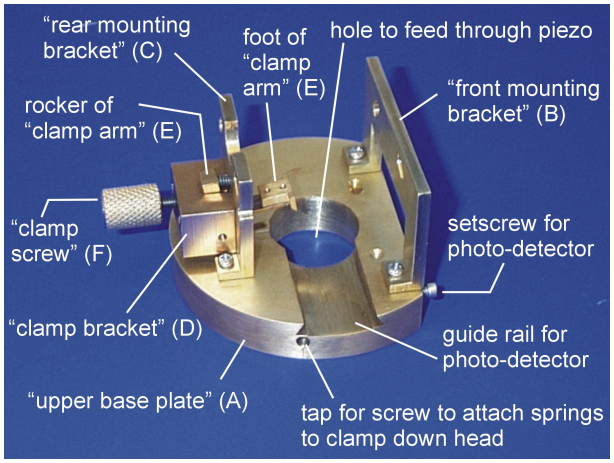

Figure B.1: Partially assembled top part of the AFM head. Letters in brackets correspond to construction drawings.

Note, that in Figure B.1 around the center hole a flat spot, a groove and a hole are machined for the 3 point bearing of the tip holder. The front an rear bracket have not just feed-through holes for the screws to mount the translation stages holding the laser, but extended holes, the one in the front in this picture is at an angle of $\sim 30°$ off the horizontal, the one in the back at $\sim 45°$. These holes allow to change the angle of incidence for the laser off normal, to avoid backscattering into the laser from reflective samples, which would destabilize the laser. On the bottom side of the upper base plate, there is again a flat spot, a groove and a hole which have to be consistent with the positions of the approach screws in the piezo assembly / bottom base plate.

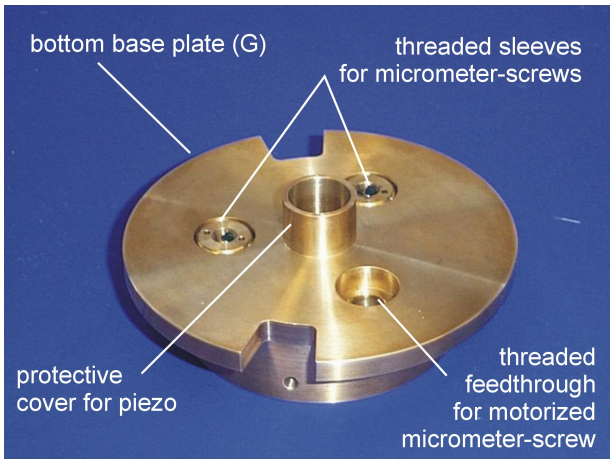

Figure B.2: Detailed view of the bottom base plate, containing already the threaded sleeves for the manual approach screws. The motorized screw is missing. The upper base plate has to fit onto these screw. The center protrusion fits through the center hole of the upper base plate and will enclose the piezo to protect it from mechanical damage.

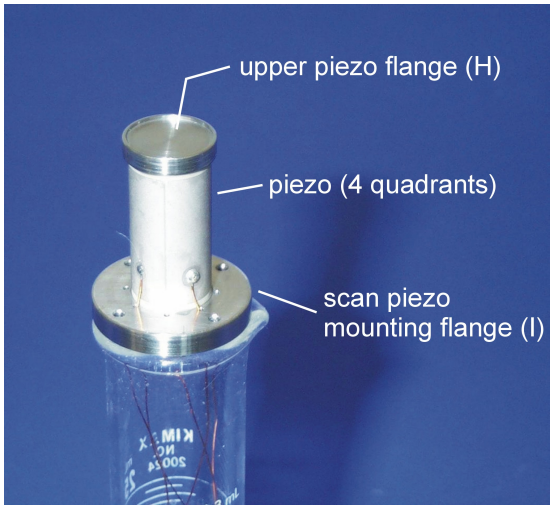

Figure B.3: Piezo with upper flange, bottom mounting flange and attached wires.

The piezo with the upper and bottom flange attached, as shown in Figure B.3, is placed into the bottom base plate from below and held by screws through the bottom mounting flange. This is a simple four quadrant piezo with an inner electrode. To allow more sophisticated movements (e.g. separate electrodes for "offset" and "scan") the electrodes on the outside can be separated by a horizontal gap to yield 8 outer electrodes. Note, the electrodes had to be carefully shaved off on a certain stretch at the top and bottom, to avoid a short via the metallic upper and bottom flanges. Instead of the kepton coated wires (10 mil thick), wires with colorful insulation should be used, to make it easier to discern between the segments and ultimately to avoid frying the piezo.

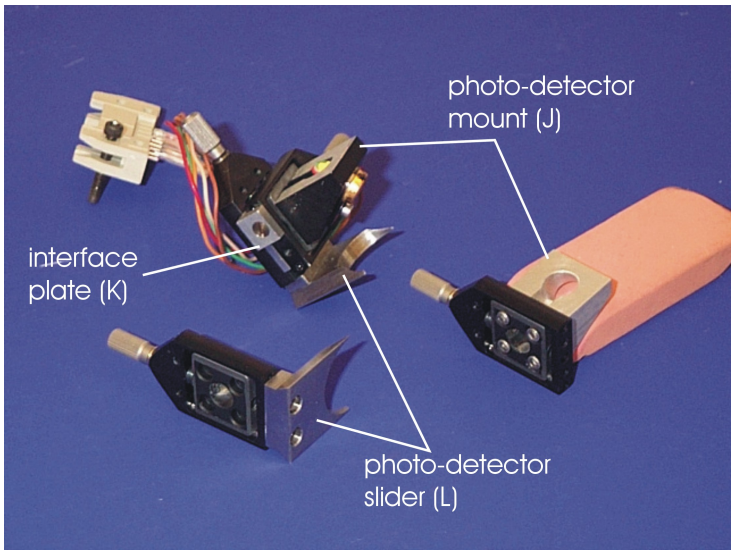

Figure B.4: Assembled and partially disassembled holder of the photo-detector. Shown are 2 sets of parts from different setups. Note that the mounting plate of the photo-detector has a groove from the hole for the detector going to the center hole of the translation stage, through which the wires for the detector will run. Note that for the assembled detector the wires run through an additional hole to the side, not through the translation stages.

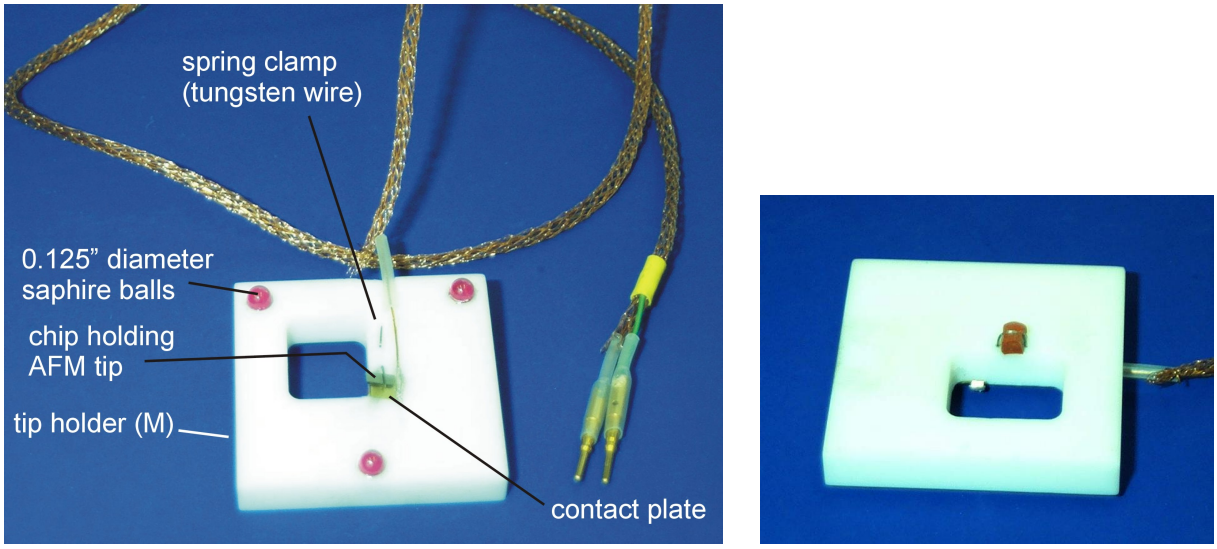

Figure B.5: Tip-holder as seen from above (right) and below (left).

The ball bearings of the tip holder shown in Figure B.5 have to fit the flat spot, groove and hole in the upper base plate, see Figure B.2. A Tungsten wire (10 mil) is bent through the holes and spring loaded with a piece of rubber so the cantilever chip can be spring clamped onto the contact plate (brass). The contact plate allows to apply a voltage to the tip via the attached kepton coated and shielded wire. The shielding is absolutely necessary! Note, there is a piece of tubing placed around the wire across the corner of the tip holder to avoid breaking the wire.

Finally, Figure B.6 shows how the tip holder and detector fit into the assembly. Note, in this photo the laser housing is missing.

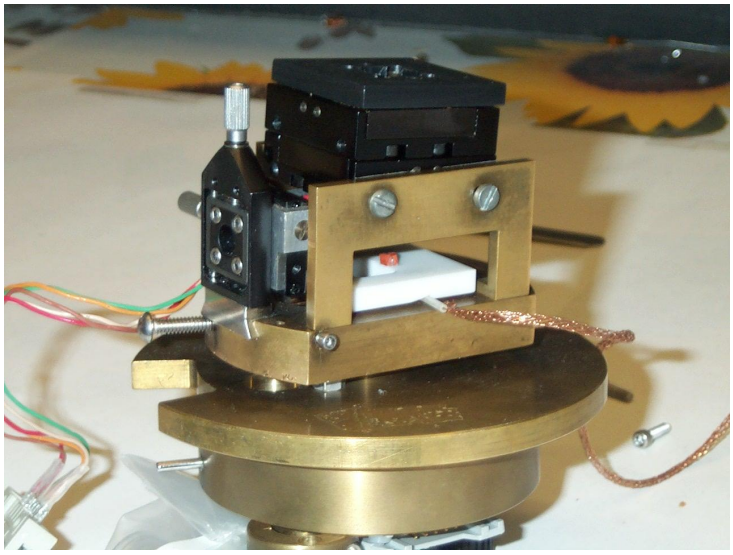

Figure B.6: Partially assembled AFM head.The tip holder is secured by the clamp arm (not visible). The detector slides into the guide rail and is tightened in position with the setscrew. Laser housing and motorized screw are missing in this view. On the left there is the screw and corresponding pin to hold the head on the approach screws with springs.

Table B.1: Conversion of US screw sizes into metric units. For other dimensions please refer to e.g. `ww4.choice.net/~shender4/thread chart.htm`.

screw size	diameter in mm	corresponding metric size
0	1.52	M1 or M1.6
1	1.85	M1.6 or M2
2	2.18	M2
4	2.84	M2.5 or M3
6	3.51	M4

B.3 Construction Drawings

Note, that although the US have officially converted to use metric units, in practice they are only used for drugs. Even a **very** expensive Mars probe was crashed by NASA, because of this issue with pounds and kilograms. Evidently, most of the following drawings are in inch (1 inch = 25.4 mm, 1 mil =1/1000 inch), taps and drills in really funny units. To make things worse, the translation stages have metric taps. To convert the taps to more or less corresponding metric equivalents, please refer to table B.1 I apologize for the mess, but changing it all into metric units would be a great source for hard to detect mistakes.

sample pucks

To mount the samples, one should have a supply of about 5 to 6 sample pucks, i.e. aluminum discs with a diameter of about 0.45 inch and a height of 0.15 inch. On one side a magnetic stainless steel disc is glued on with conductive epoxy, so it can be stuck to the magnet on the piezo. The samples themselves should be mounted on thin plates of stainless steel (diameter 0.5 inch, 0.02 inch thick, supply of $\sim$ 50). The thin plates are mounted with double sided carbon tape on the pucks. Thus the samples can be exchanged and stored on the thin plates, without destroying them. Since the thin plates on top are wider than the main puck, they are easy to grab with tweezers.
To allow for heating/cooling of the sample, a tiny thermoelectric cooling/heating element[3] can be used instead of the regular sample puck. Since these thermoelectric cooling/heating elements are high current devices, it should be enclosed by a horse-shoe shaped macor piece. On top and below thin copper plates should be attached, including a copper braid to a heat sink. An additional piece of magnetic steel is necessary as thermal insulation towards the piezo and to attach the puck to the piezo. Furthermore a temperature sensor (thermocouple wire) should be included towards the sample side. With a cludged prototype (no top copper plate and no insulating enclosure), the sample temperature could be lowered easily by 5° below room temperature.

laser housing

The design of the laser housing has to be changed dramatically from the original one, since nowadays collimation tubes for diode lasers are readily available. To hold the collimation tube in place a simple outer clamping tube should suffice (a rough sketch is given in Figure B.7). To attach the outer clamping tube to the top translation stage, an interface plate is necessary.

[3] 4 x 4 mm, Melcor, Trenton, NJ, USA. www.melcor.com or Ferrotec America Co., Nashua, NH, USA. www.ferrotec-america.com

Furthermore it is recommended to glue a short cylinder with small holes or notches and with the same inner and outer diameter onto the mount holding the collimation lens (see Figure B.7, "focusing ring"). Subsequently, the cutout at the bottom of the clamping tube allows to reach in with tweezers to adjust the focus of the laser *in situ*!

Additional tip holder

The cantilever holder shown in Figure B.24 can be improved to be used for regular contact AFM, tapping mode AFM and SPFM without changing the tip holder: By making the depression for the contact plate bigger and deeper, it can accommodate a piezo to vibrate the tip in addition to the contact plate (with an insulating layer in between). Furthermore holes to allow for cables contacting that piezo are necessary.

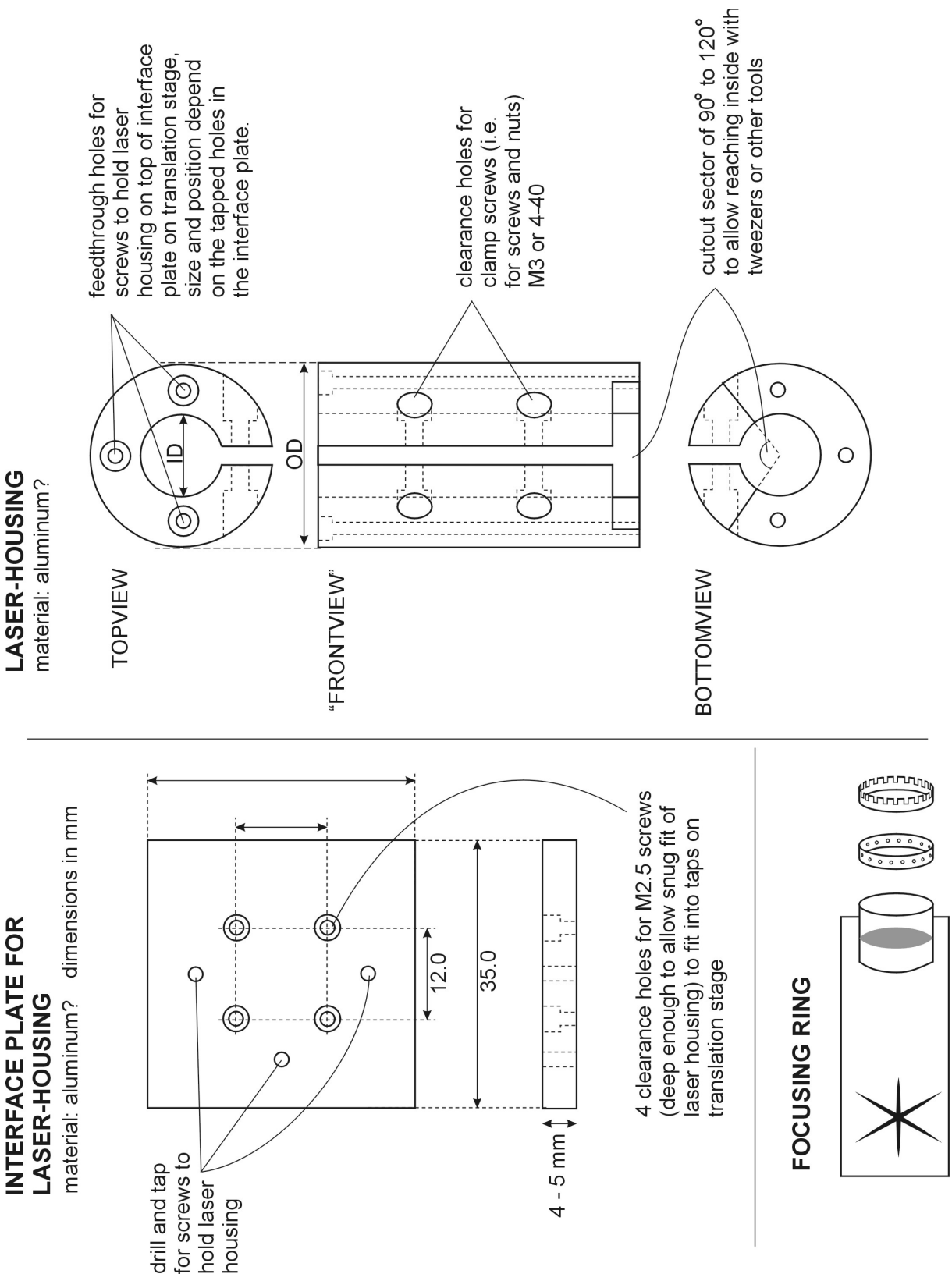

Figure B.7: Sketch of a possible housing for a diode laser collimation tube and an interface plate to mount the laser on top of the translation stages. The inner diameter (ID) and outer diameter(OD) have to be chosen in a way to fit the screws and to allow a secure clamping of the collimation tube (outer dia. 14.7 mm.

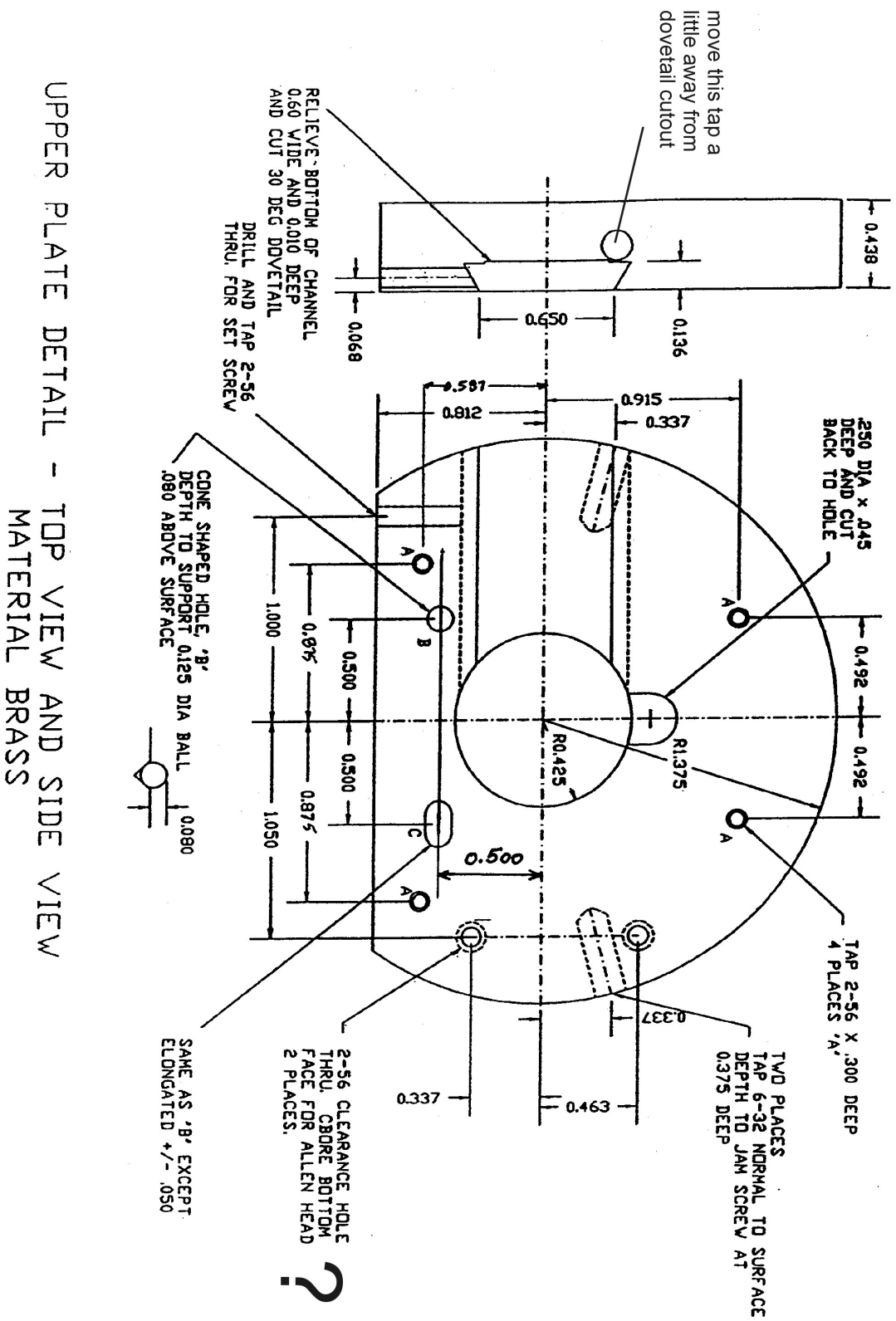

Figure B.8: Top view of upper base plate, i.e. part number (10) in Figure 2.1 and number (A) in Figure B.1. The clearance holes marked by "?" Do not serve any known purpose and can be left out.

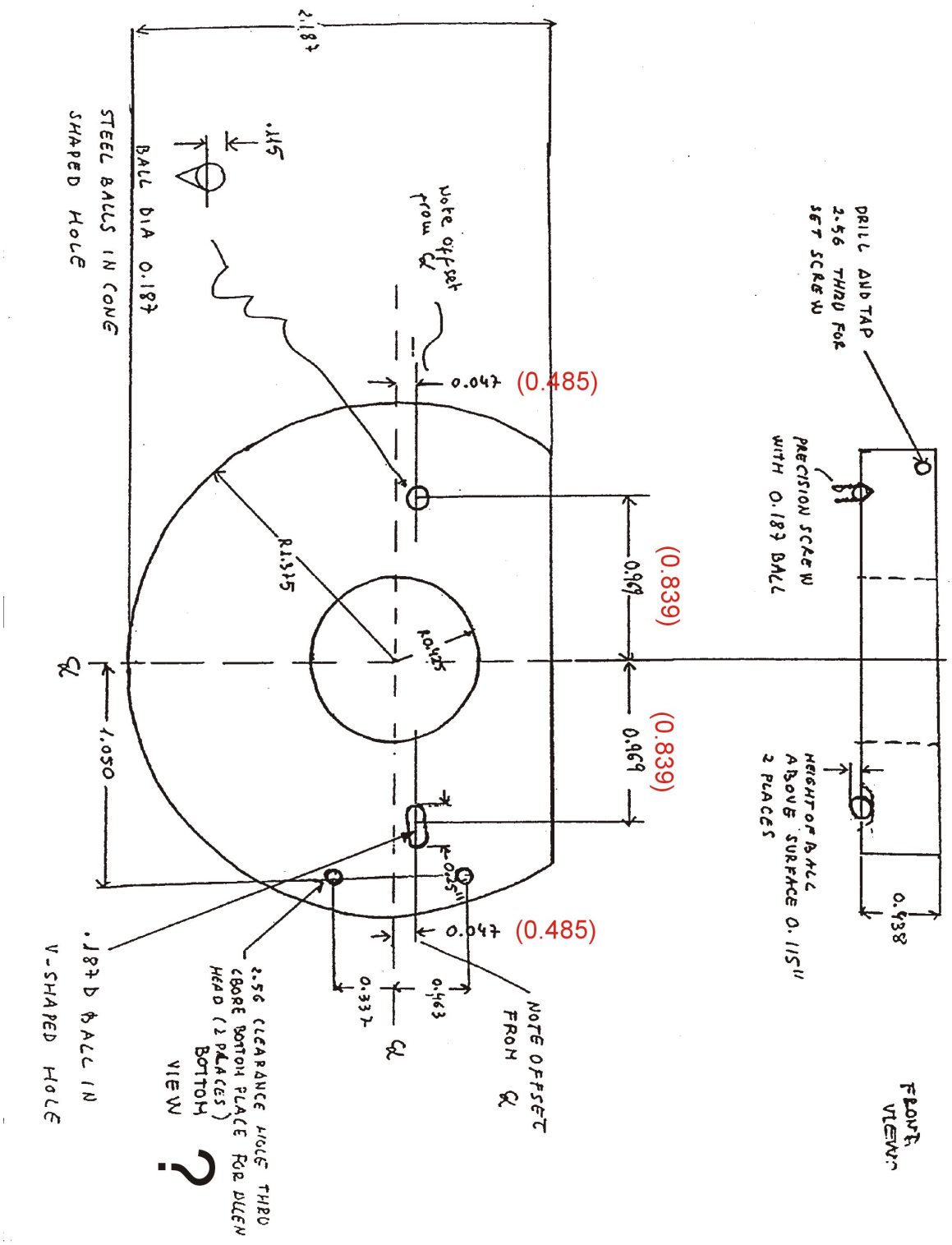

Figure B.9: Bottom view of upper base plate, i.e. part number (10) in Figure 2.1 and number (A) in Figure B.1. The clearance holes marked by "?" Do not serve any known purpose and can be left out. Numbers in brackets correspond to a different arrangement of the approach screws, which allows for a slower approach. Note that the position of the groove and hole have to coincide with the position of the approach screws, see drawing B.17.

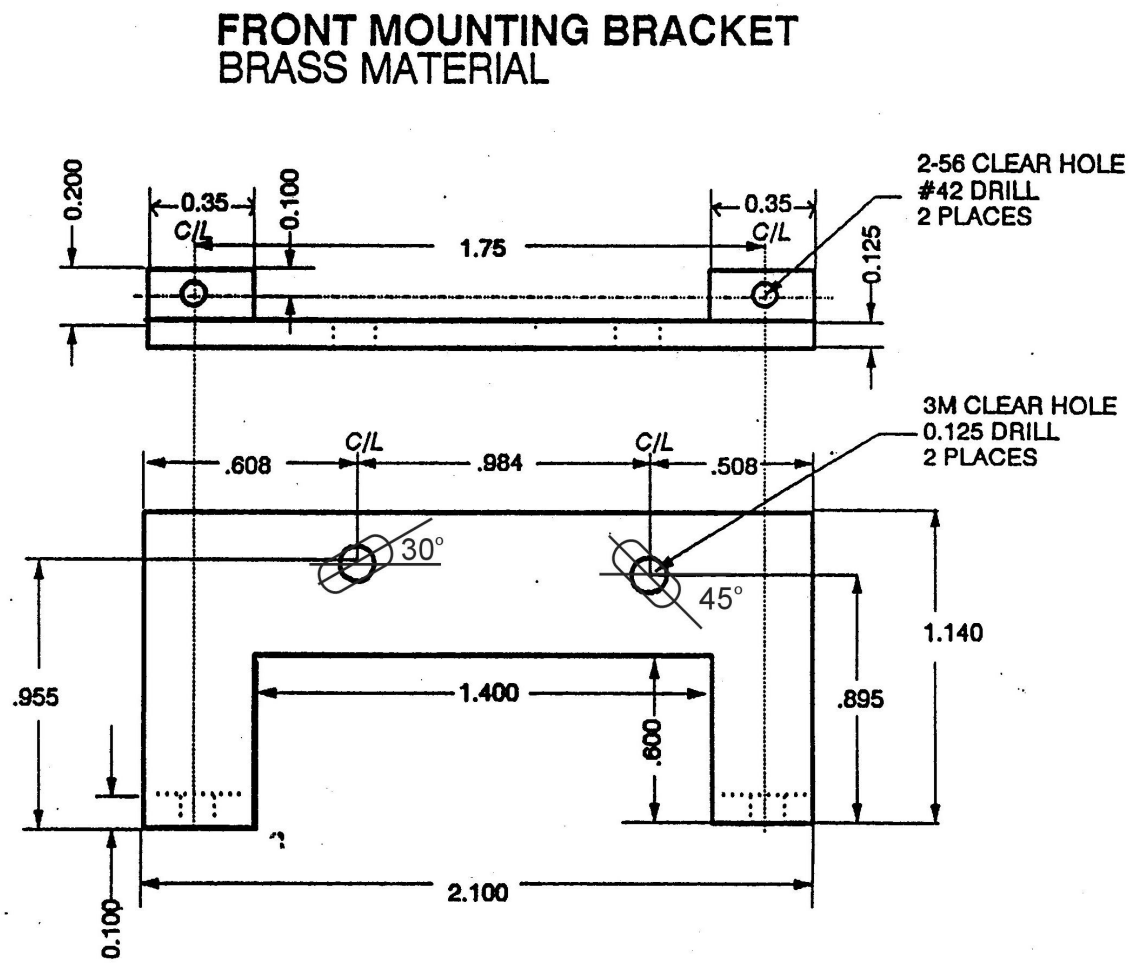

Figure B.10: Front mounting bracket, number (B) in Figure B.1. The clearance holes for the translation stages are extended by ± half the diameter of the hole at angles of 30° and 45°, respectively, to allow mounting the stages at a slight angle (5 - 10 degrees off the horizontal), so the light of the laser does not shine perpendicular onto the sample. This avoids backscattering from reflective samples into the laser diode, which would destabilize the laser.

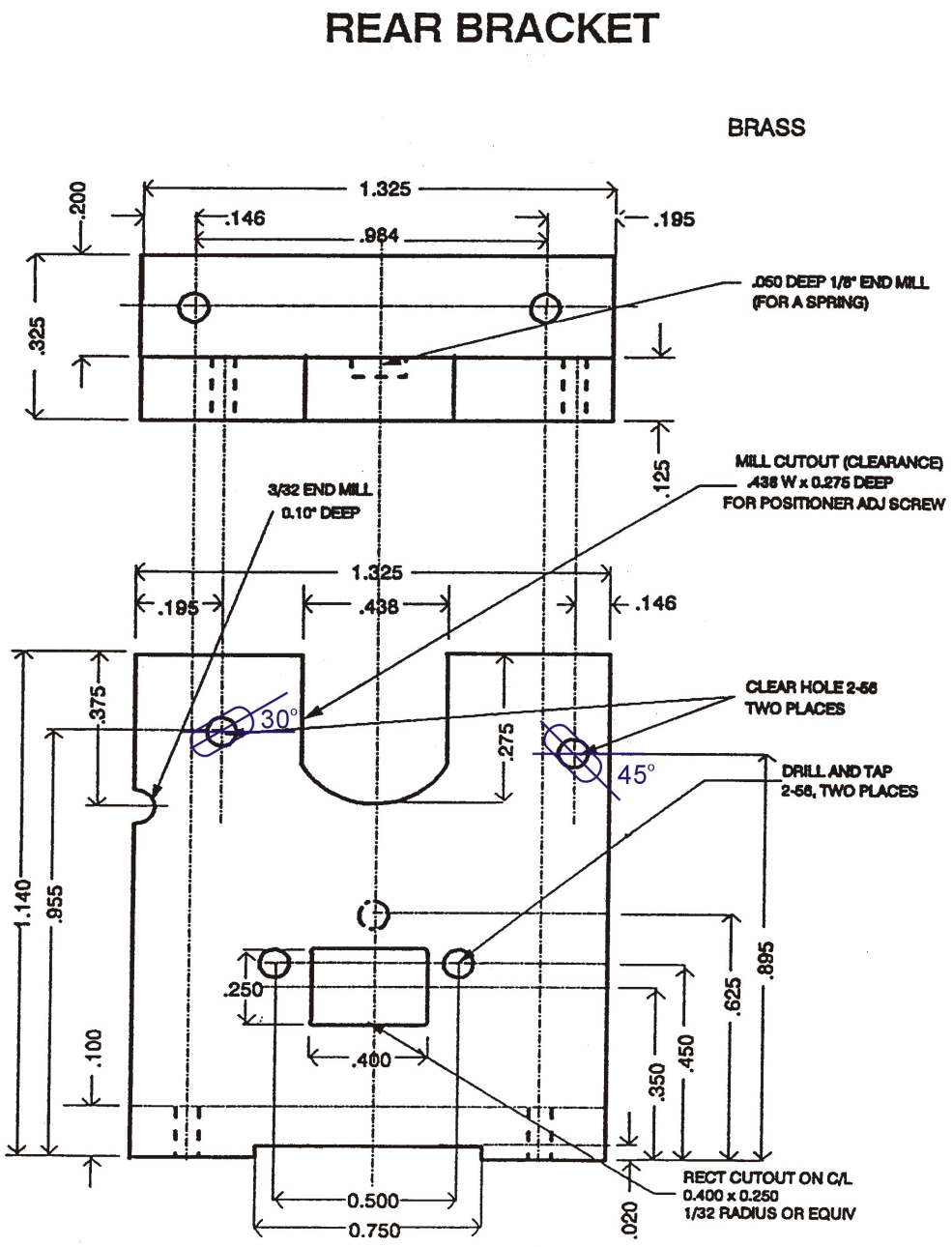

Figure B.11: Rear mounting bracket, number (C) in Figure B.1. The clearance holes for the translation stages are at angles of 30° and 45°, respectively, as explained for Drawing B.10.

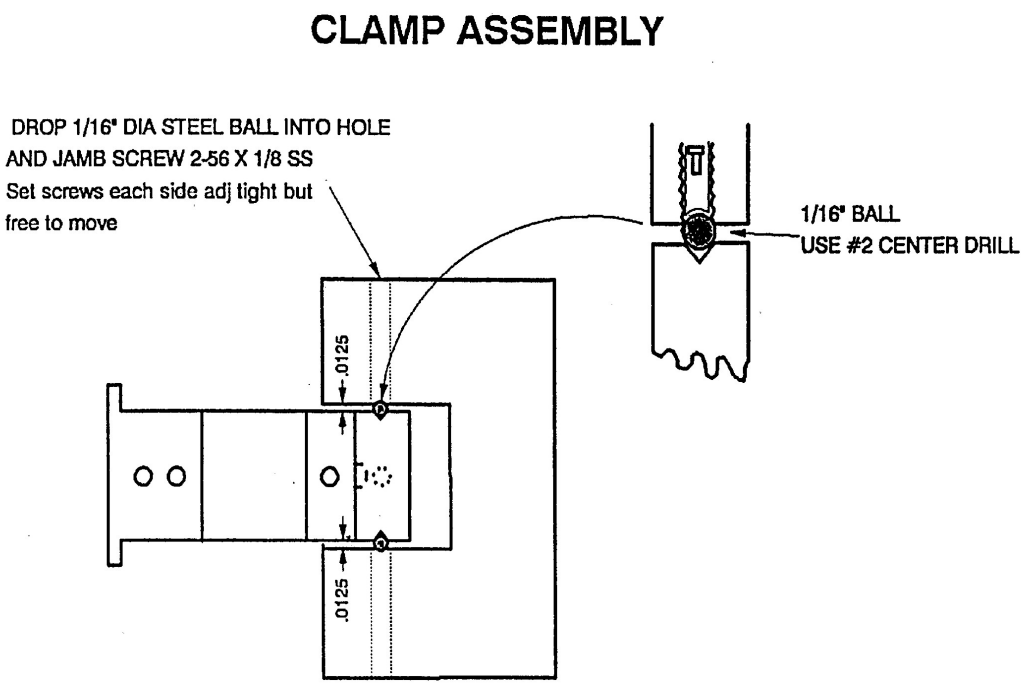

Figure B.12: This drawing of the clamp assembly shows how the clamp arm is suspended by two stainless steel balls inside the clamp bracket, to allow for a smooth operation of the clamp arm.

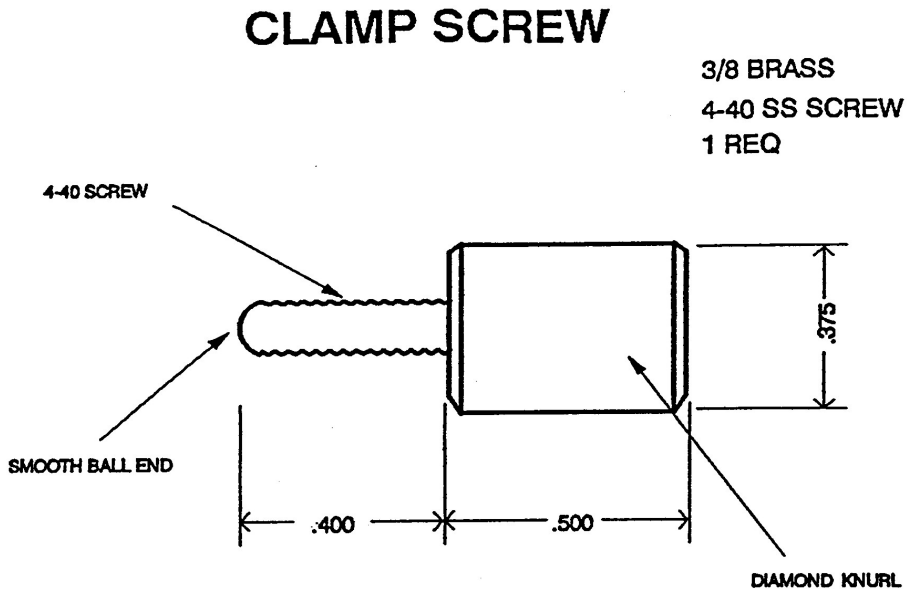

Figure B.13: Clamp screw, number (F) in Figure B.1.

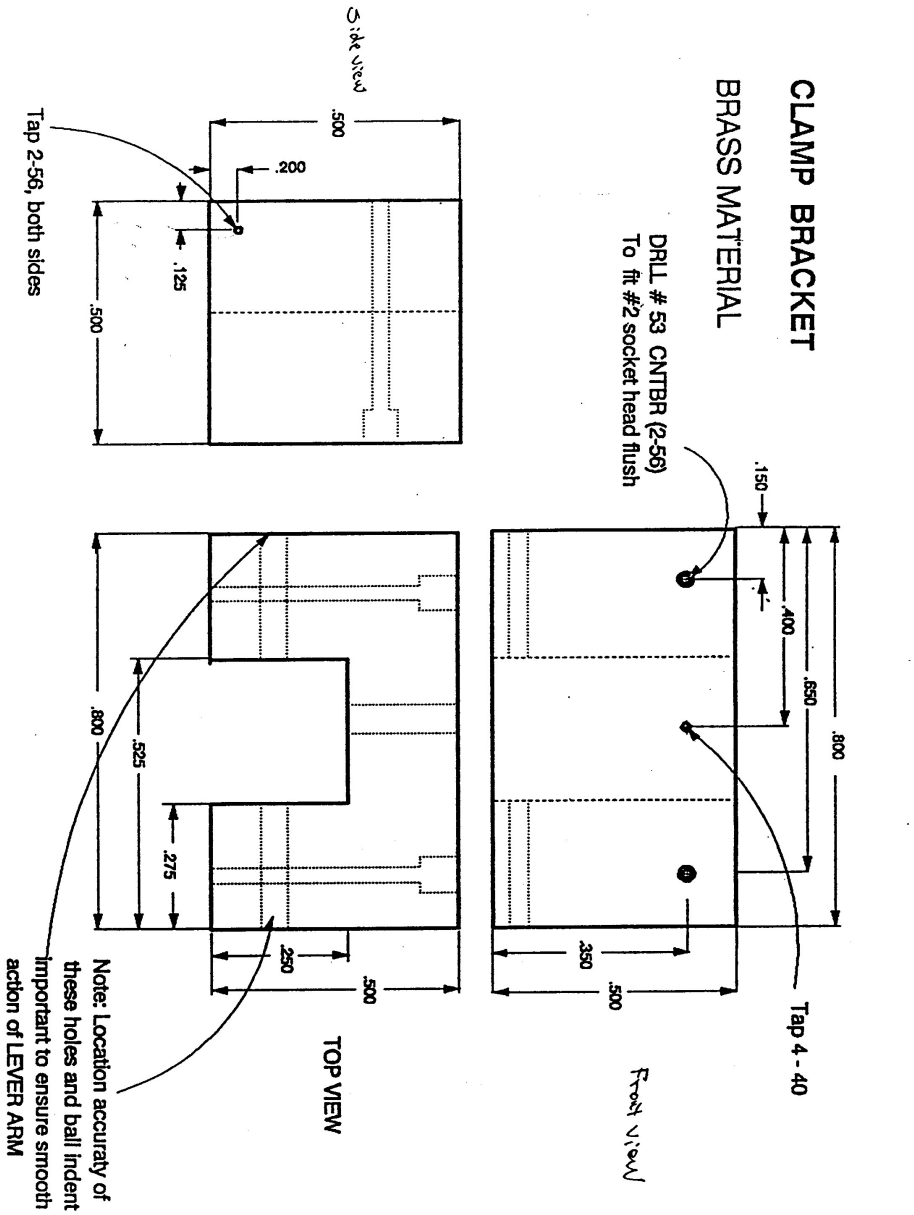

Figure B.14: Clamp bracket, number (D) in Figure B.1. The clamp bracket holds the clamp arm, and via the clamp screw allows to move the arm up and down to clamp down the tip holder.

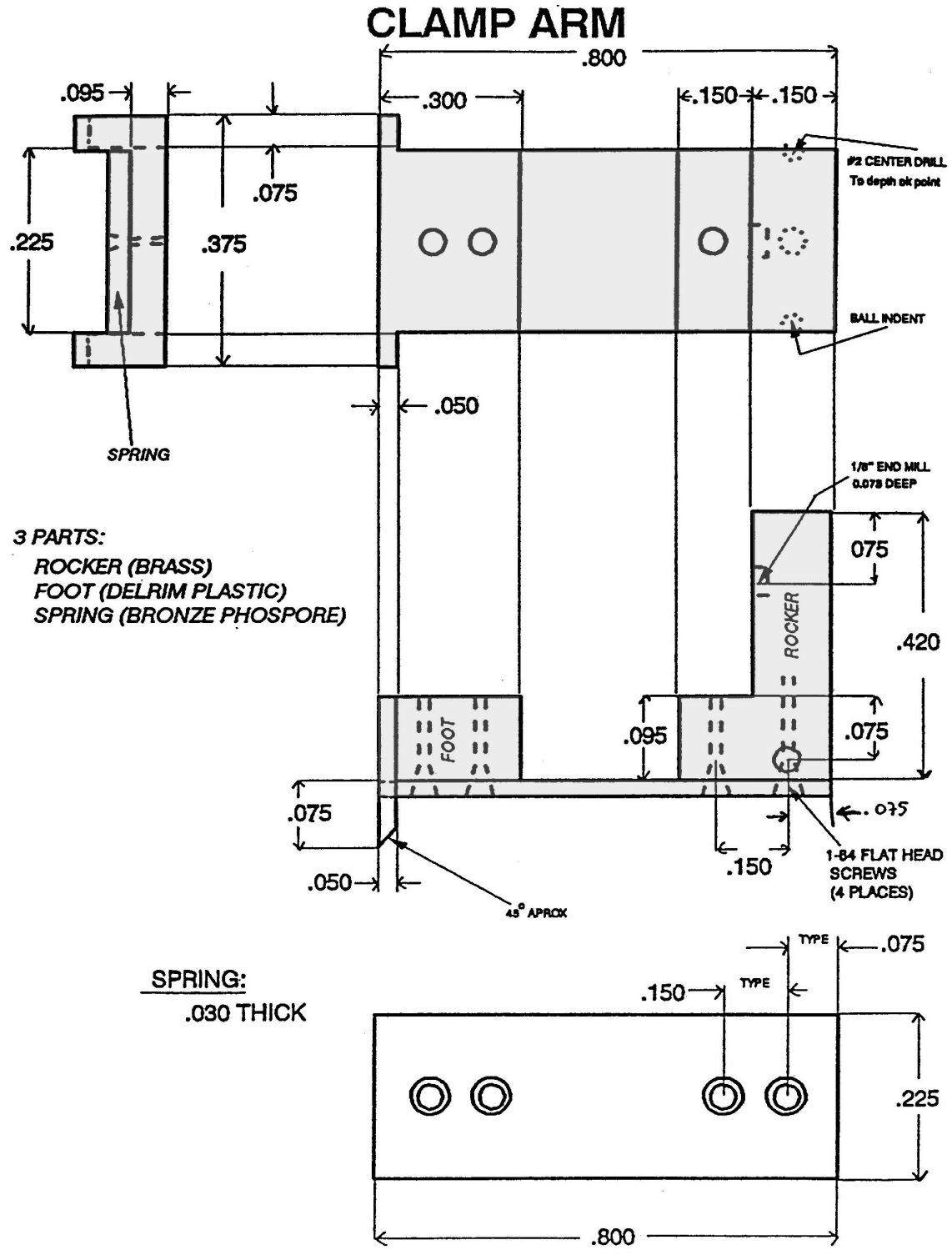

Figure B.15: Clamp arm, number (E) in Figure B.1. Note, these are actually three pieces in one drawing: rocker, spring and foot are shown screwed together. The foot can be made of brass instead of delrin, when a piece of rubber is placed between the foot and the tip holder.

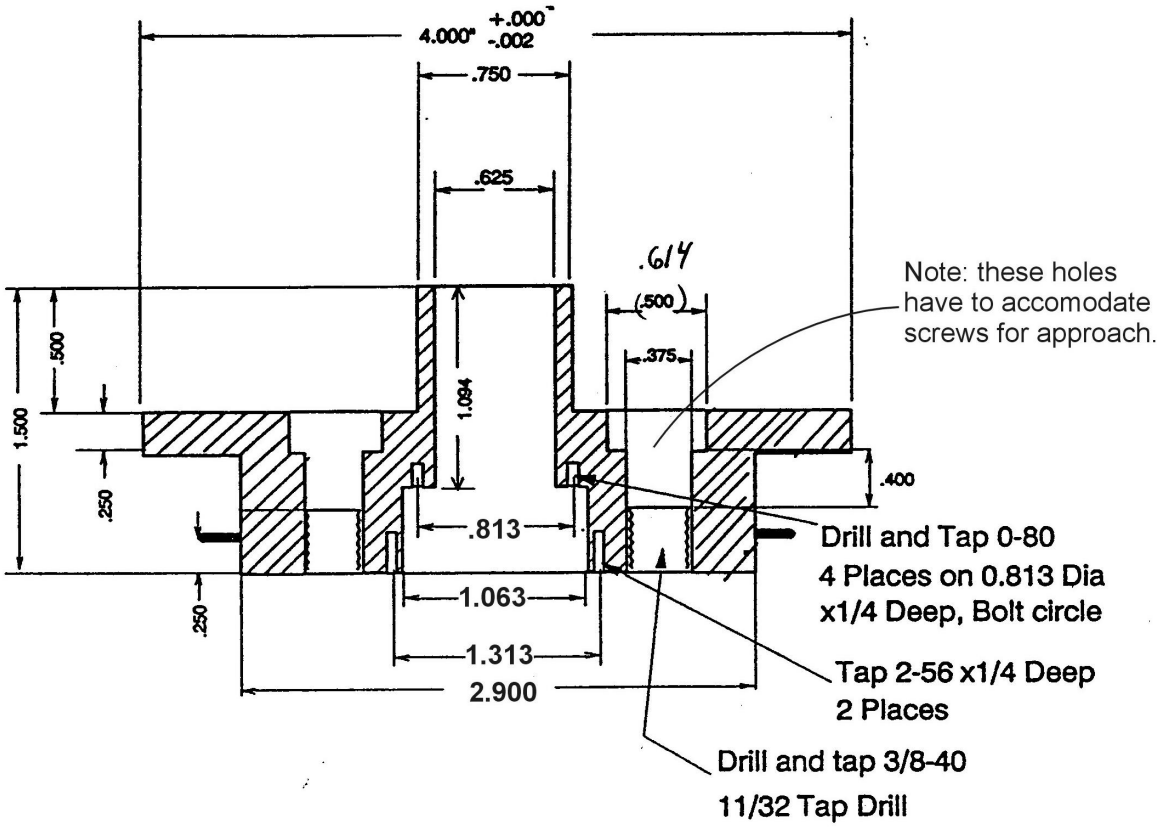

Figure B.16: Bottom base plate, number (G) in Figure B.2, side view. Note, that the diameter of the holes for the sleeves of the approach screws had to be adjusted for the screws given in the part list. If you use metric screws, you have to adjust the numbers accordingly.

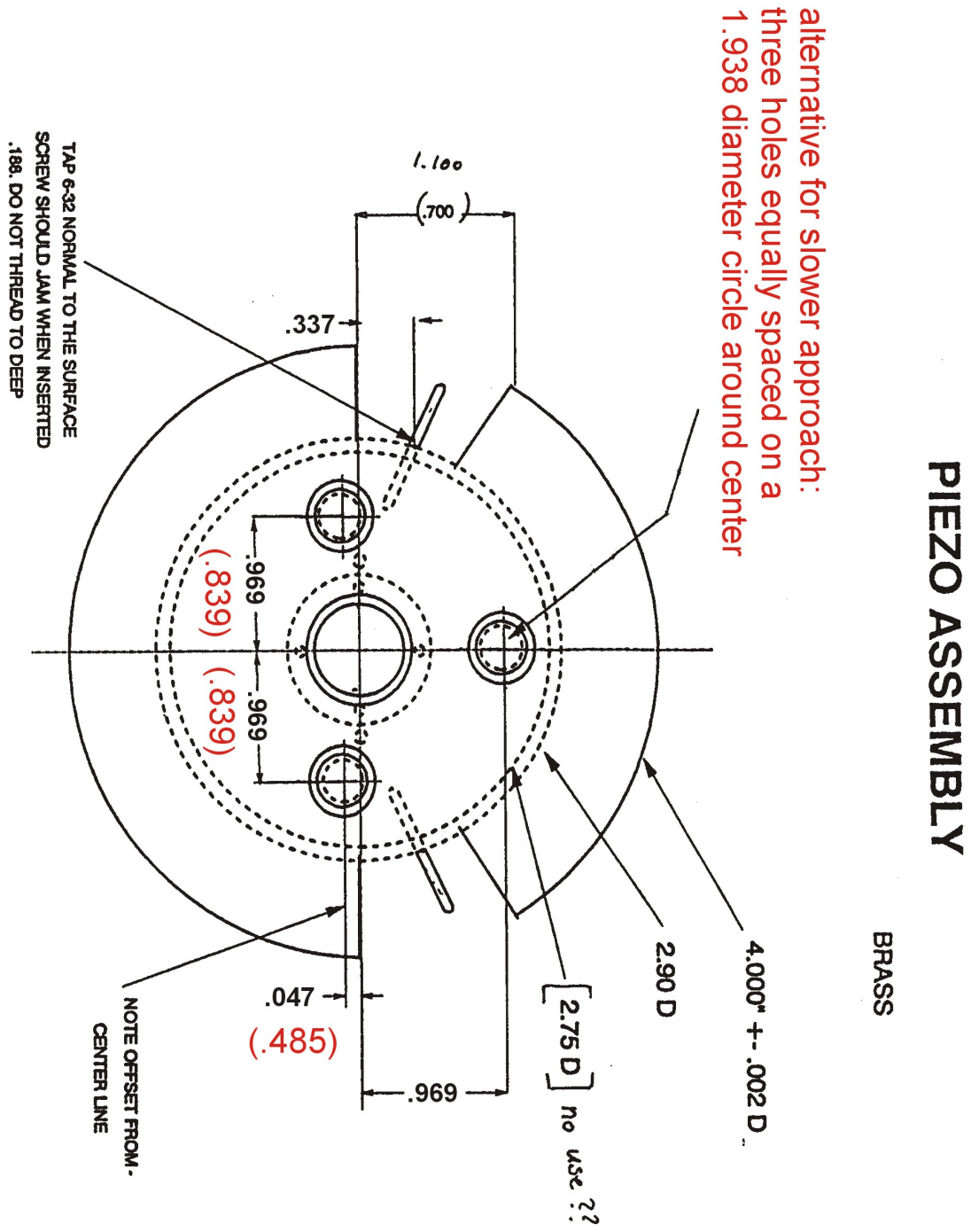

Figure B.17: Bottom base plate, number (G) in Figure B.2, top view. Note, that the numbers in brackets correspond to an alternative arrangement of the approach screws, allowing for a slower approach. If this alternative is chosen, the position of the groove and hole on the bottom of the upper base plate have to be adjusted accordingly, see drawing B.9.

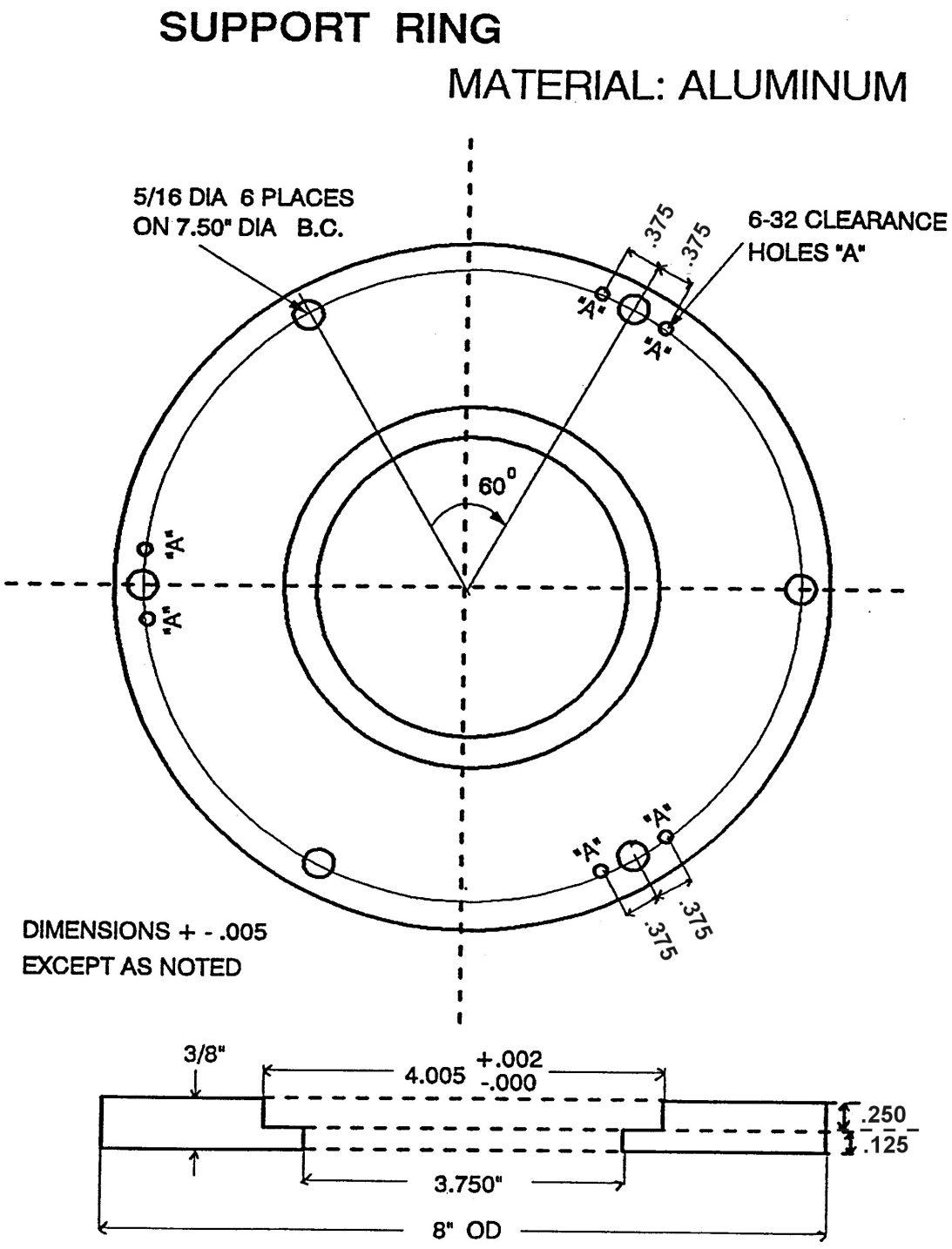

Figure B.18: Support Ring, in which the Bottom Base Plate sits. The holes are intended to attach the suspension, i.e. the rubber tubing.

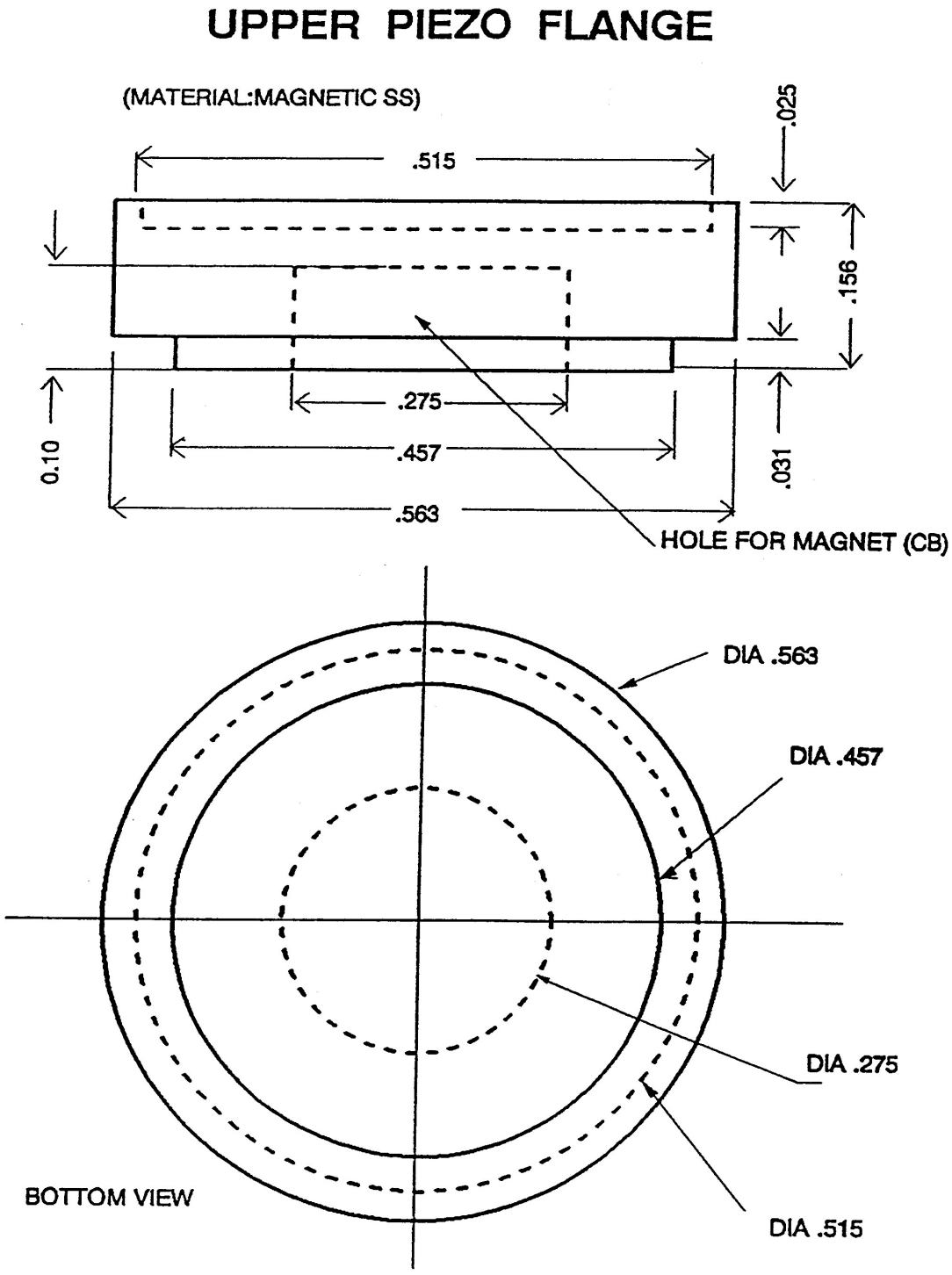

Figure B.19: Upper piezo flange, number (H) in Figure B.3. This plate closes the piezo at the top and supports the sample. Note, that the magnet has to be glued into the plate with conductive epoxy and that is has to be connected to ground. By doing so the sample is grounded (more or less). If this is piece is not grounded, the feedback will behave like a bucking bronco, but not do what it is supposed to.

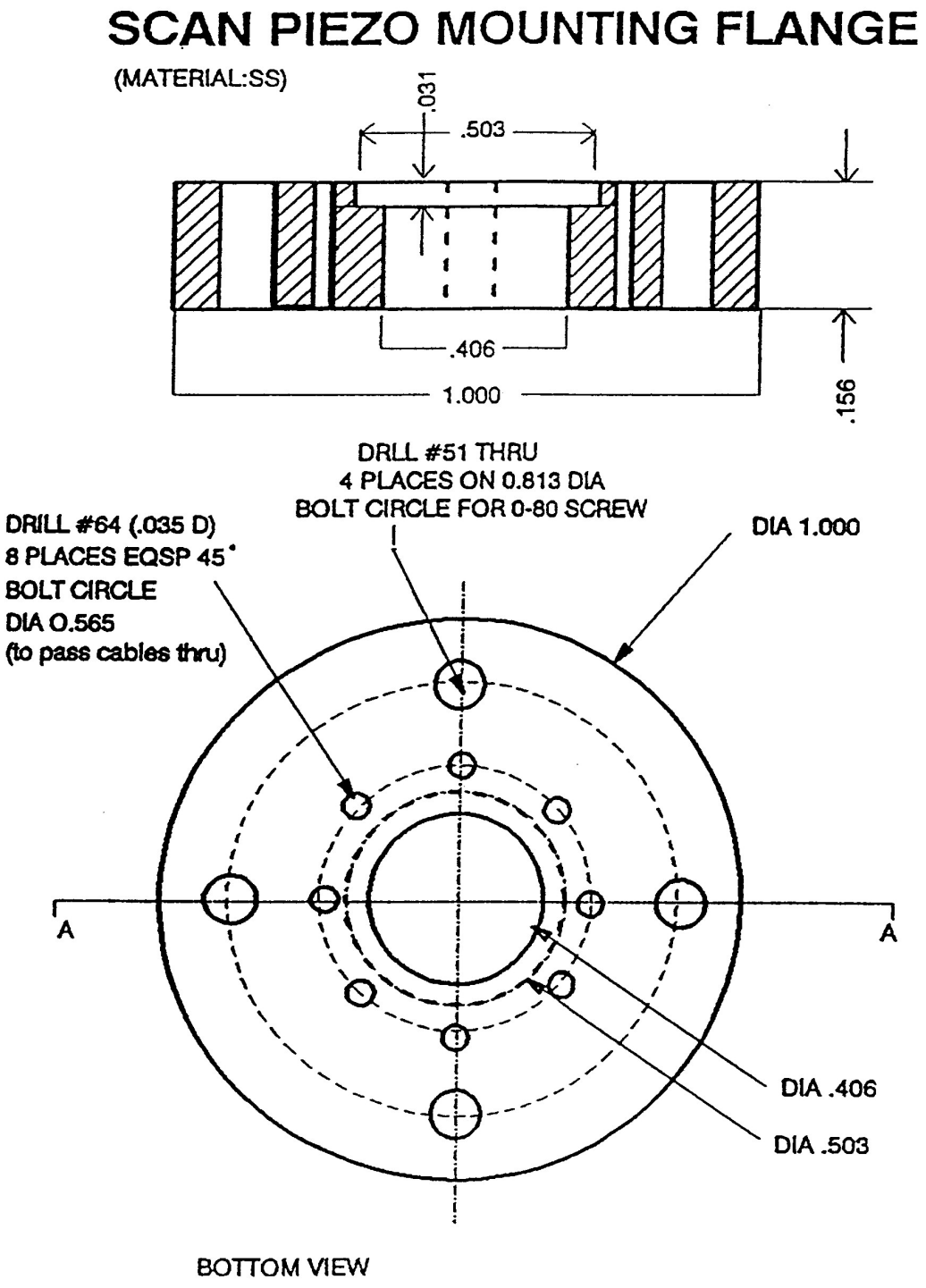

Figure B.20: Scan piezo mounting (bottom) flange, number (I) in Figure B.3. This is the base plate for the piezo, which is epoxied on top of it. This flange is screwed into the bottom base plate.

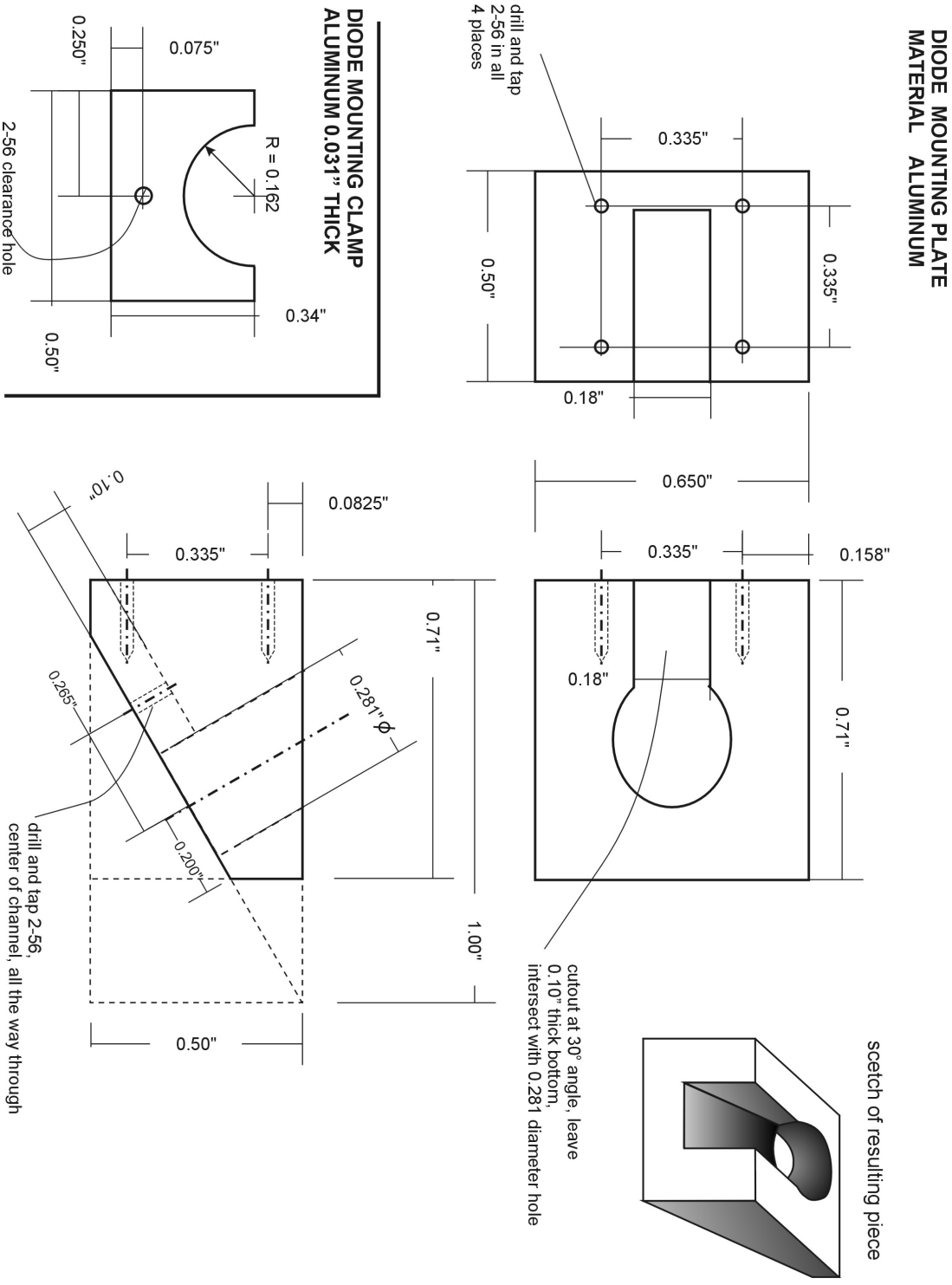

Figure B.21: Photo-detector mounting plate, number (J) in Figure B.4. The photo-detector is clamped into the hole, wire are run through the groove.

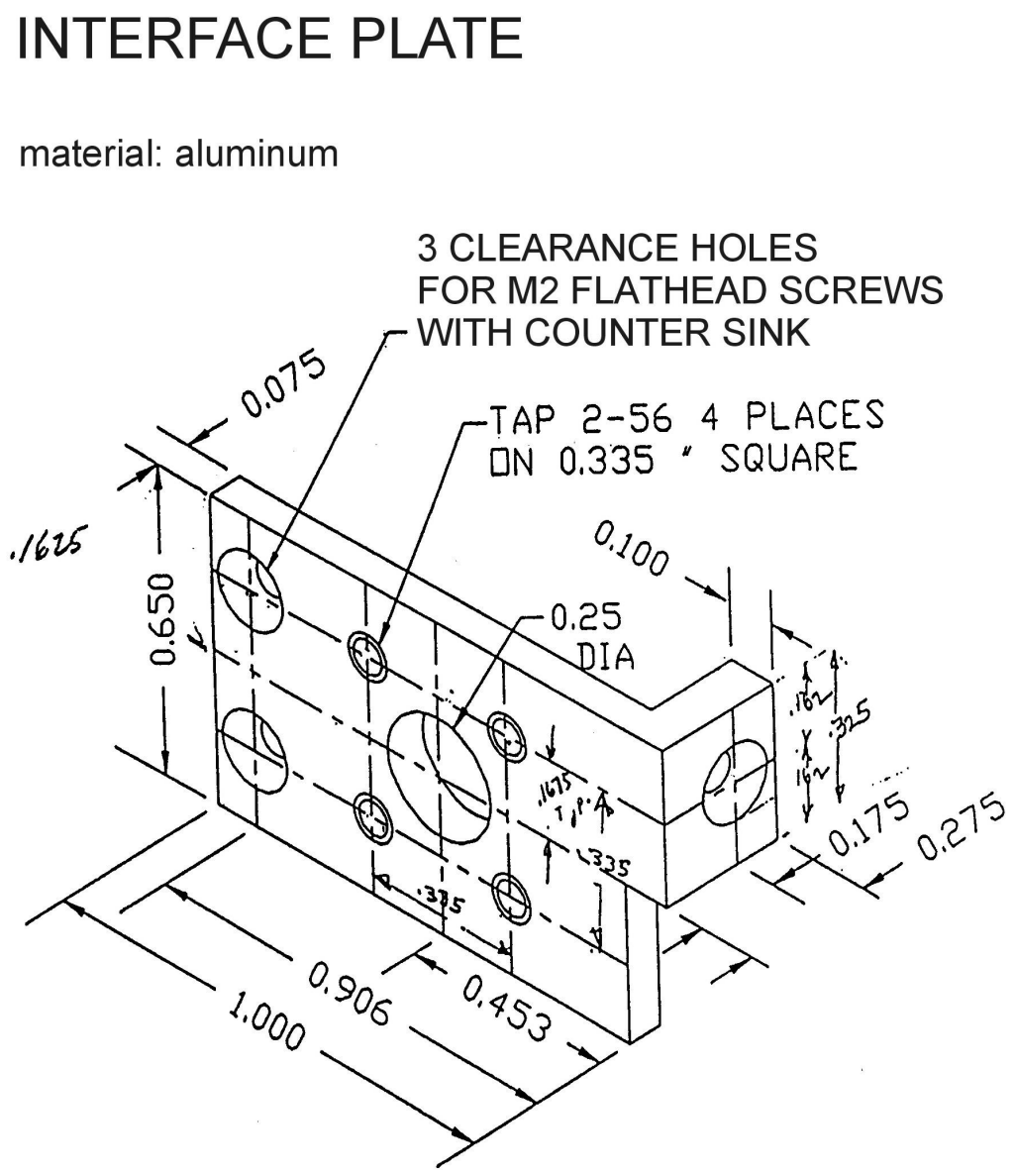

Figure B.22: Interface plate for detector translation stages, number (K) in Figure B.4. This plate allows to built a cross-axis translator out of the two miniature translation stages.

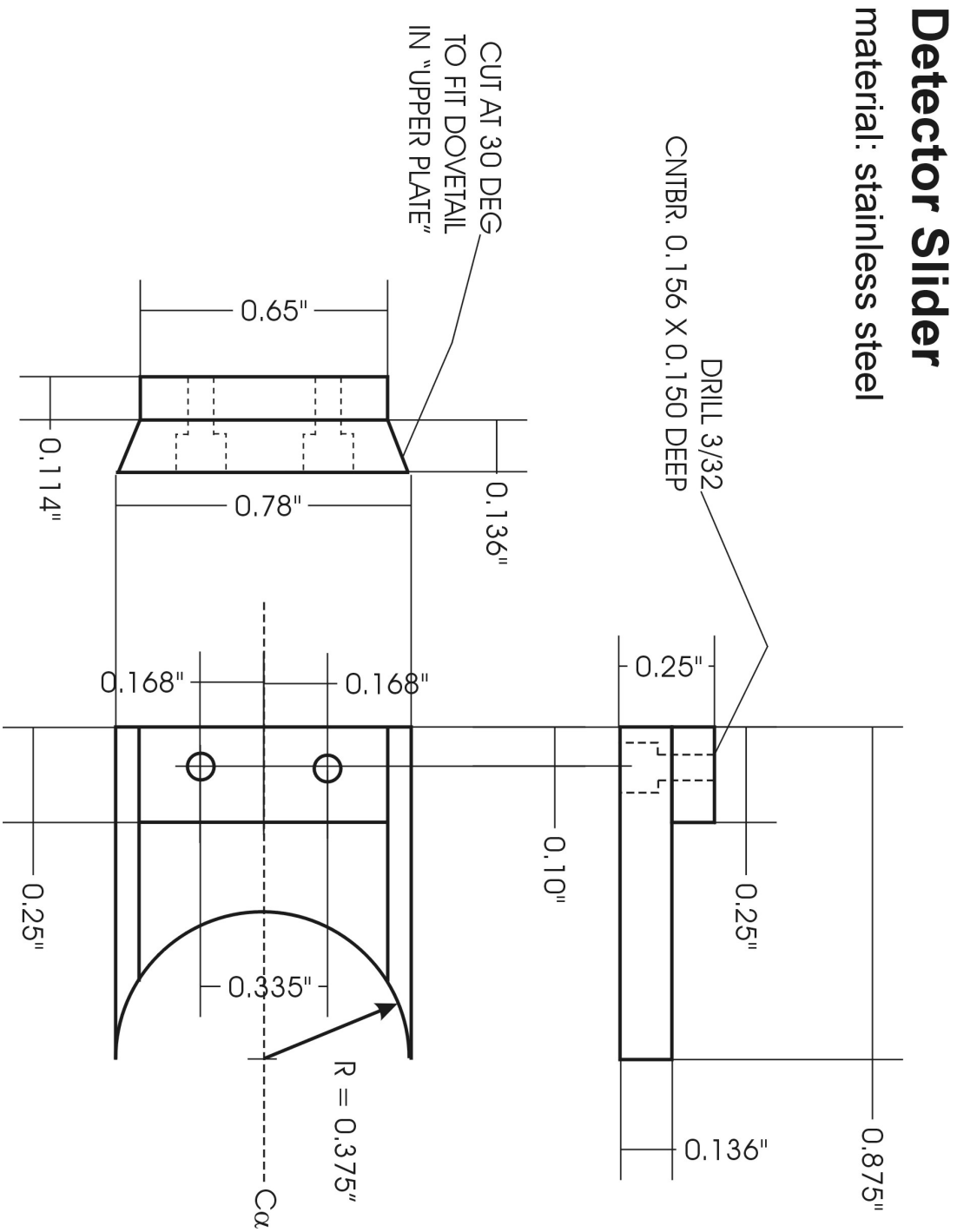

Figure B.23: Photo-detector sliding base plate, number (L) in Figure B.4. This slider has to fit into the dovetail groove in the bottom base plate.

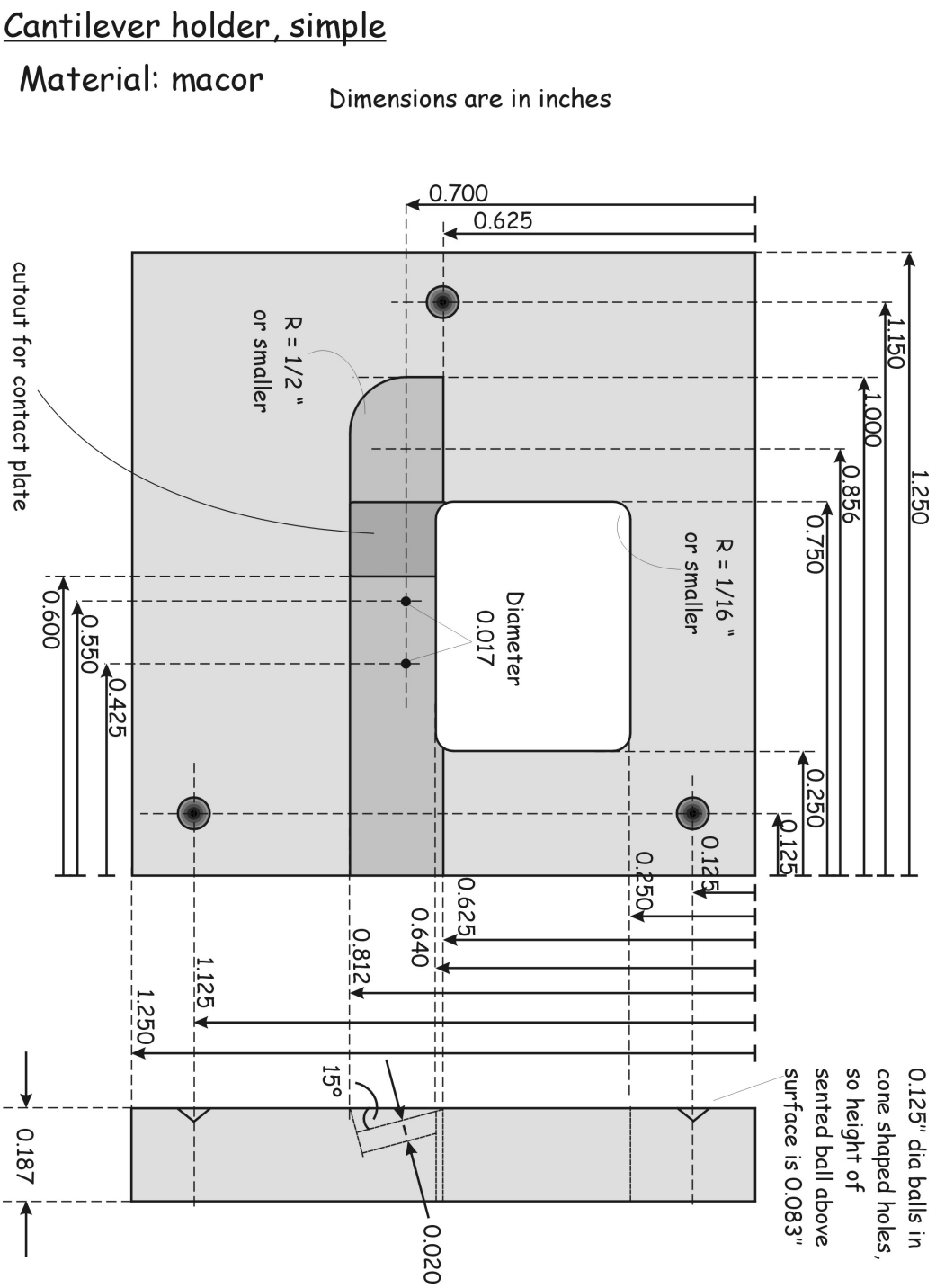

Figure B.24: Simple cantilever holder with a depression for contact plate, as shown in Figure B.5. It is advantageous to apply a voltage only to the tip. If the whole cantilever holder were conductive, separated via insulating ball bearings from the upper base plate, the two metal plates would form a huge capacitor, possibly interfering with the actual measurement. This holder can be improved to be used for regular contact AFM, tapping mode AFM and SPFM without changing the tip holder.

Bibliography

[1] J. Fritz, M. K. Baller, H. P. Lang, H. Rothuizen, P. Vettiger, E. Meyer, H.-J. Güntherodt, Ch. Gerber and J. K. Gimzewski, *Translating Biomolecular Recognition into Nanomechanics*, Science, **288**, 316 (2000).

[2] P. Vetttiger, M. Despont, U. Drechsler, U. Durig, W. Haberle, M. I. Lutwyche, H. E. Rothuzien, R. Stutz, R. Widmer, G. K. Binnig, *The "Millipede" - More Than One Thousand Tips for Future AFM Data Storage*, IBM J. Res. Dev., **44**, 323 (2000); or U. Duriga, G. Cross, M. Despont, U. Drechsler, W. Haberle, M. I. Lutwyche, H. E. Rothuzien, R. Stutz, R. Widmer, P. Vetttiger, G. K. Binnig, W. P. King, K. E. Goodson, *"Millipede" - an AFM Data Storage System at the Frontier of Nanotribology*, Tribol. Lett., **9**, 25 (2000); or M. I. Lutwyche, M. Despont, U. Drechsler, U. Durig, W. Haberle, H. E. Rothuzien, R. Stutz, R. Widmer, G. K. Binnig, P. Vetttiger, *Highly Parallel Data Storage System Based on Scanning Probe Arrays*, Appl. Phys. Lett., **77**, 3299 (2000).

[3] U. Srinivasan, M. R. Houston, R. T. Howe, R. Maboudian, *Alkyltrichlorosilane-Based Self-Assembled Monolayer Films for Stiction Reduction in Silicon Micromachines*, J. Microelectromechanical Systems, IEEE **7**, 252 (1998).

[4] M. Salmeron, *Observing Friction at Work*, Chemtech., **28**, 17 (1998).

[5] R. W. Carpick and M. Salmeron, *Scratching the Surface: Fundamental Investigations of Tribology with Atomic Force Microscopy*, Chem. Rev., **97**, 1163 (1997).

[6] B. N. J. Persson, *Sliding Friction* (Springer-Verlag, Berlin, 1998).

[7] P. B. Merrill and S. S. Perry, *Fundamental Measurements of the Friction of Clean and Oxygen-Covered VC(100) with Ultrahigh Vacuum Atomic Force Microscopy: Evidence for Electronic Contributions to Interfacial Friction*, Surf. Sci., **418**, 342 (1998).

[8] A. Dayo, W. Alnasrallah and J. Krim, *Superconductivity-Dependent Sliding Friction* Phys. Rev. Lett., **80**, 1690 (1998).

[9] M. S. Tomasone, J. B. Sokoloff, A. Widom and J. Krim, *Dominance of Phonon Friction for a Xenon Film on a Silver (111) Surface*, Phys. Rev. Lett., **79**, 4798 (1997).

[10] U. Landman, W. D. Luedtke and J. Gao, *Atomic-Scale Issues in Tribology: Interfacial Junctions and Nano-Elastohydrodynamics*, Langmuir, **12**, 4514 (1996).

[11] S. P. Lewis, M. V. Pykhtin, E. J. Mele and A. M. Rappe, *Continuum Elastic Theory of Adsorbate Vibrational Relaxation*, J. Chem. Phys., **108**, 1157 (1998).

[12] D. Fuhrmann and Ch. Wöll, *The Microscopic Origins of Sliding Friction: A Spectroscopic Approach* New Journal of Physics, **1**, 1.1 (1998), http://www.njp.org/.

[13] A. Lio, D. H. Charych and M. Salmeron, *Comparative Atomic Force Microscopy Study of the Chain Length Dependence of Frictional Properties of Alkanethiols on Gold and Alkylsilanes on Mica* J. Phys. Chem. B, **101**, 3800 (1997).

[14] X.-d. Xiao, J. Hu, D. H. Charych and M. Salmeron, *Chain Length Dependence of the Fricitonal Properties of Alkylsilane Molecules Self-Assembled on Mica Studied by Atomic Force Microscopy*, Langmuir, **12**, 235 (1996).

[15] R. C. Thomas, J. E. Houston, T. A. Michalske and R. M. Crooks, *The Mechanical Response of Gold Substrates Passivated by Self-Assembling Monolayer Films*, Science **259**, 1883 (1993).

[16] A. B. Tutein, S. J. Stuart and J. A. Harrison, *Role of Defects in Compression and Friction of Anchored Hydrocarbon Chains on Diamond*, Langmuir, **16**, 291 (2000).

[17] R. W. Carpick, Q. Dai, D. F. Ogletree and M. Salmeron, *Friction Force Microscopy Investigation of Potassium Halide Surfaces in Ultrahigh Vacuum: Structure, Friction and Surface Modification*, Tribol. Lett., **5**, 91 (1998).

[18] A. L. Shluger, R. T. Williams and A. L. Rohl, *Lateral and Friction Forces Originating During Force Microscope Scanning of Ionic Surfaces* Surf. Sci., **343**, 273 (1995).

[19] M. R. Sørensen, K. W. Jacobsen and P. Stoltze, *Simulation of Atomic-Scale Sliding Friction*, Phys. Rev. B, **53**, 2101 (1996);

[20] U. Landman and W. D. Luedtke,*Scanning tunneling microscopy III: Theory of STM and related scanning probe methods*, R. Wiesendanger, H.-J. Guentherodt, eds., (Springer Verlag, Berlin, 1993), p 207.

[21] J. N. Israelachvili, *Intermolecular and Surface Forces* (Academic Press, London, 1985)

[22] A. Widom and J. Krim, *Q Factors of Quartz Oscillator Modes as a Probe of Submonolayer-Film Dynamics*, Phys. Rev. B, **34**, 1403 (1986); J. Krim and A. Widom, *Damping of a Crystal Oscillator by an Adsorbed Monolayer and its Relation to Interfacial Viscosity* Phys. Rev. B, **38**, 12184 (1988).

[23] A. R. Burns, J. E. Houston, R. W. Carpick and T. A. Michalske, *Friction and Molecular Deformation in the Tensile Regime*, Phys. Rev. Lett., **82**, 1181 (1999). S. A. Joyce and J. E. Houston, *A New Force Sensor Incorporating Force-Feedback Control for Interfacial Force Microscopy*, Rev. Sci. Instrum. **62**, 710 (1991).

[24] G. Binnig, C. F. Quate and C. Gerber, *Atomic Force Microscope*, Phys. Rev. Lett., **56**, 930 (1986).

[25] S. Alexander, L. Hellemans, O. Marti, J. Schneir, V. Elings, P. K. Hansma, M. Longmire and J. Gurley, *An Atomic-Resolution Atomic-Force Microscope Implemented Using an Optical Lever*, J. Appl. Phys., **65**, 164 (1989); G. Meyer and N. M. Amer, *Optical-Beam-Deflection Atomic Force Microscopy: The NaCl (001) Surface*, Appl. Phys. Lett., **56**, 2100 (1990); O. Marti, J. Colchero and J. Mlynek, *Combined Scanning Force and Friction Force Microscopy on Mica*, Nanotechnology, **1**, 141 (1990).

[26] R. W. Carpick, N. Agraït, D. F. Ogletree and M. Salmeron, *Measurements of Interfacial Shear (Friction) with an Ultrahigh Vacuum Atomic Force Microscope*, J. Vac. Sci. Technol. B, **14**, 1289 (1996).

[27] E. Gnecco, R. Bennewitz, T. Gyalog, Ch. Loppacher, M. Bammerlin, E. Meyer and H.-J. Güntherodt, *Velocity Dependence of Atomic Friction*, Phys. Rev. Lett., **84**, 1172 (2000).

[28] T. Strunz, K. Oroszlan, R. Schäfer and H.-J. Güntherodt, *Dynamic Force Spectroscopy of Single DNA Molecules*, Proc. Natl. Acad. Sci., **96**, 11277 (1999); G. U. Lee, L. A. Chris and R. J. Colton, *Direct Measurement of the Forces Between Complementary Strands of DNA*, Science, **266**, 771 (1994).

[29] G. M. Carter, Y. J. Chen, S. K. Tripathy, *Intensity-Dependent Index of Refraction in Multilayers of Polydiacetylene*, Appl. Phys. Lett., **43**, 891 (1983).

[30] M. D. Mowery, A. C. Smith and C. E. Evans, *Polydiacetylene Monolayers as Versatile Photoresisits for Interfacial Patterning*, Langmuir, **16**, 5998 (2000).

[31] D. H. Charych, J. O. Nagy, W. Spevak and M. D. Bednarski, *Direct Colimetric Detection of a Receptor-Ligand Interaction by a Polymerized Bilayer Assembly*, Science, **261**, 585 (1993); A. Reichert, J. Nagy, W. Spevak and D. H. Charych, *Polydiacetylene Liposomes Functionalized with Sialic Acid Bind and Colimetrically Detect Influenza Virus*, J. Am. Chem. Soc., **117**, 829 (1995).

[32] E. Sparr, K. Ekelund, J. Engblom, S. Engström and H. Wennerström, *An AFM study of Lipid Monolayers. 2. Effect of Cholesterol on Fatty Acids*, Langmuir, **15**, 6950 (1999); E. Sparr, L. Eriksson, J. A. Bouwstra and K. Ekelund, *AFM Study of Lipid Monolayers: III. Phase Behavior of Ceramides, Cholesterol and Fatty Acids*, Langmuir, **17**, 164 (2001).

[33] M. Ruths, H. Ohtani, M. L. Greenfield, S. Granick, *Exploring the "Friction Modifier" Phenomenon: Nanorheology of n-Alkane Chains with Polar Terminus Dissolved in n-Alkane Solvent*, Tribol. Lett., **6**, 207 (1999); M. L. Greenfield, H. Ohtani, *Molecular Dynamics Simulation Study of Model Friction Modfier Additives Confined between two Surfaces*, Tribol. Lett., **7**, 137 (1999).

[34] L. Xu, D. F. Ogletree, M. Salmeron, H. Tang, J. Gui and B. Marchon, *De-Wetting of Lubricants on Hard Disks*, J. Chem. Phys., **112**, 2952 (2000); R. J. A. van den Oetelaar, L. Xu, D. F. Ogletree, M. Salmeron, H. Tang and J. Gui, *Tribocharging Phenomena in Hard Disk Amorphous Carbon Coatings with and without Perfluoro-Polyether Lubricants*, J. Appl. Phys., **89**, 3993 (2001).

[35] for example C. P. Tripp, R. P. N. Veregin, M. N. V. McDougall and D. Osmond, *Reaction of Alkyltrichlorosilanes with Silica: Importance of a Surface Attachment in Defining the Triboelectrification of the Modified Silica*, Langmuir, **11**, 1858 (1995).

[36] C. D. Frisbie, L. F. Rozsnyai, A. Noy, M. S. Wrighton and C. M. Lieber, *Functional Group Imaging by Chemical Force Microscopy*, Science, **265**, 2071 (1994).

[37] A. Ulman, *An Introduction to Ultrathin Organic Films From Langmuir-Blodgett to Self-Assembly* (Academic Press Inc., San Diego, 1991).

[38] D. K. Schwartz, *Langmuir-Blodgett Film Structure*, Surf. Sci. Rep., **27**, 241 (1997).

[39] J. A. DeRose and R. M. Leblanc, *Scanning Tunneling and Atomic Force Microscopy Studies of Langmuir-Blodgett Films*, Surf. Sci. Rep., **22**, 73 (1995).

[40] I. Doudevski, W. A. Hayes and D. K. Schwartz, *Submonolayer Island Nucleation and Growth Kinetics during Self-Assembled Monolayer Formation*, Phys. Rev. Lett. **81**, 4927 (1998).

[41] C. Carraro, O. W. Yauw, M. M. Sung and R. Maboudian *Observation of Three Growth Mechanisms in Self-Assembled Monolayers*, J. Phys. Chem. B, **102**, 4441 (1998).

[42] A. N. Parikh, D. L. Allara, I. Ben Azouz and F. Rondelez, *An Intrinsic Relationship between Molecular Structure in Self-Assembled n-Alkylsiloxane Monolayers and Deposition Temperature*, J. Phys. Chem., **98**, 7577 (1994).

[43] H. Brunner, T. Vallant, U. Mayer, H. Hoffmann, B. Basnar, M. Vallant and G. Friedbacher, *Substrate Effects on the Formation of Alkylsiloxane Monolayers*, Langmuir, **15**, 1899 (1999).

[44] D. L. Allara, A. N. Parikh and F. Rondelez, *Evidence for a Unique Chain Organization in Long Chain Silane Monolayers Deposited on Two Widely Different Solid Substrates*, Langmuir, **11**, 2357 (1995).

[45] T. Vallant, H. Brunner, U. Mayer, H. Hoffmann, T. Leitner, R. Resch, and G. Friedbacher, *Formation of Self-Assembled Octadecylsiloxane Monolayers on Mica and Silicon Surfaces Studied by Atomic Force Microscopy and Infrared Spectroscopy*, J. Phys. Chem. B, **102**, 7190 (1998).

[46] A. N. Parikh, M. A. Schivley, E. Koo, K. Seshadri, D. Aurentz, K. Mueller, and D. L. Allara, *n-Alkylsiloxanes: From Single Monolayers to Layered Crystals. The Formation of Crystalline Polymers from the Hydrolysis of n-Octadecyltrichlorosilane*, J. Am. Chem. Soc., **119**, 3135 (1997).

[47] A. Lio, C. Morant, D. F. Ogletree and M. Salmeron, *Atomic Force Microscopy Study of the Pressure-Dependent Structural and Frictional Properties of n-Alkanethiols on Gold* J. Chem. Phys. B., **101**, 4767 (1997).

[48] G.-y. Liu and M. B. Salmeron *Reversible Displacement of Chemisorbed n-Alkanethiol Molecules on Au(111) Surface: An Atomic Force Microscopy Study*, Langmuir, **10**, 367 (1994).

[49] G.-y. Liu, P. Fenter, C. E. D. Chidsey, D. F. Ogletree, P. Eisenberger and M. Salmeron, *An Unexpected Packing of Fluorinated n-Alkane Thiols on Au(111): A Combined Atomic Force Microscopy and X-Ray Diffraction Study*, J. Chem. Phys., **101**, 4301 (1994).

[50] W. F. Kolbe, D. F. Ogletree and M. B. Salmeron, *Atomic Force Microscopy Imaging of T4 Bacteriophages on silicon substrates*, Ultramicroscopy, **42-44**, 1113 (1992).

[51] Q. Dai, R. Vollmer, R. W. Carpick, D. F. Ogletree and M. Salmeron *A Variable Temperature Ultrahigh Vacuum Atomic Force Microscope*, Rev. Sci. Instrum., **66**, 5266 (1995).

[52] M. Salmeron, G. Neubauer, A. Folch, M. Tomitori, D. F. Ogletree and P. Sautet, *Viscoelastic and Electrical Properties of Self-Assembled Monolayers on Au(111) Films* Langmuir, **9**, 3600 (1993).

[53] R. Erlandsson, G. Hadziioannou, C. M. Mate, G. M. McClelland and S. Chiang, *Atomic Scale Friction between the Muscovite Mita Cleavage Plane and a Tungsten Tip*, J. Chem. Phys. **89**, 5190 (1988).

[54] J. P. Cleveland, S. Manne, D. Bocek, P. K. Hansma, *A Nondestructive Method for Determining the Spring Constant of Cantilevers for Scanning Force Microscopy*, Rev. Sci. Instrum., **64**, 403 (1993).

[55] Y. Q. Li, N. J. Tao, J. Pan, A. A. Garcia and S. M. Lindsay, *Direct Measurement of Interaction Forces between Colloidal Particles Using the Scanning Force Microscope*, Langmuir, **9**, 637 (1993).

[56] M. Jaschke, H. J. Butt, *Height Calibration of Optical Lever Atomic Force Microscopes by Simple Laser Interferometry*, Rev. Sci. Instrum., **66**, 1258 (1995).

[57] D. A. Walters, J. P. Cleveland, N. H. Thomson, P. K. Hansma, M. A. Wendman, G. Gurley and V. Elings, *Short Cantilevers for Atomic Force Microscopy*, Rev. Sci. Instrum., **67**, 3583 (1996).

[58] J. E. Sader and L. White, *Theoretical Analysis of the Static Deflection of Plates for Atomic Force Microscopy Applications*, J. Appl. Phys., **74**, 1 (1993). J. M. Neumeister and W. A. Ducker, *Lateral, Normal and Longitudinal Spring Constants of Atomic Force Microscopy Cantilevers*, Rev. Sci. Instrum., **65**, 2527 (1994).

[59] J. E. Sader, I. Larson, P. Mulvaney, L. R. White, *Method for the Calibration of Atomic Force Microscope Cantilevers*, Rev. Sci. Instrum., **66**, 3789 (1995).

[60] D. F. Ogletree, R. W. Carpick and M. Salmeron, *Calibration of Frictional Forces in Atomic Force Microscopy*, Rev. Sci. Instrum., **67**, 3298 (1996).

[61] J. S. Villarrubia, *Scanned Probe Microscope Tip Characterization without Calibrated Characterizers*, J. Vac. Sci. Technol. B, **14**, 1518 (1996).

[62] C. M. Mate, G. M. McClelland, R. Erlandsson and S. Chiang, *Atomic-Scale Friction of a Tungsten Tip on a Graphite Surface* Phys. Rev. Lett., **59**, 1942 (1987).

[63] R. Lüthi, E. Meyer, M. Bammerlin, L. Howald, H. Haefke, T. Lehmann, C. Loppacher, H.-J. Güntherodt, T. Gyalog and H. Thomas, *Friction on the Atomic Scale: An Ultrahigh Vacuum Atomic Force Microscopy Study on Ionic Crystals*, J. Vac. Sci. Technol. B, **14**, 1280 (1996); S. Morita, S. Fujisawa and Y. Sugawara, *Spatially Quantized Friction with a Lattice Periodicity*, Surf. Sci. Rep., **23**, 23 (1996); L. Howald, R. Lüthi, E. Meyer, G. Gerth, H. Haefke, R. Overney and H.-J. Güntherodt, *Friction Force Microscopy on Clean Surfaces of NaCl, NaF, an AgBr*, J. Vac. Sci. Technol. B, **12**, 2227 (1994).

[64] L. Howald, R. Lüthi, E. Meyer and H.-J. Güntherodt, *Atomic-Force Microscopy on the Si(111)7×7 Surface*, Phys. Rev. B, **51**, 5484 (1995).

[65] M. Bammerlin, R. Lüthi, E. Meyer, A. Baratoff, J. Lü, M. Guggisberg, C. Loppacher, Ch. Gerber and H.-J. Güntherodt, *Dynamic SFM with True Atomic Resolution on Alkali Halide Surfaces*, Appl. Phys. A, **66**, S293 (1998).

[66] Y. Martin, C. C. Williams and H. K. Wickramasinghe, *Atomic Force Microscope-Force Mapping and Profiling on a sub 100-Å Scale*, J. Appl. Phys. **61**, 4723 (1987).

[67] J. Hu, X.-d. Xiao and M. Salmeron, *Scanning Polarization Force Microscopy: A Technique for Imaging Liquids and Weakly Absorbed Layers*, Appl. Phys. Lett., **67**, 476 (1995).

[68] C. Schönenberger and S. F. Alvarado, *Observation of Single Charge Carriers by Force Microscopy*, Phys. Rev. Lett., **65**, 3162 (1990).

[69] H. Yokohama and T. Inoue, Thin Solid Films, **242**, 33 (1994).

[70] J. M. R. Weaver and D. W. Abraham, *High Resolution Atomic Force Microscopy Potentiometry*, J. Vac. Sci. Technol. B, **9**, 1559 (1991); M. Nonnenmacher, M. P. O'Boyle and H. K. Wickramasinghe, *Kelvin Probe Force Microscopy*, Appl. Phys. Lett., **58**, 2921 (1991).

[71] J. Lü, M. Guggisberg, R. Lüthi, M. Kubon, L. Scandella, Ch. Gerber, E. Meyer and H.-J. Güntherodt, *Surface Potential Studies Using Kelvin Force Spectroscopy*, Appl. Phys. A, **66**, 273 (1998).

[72] M. Salmeron, *Nanoscale Wetting and De-Wetting of Lubricants with Scanning Polarization Force Microscopy (Review)*, Fundamentals of Tribology and Bridging the Gap Between the Macro- and Micro/Nanoscales, ed. B. Bhushan, pp. 651-662. NATO ASI Series E: Applied Sciences. Kluwer Academic Publishers, The Netherlands, 2001.

[73] D. DeVecchio and B. Bhushan, *Use of a Nanoscale Kelvin Probe for Detecting Wear Precursors*, Rev. Sci. Instrum., **69**, 3618 (1998).

[74] S. Kopta and M. Salmeron, *The Atomic Scale Origin of Wear on Mica and its Contribution to Fricition*, J. Chem. Phys., **113**, 8249 (2000).

[75] J. Hu, X.-d. Xiao, D. F. Ogletree and M. Salmeron, *Atomic Scale Friction and Wear of Mica*, Surf. Sci., **327**, 358 (1995).

[76] G. Brusdeylins and D. Schmicker, *Elastic and Ineleastic Helium Atom Scattering at a Cleaved Mica Sheet*, Surf. Sci., **331-333**, 237 (1995).

[77] L. Xu, A. Lio, J. Hu, D. F. Ogletree and M. Salmeron, *Wetting and Capillary Phenomena of Water on Mica* J. Phys. Chem., **102**, 540 (1998).

[78] J. T. Dickinson, N.-S. Park, M.-W. Kim and S. C. Langford, *A Scanning Force Microscope Study of a Tribochemical System: Stress-Enhanced Dissolution*, Tribol. Lett., **3**, 69 (1997); or N.-S. Park, M.-W. Kim, S. C. Langford, J. T. Dickinson, *Atomic Layer Wear of Single-Crystal Calcite in Aqueous Solution Using Scanning Force Microscopy*, J. Appl. Phys., **80**, 2680 (1996).

[79] E. Barrena, S. Kopta, D. F. Ogletree, D. H. Charych and M. Salmeron, *Relationship between Friction and Molecular Structure: Alkylsilane Lubricant Films under Pressure*, Phys. Rev. Lett., **82**, 2880 (1999).

[80] A. Würger, *Comment on "Relationship between Friction and Molecular Structure: Alkylsilane Lubricant Films under Pressure"*, Phys. Rev. Lett. **83**, 1696 (1999).

[81] S. Kopta, E. Barrena, D. F. Ogletree, D. H. Charych and M. Salmeron, *Reply to Comment on "Relationship between Friction and Molecular Structure: Alkylsilane Lubricant Films under Pressure"*, Phys. Rev. Lett. **83**, 1697 (1999).

[82] J. Fang and C. M. Knobler, *Contro of Density in Self-Assembled Organosilane Monolayers by Langmuir-Blodgett Deposition*, J. Phys. Chem., **99**, 10425 (1995).

[83] X.-d. Xiao, G.-y. Liu, D. H. Charych and M. Salmeron, *Preparation, Structure, and Mechanical Stability of Alkylsilane Monolayers on Mica*, Langmuir, **11**, 1600 (1995).

[84] D. K. Schwartz, S. Steinberg, J. Israelachvili, J. A. N. Zasadzinski, *Growth of a Self-Assembled Monolayer by Fractal Aggregation*, Phys. Rev. Lett., **69**, 3354 (1992).

[85] R. R. Rye, G. C. Nelson and M. T. Dugger, *Mechanistic Aspects of Alkylchlorosilane Coupling Reactions* Langmuir, **13**, 2965 (1997).

[86] M. M. Sung, C. Carraro, O. W. Yauw, Y. Kim and R. Maboudian, *Reversible Liquid-Liquid Transitions in the Early Stages of Monolayer Self-Assembly*, J. Phys. Chem. B, **104**, 1556 (2000).

[87] E. Barrena, C. Ocal and M. Salmeron, *Evolution of the Structure and Mechanical Stability of Self-Assembled Alkanethiol Islands on Au(111) due to Diffusion and Ripening*, J. Chem. Phys., **111**, 9797 (1999).

[88] T. P. Weihs, Z. Nawaz, S. P. Jarvis, J. B. Pethica, *Limits of Imaging Resolution for Atomic Force Microscopy of Molecules*, Appl. Phys. Lett. **59**, 3536 (1991).

[89] A. I. Kitaigorodskii, *Organic Chemical Crystallography* (Consultants Bureau, New York, 1961).

[90] D. A. Outka, J. Stöhr, J. P. Rabe, J. D. Swalen, *The Orientation of Langmuir-Blodgett monolayers using NEXAFS* J. Chem. Phys. **88**, 4076 (1988).

[91] D. K. Schwartz, R. Viswanathan and J. A. N. Zasadzinski, *Coexisting Lattice Structures in a Langmuir-Blodgett Film Identified by Atomic Force Microscopy*, Langmuir, **9**, 1384 (1993).

[92] H. G. Olf and A. Peterlin, J. of Polym. Sci. A-2 **8**, 753 (1970); **8**, 771 (1970).

[93] E. Barrena C. Ocal and M. Salmeron, *Structure and Stability of Tilted-Chain Phases of Alkanethiols on Au(111)*, J. Chem. Phys. **114**, 4210 (2001).

[94] E. Barrena, C. Ocal and M. Salmeron, *Molecular Packing Changes of Alkanethiols Monolayers on Au(111) Under Applied Pressure*, J. Chem. Phys., **113**, 2413 (2000).

[95] J. Israelachvili, *Intermolecular and Surface Forces*, ed. 2 (Academic Press, New York, 1991), p. 89.

[96] M. D. Mowery, S. Kopta, D. F. Ogletree, M. Salmeron and C. E. Evans, *Structural Manipulation of the Fricitonal Properties of Linear Polymers in Single Molecular Layers*, Langmuir, **15**, 5118 (1999).

[97] C. A. Alves, E. L. Smith and M. D. Porter, *Atomic Scale Imaging of Alkanethiolate Monolayers at Gold Surfaces with Atomic Force Microscopy*, J. Am. Chem Soc., **114**, 1222 (1992).

[98] J. Pan, N. Tao and S. M. Lindsay, *An Atomic Force Microscopy Study of a Self-Assembled Octadecyl Mercaptan Monolayer Adsorbed on Gold(111) under Potential Control*, Langmuir, **9**, 1556 (1993).

[99] K. Kojio, S. Ge, A. Takahara, T. Kajiyama, *Molecular Aggregation State of n-Octadecyltrichlorosilane Monolayer Prepared at an Air/Water Interface*, Langmuir **14**, 971 (1998).

[100] R. S. Clegg and J. E. Hutchinson, *Hydrogen-Bonding, Self-Assembled Monolayers: Ordered Molecular Films for Study of Through-Peptide Electron Transfer*, Langmuir, **12**, 5239 (1996); R. C. Sabapathy, S. Bhattacharyya, M. C. Leavy, W. E. Cleland and C. L. Hussey, *Eletrochemical and Spectroscopic Characterization of Self-Assembled Monolayers of Ferrocenylalkyl Compounds with Amide Linkages*, Langmuir, **14**, 124 (1998).

[101] S. B. Sachs, S. P. Dudek, R. P. Hsung, L. R. Sita, J. F. Smalley, M. D. Newton, S. W. Feldberg and C. E. D. Chidsey, *Rates of Interfacial Electron Transfer Through π-Conjugated Spacers*, J. Am. Chem. Soc., **119**, 10563 (1997).

[102] S. D. Evans, K. E. Goppert-Berarducci, E. Urankar, L. J. Gerenser and A. Ulman, *Monolayers Having Large In-Plane Dipole Moments: Characterization of Sulfone-Containing Self-Assembled Monolayers of Alkanethiols on Gold by Fourier Transform Infrared Spectroscopy, X-ray Photoelectron Spectroscopy, and Wetting*, Langmuir, **7**, 2700 (1991); A. Dhirani, R. W. Zehner, R. P. Hsung, P. Guyot-Sionnest and L. R. Sita, *Self-Assembly of Conjugated Molecular Rods: A High-Resolution STM Study*, J. Am. Chem Soc., **118**, 3319 (1996).

[103] J. S. Peanasky and R. L. McCarley, *Surface-Confined Monomers on Electrode Surfaces. 4. Electrochemical and Spectroscopic Characterization of Undec-10-ene-1-thiol Self-Assembled Monolayers on Au*, Langmuir, **14**, 113 (1998); D. N. Batchelder, S. D. Evans, T. L. Freeman, L. Häussling, H. Ringsdorf and H. Wolf, *Self Assembled Monolayers Containing Polydiacetylenes*, J. Am. Chem. Soc., **116**, 1050 (1994); T. Kim, R. M. Crooks, M. Tsen and L. Sun, *Polymeric Self-Assembled Monolayers. 2. Synthesis and Characterization of Self-Assembled Polydiacetylene Mono- and Multilayers*, J. Am. Chem. Soc., **117**, 3963 (1995); T. Kim, Q. Ye, L. Sun, K.C. Chan and R. M. Crooks, *Polymeric Self-Assembled Monolayers. 5. Synthesis and Characterization of ω-Functionalized, Self-Assembled Diacetylenic and Polydiacetylenic Monolayers*, Langmuir, **12**, 6065 (1996).

[104] T. Kim, K. C. Chan and R. M. Crooks, *Polymeric Self-Assembled Monolayers. 4. Chemical, Electrochemical, and Thermal Stability of ω-Functionalized, Self-Assembled Diacetylenic and Polydiacetylenic Monolayers*, J. Am. Chem. Soc., **119**, 189 (1997).

[105] H. Menzel, M. D. Mowery, M. Cai and C. E. Evans, *Vertical Positioning of Internal Molecular Scaffolding within a Single Molecular Layer*, J. Phys. Chem. B, **102**, 9550 (1998).

[106] J. B. Lando in *Polydiacetylenes*; eds. D. Bloor, R. Chance, Nijhoff: Dordrecht, The Netherlands (1985); M. W. Schott and G. Wegner in *Nonlinear Optical Properties of Organic Molecules and Crystals*, ed. J. Chemla, Academic Press: Orlando, Florida, USA (1987); G. Cao and T. E. Mallouk, *Topochemical Diacetylene Polymerization in Layered Metal Phosphate Salts*, J. Solid State Chem., **94**, 59 (1991).

[107] A. Lio, A. Reichert, N. O. Nagy, M. Salmeron and D. H. Charych, *Atomic Force Microscope Study of Chromatic Transitions in Polydiacetylene Thin Films*, J. Vac. Sci. Technol. B, **14**, 1481 (1996).

[108] A. Lio, A. Reichert, D. Ahn, N. O. Nagy, M. Salmeron and D. H. Charych, *Molecular Imaging of Thermochromic Carbohydrate-Modified Polydiacetylene Thin Films*, Langmuir, **13**, 6524 (1997).

[109] R. W. Carpick, D. Y. Sasaki and A. R. Burns, *Large Friction Anisotropy of a Polydiacetylene Monolayer*, Tribol. Lett., **7**, 79 (1999).

[110] M. D. Mowery and C. E. Evans, *The Synthesis of Conjugated Diacetylene Monomers for the Fabrication of Polymerized Monolayer Assemblies*, Tetrahedron Lett., **38**, 11 (1997).

[111] M. Cai, M. D. Mowery, H. Menzel and C. E. Evans, *Fabrication of Extended Conjugation Length Polymers within Diacetylene Monolayers on Au Surfaces: Influence of UV Exposure Time*, Langmuir, **15**, 1215 (1999).

[112] M. J. Tarlov, D. R. F. Burgess, Jr. and G. Gillen, *UV Photopatterning of Alkanethiolate Monolayers Self-Assembled on Gold and Silver*, J. Am. Chem. Soc., **115**, 5305 (1993)

[113] M. Gleiche, L. F. Chi and H. Fuchs, *Nanoscopic Channel Lattices with Controlled Anisotropic Wetting*, Nature, **403**, 173 (2000).

[114] H. Gau, S. Herminghaus, P. Lenz and R. Lipowsky, *Liquid Morphologies of Structured Surfaces: From Microchannels to Microchips*, Science, **283**, 46 (1999).

[115] J. Huang and J. C. Hemminger, *Photooxidation of Thiols in Self-Assembled Monolayers on Gold*, J. Am. Chem. Soc., **115**, 3342 (1993).

[116] S. Xu, P. E. Laibinis and G.-y. Liu, *Accelerating the Kinetics of Thiol Self-Assembly on Gold - A Spatial Confinement Effect*, J. Am. Chem. Soc., **120**, 9356 (1998).

[117] J. Lü, E. Delamarche, L. Eng, R. Bennewitz, E. Meyer and H.-J. Güntherodt, *Kelvin Probe Force Microscopy on Surfaces: Investigation of the Surface Potential of Self-Assembled Monolayers on Gold*, Langmuir, **15**, 8184 (1999).

[118] T. Pompe and S. Herminghaus, *Three-Phase Contact Line Energetics from Nanoscale Liquid Surface Topographies*, Phys. Rev. Lett., **85**, 1930 (2000).

Acknowledgements

When I started out on this venture called a Ph.D. thesis I was a hard core physicist with confused ideas what I wanted to accomplish and furthermore with a strong chemistry-intolerance. Sure enough not too many of the initial ideas could be accomplished, but other experiments took their place and proved successful. What was more bothering was the necessity to learn some "chemistry", at least enough to prepare my samples without hurting myself in the course. Besides the scientific aspects of this work I greatly enjoyed meeting scientists from all across the globe, which makes this world look like not such a vast place, after all.
Now and here is the right occasion to acknowledge all those who contributed to the progress and final success of this ordeal, in the order they come to my mind:
I want to thank Prof. Ernst Meyer, for accepting the task of being my thesis advisor, for supporting my visit of the group of Dr. Miquel Salmeron at the Lawrence Berkeley National Laboratory, and for trusting me with an interesting challenge concluding my experimental work.
I would also like to acknowledge Prof. Hans-Joachim Güntherodt's support for my research trip to "sunny" California. This visit would not have been possible without a fellowship from the *Uarda Frutiger-Fonds* of the *Freiwillige Akademische Gesellschaft* (Basel) and I am grateful for the support of Prof. Iris Zschokke-Gränacher to obtain this fellowship.
For granting me the opportunity of a most(ly) successful time at his group at LBNL, his enthusiastic encouragement, abundant knowledge about tribology, and his never dwindling supply off new ideas my appreciation goes to Dr. Miquel Salmeron.
I would like to dedicate a very special thank you for their administrative work to Jaqueline Vetter, and Mae Lum. Besides graduate students you are the hardest working worst paid people I know. Alexandre Bouhelier and Dr. Roland Bennewitz were particularly helpful in pointing me to and giving practical advice for the latest LATEX version and corresponding editor. It is really cool to get your thesis as reasonably sized pdf file in one click! I am also grateful for the opportunity to get some teaching experience, granted by Roland.
I have to thank Viola Barwich and Irina Schumakovitch for the introduction on the Nanoscope AFM and teaching me its "in liquid" operation, respectively.
For an excursion into the field of glass my appreciation goes to Prof. Eric Courtens. The workshop crew of Heinz Breitenstein was most helpful (as usual) in building/modifying certain sample holders and sample cleavage tools at very short notice (also as usual).
Leo Merz and Adriaan Bredekamp I want to thank for welcoming me back home with friendly banter, just like it was during the time of my diploma thesis between "Snomies" and "Krafties".
I also want to acknowledge all the members of the group of Prof. Hans-Joachim Güntherodt and Prof. Ernst Meyer, who I haven't mentioned individually, especially those who willingly shared their knowledge about latest developments in surface science research before my exam.
Special thanks go to Dr. Esther Barrena, who kicked off this whole tilting molecules business with me. I think we were a good team and I missed her, no matter how many times we nearly electrocuted each other on the cramped space in front of the setup with chairs that can charge up to 100'000 Volts (at least): "Sussie, one day you're gonna kill me!" Oh, and I still follow her recipe for "arroz con leche".
My knowledge about the AFM setup, especially the electronics and software part, and about

the SPFM technique I owe to Dr. Hendrik Blum and Dr. Lei Xu. Furthermore I would like to thank Hendrik for his patience with my short tempered outbursts in the lab.
Dr. Frank Ogletree was most helpful regarding thoretical and practical issues of AFM and I would like to acknowledge in particular many "door frame discussions".
Dr. Deborah Charych, Dr. Ulrich Jonas and Dr. Martina Kubon deserve special acknowledgement for patiently teaching elementary chemistry to a person void of any knowledge in this field and scared of anything that smells or has a pH outside 4-8, leaving alone bottles with skulls on it. As a consequence, colleagues could enjoy seing me in "full body armor": ugly red safety glasses, white lab coat and blue gloves, what usually led to such insults as e.g. "You look like a chemist!" At least Prof. Gabor Somorjai showed some mercy, seeing me with just the blue gloves on: "You look like a killer with those!" Dr. Jason Cheng, Dr. Jie Song and Dr. Ivan Kuzmenko I would like to thank for further "chemistry support", and Albert and Jenny were most helpful in showing me how to operate an LB-trough.
This work would have suffered greatly without the excellent jobs from the UC Berkeley chemistry machine shop and the LBNL ceramics workshop.
For being a really good office-mate and for pushing me on some issues my appreciation goes to Dr. Frieder Mugele. Furthermore I want to say thank you to the rest of the "German connection": Nikos Jäger and Petra Specht, just for being around.
I am grateful for Mark Rose's patience with my missing English vocabulary regarding tools, which manifested in pantomime descriptions. By now I know that my favorite "thingy" is called "caliper". I would like to thank Mark Rose and David Schleef for never grabbing me by the neck and throwing me out of the room for complaining about printers being out of service. And I really appreciated the chats with Dave over a cup of coffee, those really improved my colloquial American English.
Dr. Rob Carpick was most helpful because he actually kept track of changes to the electronics, a trait rare among physicists. And thanks for getting me stuck with one of the most annoying and useless little jobs that LBNL waste management has to offer.
I would like to acknowledge Prof. Marie-Pierre Valignat for encouraging me to ride my bike more often and for putting the elaborate version of the heatable sample holder to use, which had been sleeping on my desk.
I also enjoyed the special guest appearances of: Dr. Hjalti Skulasson (the only chemist I know who was not scared of the amount of buttons on the AFM electronics and even started playing with them without supervision),Dr. Mark Mowery (supplier of the (poly-)diacetylene samples), Craig Priest (three weeks of late night shifts but "heaps" of fun, as the Australian says), Dr. Sutapa Ghosal (now I understand much better how determined you were to finish your thesis), Dr. Natalio Mingo (our "Jack in the box": You can kill someone by sneaking up from behind and saying "HELLO!"), Prof. Joan Esteve (I had almost forgotten how to play table tennis), and Dr. Fernando Teran Arce (he pointed out all the advantages of a certain commercial AFM over this setup, by now I also know all the disadvantages of that commercial one, and thank you for helping with the temperature dependence measurements on mica, which turned out to be a humidity dependence.).
To Dr. Marius Enachescu goes my gratitude for being a caring colleague and also to his family for the help during the last days in California.
I greatly enjoyed the introduction to some strange (at least for the European trained taste) Asian specialties, administered by Winnie Ling, Osamu Takeuchi and Dr. Takahito Inoue, although I will never try the tiny, dried whole fish.
For last minute rescue operations for this thesis my appreciation goes to Dr. Jose Benitez, my last apprentice on the AFM setup and thus my rightful heir. But who will take over now that he has left, too?
I feel the need to apologize to all the people that I "bossed around", especially those who had the doubtful pleasure to learn how to use the AFM setup: Sorry folks, but after working for a

while with this cute little machine one gets a little protective. I also want to apologize to all those who I might have forgotten here and dedicate a thank you for them, too.
Furthermore, I would like to acknowledge those who helped to make life beyond the lab a little easier or more pleasant: Dr. Thilo Enderle for lots of advice on going to California, and Dr. Angelika Fath and Dr. Michael Goodin for practical help in getting started there. Dr. Thomas and Melanie Huser for being friends who even "followed" to a strange country and their daughter Carolin for showing us how much fun but also work kids can be (I think I will pass on that point for a little while longer). Dr. Peter Streckeisen holds the record in visits to California and Dr. Sabine Hild managed to bring a suitcase full of sunshine in the middle of El Niño. And I would like to reward all those who promised to visit and never did by blowing a raspberry! Sonja Leichtle deserves to be mentioned for writing more letters than anyone else without email.
Talking about California I must not forget to thank the San Andreas and Hayward faults for holding back with "the big one", and also LBNL for the cheap tickets for the Oakland A's vs. SF Giants game, now I am back in Germany and hooked on BASEBALL!
Many thanks also to the proofreaders, who made sure that there is not the slightest mistace left: Adriaan Bredekamp, Peter Kappenberger and Dr. Thilo Lacoste. Furthermore I am grateful to Peter Kappenberger and Regina Hoffmann for organizing the little celebration after my exam.
I am most grateful to my parents for their financial support for this undertaking and their great patience with my impatience during the last months of it. And my Thilo deserves a really big hug for bearing with me all the time.

List of Publication

Journal Contributions

- E. Barrena, S. Kopta, D. F. Ogletree, D. H. Charych and M. Salmeron, *Relationship between Friction and Molecular Structure: Alkylsilane Lubricant Films under Pressure*, Phys. Rev. Lett., **82**, pp. 2880-2883 (1999).
- S. Kopta, E. Barrena, D. F. Ogletree, D. H. Charych and M. Salmeron, Phys. Rev. Lett. **83**, p. 1697 (1999). Reply to A. Würger, *Comment on "Relationship between Friction and Molecular Structure: Alkylsilane Lubricant Films under Pressure"*, Phys. Rev. Lett., **83**, p. 1696 (1999).
- M. D. Mowery, S. Kopta, D. F. Ogletree, M. Salmeron and C. E. Evans, *Structural Manipulation of the Fricitonal Properties of Linear Polymers in Single Molecular Layers*, Langmuir, **15**, pp. 5118-5122 (1999).
- S. Kopta and M. Salmeron, *The Atomic Scale Origin of Wear on Mica and its Contribution to Friction*, J. Chem. Phys. **113**, pp. 8249-8252 (2000).
- J. Song, Q. Cheng, S.Kopta and R. C. Stevens, *Modulating Artificial Membrane Morphology: pH-Induced Chromatic Transition and Nanostructural Transformation of a Bolaamphiphilic Conjugated Polymer from Blue Helical Ribbons to Red Nanofibers*, Journal of the American Chemical Society **123**, pp. 3205-3213 (2001).

Conference Proceedings

- M. Salmeron, S. Kopta, E. Barrena and C. Ocal: *Atomic scale origin of adhesion and friction (review)*, Proceedings of the NATO-ASI Conference on Fundamentals of Tribology and Bridging the Gap Between the Macro- and Micro/Nanoscales, Keszthely, Hungary, August 13-25, 2000. In B. Bhushan (ed.): Fundamentals of Tribology and Bridging the Gap Between the Macro- and Micro/Nanoscales, Kluwer Academic Publishers, The Netherlands, *NATO ASI Series E: Applied Sciences*, pp. 41-52 (2001).

Unpublished Conference Contributions

- S. Kopta, E. Barrena, D. F. Ogletree, D. H. Charych and M. Salmeron: *The Relationship Between Friction and Molecular Structure: Alkylsilane Lubricant Films under Pressure.* 217^{th} National Meeting of the American Chemical Society, in Anaheim, California, USA, March 1999.